

¹ **Searches for Supersymmetry using the α_T**
² **variable with the CMS detector at the LHC**

³ Darren Burton

⁴ Imperial College London
⁵ Department of Physics

⁶ A thesis submitted to Imperial College London
⁷ for the degree of Doctor of Philosophy

9 Abstract

10 A search for supersymmetric particles is presented, using the Compact
11 Muon Solenoid detector at the Large Hadron Collider, with a signature
12 of missing energy in events with high p_T jets is presented. The analysis is
13 performed with 11.7 fb^{-1} of data, collected at a center-of-mass energy of
14 8 TeV during the 2012 run period. The dimensionless kinematic variable
15 α_T is used to select events with genuine missing energy signatures, while
16 Standard Model backgrounds in the signal region estimated using data
17 driven control samples. A complementary method to search for natural
18 SUSY signatures with a high number of b-flavoured jets, through the use
19 of a simple template fit is presented. The α_T search is used as a vehicle to
20 demonstrate proof of principle and as a search region for this technique.
21 Additionally the efficiency of the hadronic Level-1 single jet triggers are
22 measured throughout the 2012 run period. Results are presented with
23 a view to comparing L1 jet performance, before and after, a change
24 to the jet seed algorithm implemented during data taking. No excess
25 of events is found over Standard Model expectations in the α_T search.
26 Exclusion limits are set at the 95% confidence level in the parameter
27 space of simplified models, with special emphasis on compressed spectra
28 and natural SUSY scenarios.

29

Declaration

30 I, the author of this thesis, declare that the work presented within this
31 document to be my own. The work presented in Chapters 4, 5, 6 and Section
32 3.4.1, is a result of the author's own work or that of which I have been a
33 major contributor unless explicitly stated otherwise, and is carried out within
34 the context of the Imperial College London and CERN SUSY groups, itself a
35 subsection of the greater CMS collaboration. All figures and studies taken
36 from external sources are referenced appropriately throughout this document.

37

Darren Burton

38

Acknowledgements

39 Of the many people who deserve thanks, some are particularly prominent.... Thank
40 Rob Thank Jad

41 Contents

42	List of Figures	viii
43	List of Tables	xii
44	1. Introduction	2
45	2. A Theoretical Overview	5
46	2.1. The Standard Model	5
47	2.1.1. Gauge Symmetries of the SM	7
48	2.1.2. The Electroweak Sector and Electroweak Symmetry Breaking	9
49	2.2. Motivation for Physics Beyond the Standard Model	13
50	2.3. Supersymmetry Overview	15
51	2.3.1. R-Parity	16
52	2.4. Experimental signatures of SUSY at the LHC	17
53	2.4.1. Simplified Models	18
54	3. The LHC and the CMS Detector	20
55	3.1. The LHC	20
56	3.2. The CMS detector	23
57	3.2.1. Detector Subsystems	23
58	3.2.2. Tracker	24
59	3.2.3. Electromagnetic Calorimeter	25
60	3.2.4. Hadronic Calorimeter	26
61	3.2.5. Muon Systems	28
62	3.3. Event Reconstruction and Object Definition	28
63	3.3.1. Jets	28
64	3.3.2. B-tagging	30
65	3.4. Triggering System	33
66	3.4.1. The Level-1 Trigger	34

67	3.4.2. L1 Trigger Jet Algorithm	35
68	3.4.3. Measuring L1 Jet Trigger Efficiencies	37
69	3.4.4. Effects of the L1 Jet Seed	38
70	3.4.5. Robustness of L1 Jet Performance against Pile-up	40
71	3.4.6. Summary	43
72	4. SUSY searches in Hadronic Final States	45
73	4.1. An introduction to the α_T search	46
74	4.1.1. The α_T variable	48
75	4.2. Search Strategy	50
76	4.2.1. Physics Objects	53
77	4.2.2. Event Selection	55
78	4.2.3. Control Sample Definition and Background Estimation	58
79	4.2.4. Estimating the QCD Background Multi-jet Background	65
80	4.3. Trigger Strategy	67
81	4.4. Measuring MC normalisation factors via H_T sidebands	68
82	4.5. Determining MC Yields With Higher Statistical Precision	69
83	4.5.1. The formula method	70
84	4.5.2. Establishing proof of principle	71
85	4.5.3. Correcting Measured Efficiencies In Simulation To Data	71
86	4.6. Systematic Uncertainties On Transfer Factors	72
87	4.6.1. Determining systematic uncertainties from closure tests	75
88	4.7. Statistical Framework	78
89	4.7.1. Hadronic sample	78
90	4.7.2. H_T evolution model	79
91	5. Searches For Natural SUSY With B-tag Templates.	80
92	5.1. Concept	80
93	5.2. Application to the α_T search	82
94	5.2.1. Proof of principle in simulation	83
95	5.2.2. Results in a data control sample	86
96	5.2.3. Application to the α_T hadronic search region	88
97	5.3. Conclusions	88
98	6. Results and Interpretation	89
99	6.1. Statistical Interpretation	89
100	6.2. Interpretation in Simplified Signal Models	89

101	A. Miscellaneous	90
102	A.1. Noise Filters	90
103	A.2. Primary Vertices	92
104	B. L1 Jets	94
105	B.1. Jet matching efficiencies	94
106	B.2. Leading Jet Energy Resolution	95
107	B.3. Resolution for Energy Sum Quantities	98
108	C. Additional material on background estimation methods	103
109	C.1. Determination of k_{QCD}	103
110	C.2. Effect of varying background cross sections on closure tests	104
111	D. Additional Material For B-tag Template Method	105
112	D.1. Templates Fits in Simulation	105
113	D.2. Pull Distributions for Template Fits	108
114	D.3. Templates Fits in Data	108
115	Bibliography	111

¹¹⁶ List of Figures

¹¹⁷ 2.1.	One loop quantum corrections to the Higgs squared mass parameter m_h^2 due to a fermion.	¹¹⁸ 14
¹¹⁹ 2.2.	Two example simplified model decay chains.	¹¹⁹ 19
¹²⁰ 3.1.	A top down layout of the LHC, with the position of the four main detectors labelled.	¹²¹ 21
¹²² 3.2.	The total integrated luminosity delivered to and collected by Compact Muon Solenoid (CMS) during the 2012 8 TeV pp runs	¹²³ 22
¹²⁴ 3.3.	A pictorial depiction of the CMS detector.	¹²⁴ 24
¹²⁵ 3.4.	Illustration of the CMS Electromagnetic CALorimeter (ECAL).	¹²⁵ 26
¹²⁶ 3.5.	Schematic of the CMS Hadronic CALorimeter (HCAL).	¹²⁶ 27
¹²⁷ 3.6.	Combined Secondary Vertex (CSV) algorithm discriminator values in enriched ttbar and inclusive multi jet samples	¹²⁸ 31
¹²⁹ 3.7.	Data/MC b-tag scale factors derived using the Combined Secondary Vertex Medium Working Point (CSVM) tagger.	¹³⁰ 32
¹³¹ 3.8.	Data/MC mis-tag scale factors derived using the CSVM tagger.	¹³¹ 33
¹³² 3.9.	The CMS Level 1 Trigger (L1) Trigger system.	¹³² 34
¹³³ 3.10.	Illustration of the Level-1 jet finding algorithm.	¹³³ 36
¹³⁴ 3.11.	L1 jet efficiency turn-on curves as a function of the offline CaloJet and PFJet E_T	¹³⁵ 38
¹³⁶ 3.12.	L1 jet efficiency turn-on curves as a function of the offline CaloJet E_T for the 2012 run period B and C.	¹³⁷ 39

138	3.13. Trigger cross section for the L1HTT150 trigger path.	40
139	3.14. L1 H_T efficiency turn-on curves as a function of the offline CaloJet H_T	41
140	3.15. L1 jet efficiency turn-on curves as a function of the leading offline E_T Calo	
141	(left) and PF (right) jet, for low, medium and high pile-up conditions.	42
142	3.16. Fit values from an Exponentially Modified Gaussian (EMG) function fitted	
143	to the resolution plots of leading Calo jet E_T measured as a function of	
144	$\frac{(L1\ E_T - \text{Offline}\ E_T)}{\text{Offline}\ E_T}$ for low, medium and high pile-up conditions.	43
145	3.17. Fit values from an EMG function fitted to the resolution plots of leading	
146	PF jet E_T measured as a function of $\frac{(L1\ E_T - \text{Offline}\ E_T)}{\text{Offline}\ E_T}$ for low, medium and	
147	high pile-up conditions.	44
148	4.1. Reconstructed offline H_T for 11.7fb^{-1} of data after a basic pre-selection.	47
149	4.2. The event topologies of background QCD dijet events (right) and a generic	
150	SUPERSYmmetry (SUSY) signature with genuine Z_T (left).	48
151	4.3. The α_T distributions for the low 2-3 (left) and high ≥ 4 (right) jet	
152	multiplicities after a full analysis selection and shown for $H_T > 375$	50
153	4.4. Pictorial depiction of the analysis strategy employed by the α_T search to	
154	increase sensitivity to a wide spectra of SUSY models.	52
155	4.5. Data/MC comparisons of key variables for the hadronic signal region.	58
156	4.6. Data/MC comparisons of key variables for the $\mu + \text{jets}$ selection.	61
157	4.7. Data/MC comparisons of key variables for the $\mu\mu + \text{jets}$ selection.	63
158	4.8. Data/MC comparisons of key variables for the $\gamma + \text{jets}$ selection.	64
159	4.9. QCD sideband regions, used for determination of k_{QCD}	66
160	4.10. Sets of closure tests overlaid on top of the systematic uncertainty used for	
161	each of the five H_T regions.	77
162	5.1. The b-tagging (a), c-quark mis-tagging (b), and light-quark mis-tagging	
163	rate (c) as measured in simulation after the α_T analysis, $\mu + \text{jets}$ control	
164	sample selection in the region $H_T > 375$	82

165	5.2. The results of fitting the $Z = 0$ and $Z = 2$ templates to the $n_b^{reco} = 0, 1, 2$ bins taken directly from simulation in the region $H_T > 375$ GeV, for the $n_{jet} \geq 5$ category.	85
166		
167		
168	5.3. The results of fitting the $Z = 0$ and $Z = 2$ templates to the $n_b^{reco} = 0, 1, 2$ bins taken from data, for the $n_{jet} \geq 5$ category and medium CSV working point.	87
169		
170		
171	B.1. Leading jet matching efficiency as a function of the offline CaloJet E_T	94
172		
173	B.2. Resolution plots of the leading offline Calo E_T measured as a function of $\frac{(L1 E_T - \text{Offline } E_T)}{\text{Offline } E_T}$ for low (a), medium (b) and high (c) pile-up conditions.	96
174		
175	B.3. Resolution plots of the leading off-line PF E_T measured as a function of $\frac{(L1 E_T - \text{Offline } E_T)}{\text{Offline } E_T}$ for low (a), medium (b) and high (c) pile-up conditions.	98
176		
177	B.4. $\sum E_T$ resolution parameters in bins of Calo $\sum E_T$ measured for the defined low, medium and high pile up conditions.	99
178		
179	B.5. $\sum E_T$ resolution parameters in bins of PF $\sum E_T$ measured for the defined low, medium and high pile up conditions.	99
180		
181	B.6. \cancel{E}_T resolution parameters in bins of Calo \cancel{E}_T measured for the defined low, medium and high pile up conditions.	100
182		
183	B.7. \cancel{E}_T resolution parameters in bins of PF \cancel{E}_T measured for the defined low, medium and high pile up conditions.	100
184		
185	B.8. H_T resolution parameters in bins of Calo H_T measured for the defined low, medium and high pile up conditions.	101
186		
187	B.9. H_T resolution parameters in bins of PF H_T measured for the defined low, medium and high pile up conditions.	101
188		
189	B.10. \cancel{H}_T resolution parameters in bins of \cancel{H}_T measured for the defined low, medium and high pile up conditions.	102
190		
191	B.11. \cancel{H}_T resolution parameters in bins of PF \cancel{H}_T measured for the defined low, medium and high pile up conditions.	102
192	C.1. $R_{\alpha_T}(H_T)$ and exponential fits for each of the data sideband regions. Fit is conducted between the H_T region $275 < H_T < 575$	103
193		

194	C.2. Sets of closure tests overlaid on top of the systematic uncertainty used for each of the five H_T regions.	104
195		
196	C.3. Sets of closure tests overlaid on top of the systematic uncertainty used for each of the five H_T regions.	104
197		
198	D.1. The results of fitting the $Z = 0$ and $Z = 2$ templates to the $n_b^{reco} = 0, 1, 2$ bins taken directly from simulation in the region $H_T > 375$ GeV, for the $n_{jet} = 3$ category.	106
199		
200		
201	D.2. The results of fitting the $Z = 0$ and $Z = 2$ templates to the $n_b^{reco} = 0, 1, 2$ bins taken directly from simulation in the region $H_T > 375$ GeV, for the $n_{jet} = 4$ category.	107
202		
203		
204	D.3. The results of fitting the $Z = 0$ and $Z = 2$ templates to the $n_b^{reco} = 0, 1, 2$ bins taken directly from data, for the $n_{jet} \geq 5$ category and loose CSV working point.	108
205		
206		
207	D.4. The results of fitting the $Z = 0$ and $Z = 2$ templates to the $n_b^{reco} = 0, 1, 2$ bins taken directly from data, for the $n_{jet} \geq 5$ category and tight CSV working point.	109
208		
209		

List of Tables

211	2.1. The fundamental particles of the Standard Model (SM), with spin, charge and mass displayed.	6
213	3.1. Results of a cumulative EMG function fit to the turn-on curves for L1 single jet triggers in 2012 Run Period C.	38
215	3.2. Results of a cumulative EMG function fit to the turn-on curves for L1 single jet triggers in the 2012 run period B and C.	40
217	3.3. Results of a cumulative EMG function fit to the turn-on curves for H_T in 2012 run period B and C.	41
219	3.4. Results of a cumulative EMG function fit to the efficiency turn-on curves for L1 single jet triggers in the 2012 run period C, for low,medium and high pile-up conditions.	42
222	3.5. Results of a cumulative EMG function fit to the efficiency turn-on curves for Level-1 single jet triggers in the 2012 run period C, for low,medium and high pile-up conditions.	43
225	4.1. A summary of the Simplified Model Spectra (SMS) models interpreted in this analysis, involving both direct (D) and gluino-induced (G) production of squarks and their decays.	46
228	4.2. Muon Identification criteria used within the analysis for selection/veto purposes in the muon control/signal selections.	53
230	4.3. Photon Identification criteria used within the analysis for selection/veto purposes in the $\gamma +$ jets control/signal selections.	54
232	4.4. Electron Identification criteria used within the analysis for veto purposes. .	55

233	4.5. Jet thresholds used in the three H_T regions of the analysis.	56
234	4.6. Best fit values for the parameters k_{QCD} obtained from sideband regions	
235	B,C ₁ ,C ₂ ,C ₃	67
236	4.7. Measured efficiencies of the H_T and α_T legs of the HT and HT_alphaT triggers in independent analysis bins.	68
238	4.8. k-factors calculated for different Electroweak Sector (EWK) processes. .	69
239	4.9. place holder	71
240	4.10. A summary of the results obtained from fits of zeroeth order polynomials (i.e. a constant) to five sets of closure tests performed in the $2 \leq n_{jet} \leq 3$ bin	74
243	4.11. A summary of the results obtained from fits of zeroeth order polynomials (i.e. a constant) to five sets of closure tests performed in the $n_{jet} \geq 4$ bin	74
245	4.12. A summary of the results obtained from fits of zeroeth order polynomials (i.e. a constant) to five sets of closure tests performed in the $2 \leq n_{jet} \leq 3$ bin	75
248	4.13. Calculated systematic uncertainties for the five H_T regions, determined from the closure tests.	76
250	5.1. Summary of the fit predictions in the n_b^{reco} signal region for $n_{jet} = 3, = 4, \geq 5$. The fit region is $n_b^{reco} = 0, 1, 2$ and simulation yields are normalised to an integrated luminosity of 10 fb^{-1}	84
253	5.2. Summary of the fit predictions in the n_b^{reco} signal region of the $\mu + \text{jets}$ control sample, for $n_{jet} = 3, = 4, \geq 5$. The fit region is $n_b^{reco} = 0, 1, 2$ using 11.5 fb^{-1} of data at $\sqrt{s} = 8 \text{ TeV}$	86
256	A.1. Criteria for a reconstructed jet to pass the loose calorimeter jet id.	90
257	A.2. Criteria for a reconstructed jet to pass the loose PF jet id.	91
258	A.3. Noise filters that are applied to remove spurious and non-physical \cancel{E}_T signatures within the CMS detector.	92

260	A.4. Criteria for a vertex in an event to be classified as a 'good' reconstructed primary vertex.	93
261		
262	B.1. Results of a cumulative EMG function fit to the turn-on curves for the matching efficiency of the leading jet in an event to a Level-1 jet in run 2012C and 2012B data.	95
263		
264		
265	C.1.	104

266 Acronyms

267	ALICE	A Large Ion Collider Experiment
268	ATLAS	A Toroidal LHC ApparatuS
269	APD	Avalanche Photo-Diodes
270	BSM	Beyond Standard Model
271	CERN	European Organization for Nuclear Research
272	CMS	Compact Muon Solenoid
273	CMSSM	Compressed Minimal SuperSymmetric Model
274	CSC	Cathode Stripe Chamber
275	CSV	Combined Secondary Vertex
276	CSVM	Combined Secondary Vertex Medium Working Point
277	DT	Drift Tube
278	ECAL	Electromagnetic CALorimeter
279	EB	Electromagnetic CALorimeter Barrel
280	EE	Electromagnetic CALorimeter Endcap
281	ES	Electromagnetic CALorimeter pre-Shower
282	EMG	Exponentially Modified Gaussian
283	EPJC	European Physical Journal C
284	EWK	Electroweak Sector
285	GCT	Global Calorimeter Trigger
286	GMT	Global MuonTrigger
287	GT	Global Trigger
288	HB	Hadron Barrel
289	HCAL	Hadronic CALorimeter

290	HE	Hadron Endcaps
291	HF	Hadron Forward
292	HLT	Higher Level Trigger
293	HO	Hadron Outer
294	HPD	Hybrid Photo Diode
295	LUT	Look Up Table
296	L1	Level 1 Trigger
297	LHC	Large Hadron Collider
298	LHCb	Large Hadron Collider Beauty
299	LSP	Lightest Supersymmetric Partner
300	NNLO	Next to Next Leading Order
301	POGs	Physics Object Groups
302	PS	Proton Synchrotron
303	QED	Quantum Electro-Dynamics
304	QCD	Quantum Chromo-Dynamics
305	QFT	Quantum Field Theory
306	RBXs	Readout Boxes
307	RPC	Resistive Plate Chamber
308	RCT	Regional Calorimeter Trigger
309	RMT	Regional Muon Trigger
310	SUSY	SUPerSYmmetry
311	SM	Standard Model
312	SMS	Simplified Model Spectra
313	SPS	Super Proton Synchrotron
314	TF	Transfer Factor

315	TP	Trigger Primitive
316	VEV	Vacuum Expectation Value
317	VPT	Vacuum Photo-Triodes
318	WIMP	Weakly Interacting Massive Particle

³¹⁹

“The Universe is about 1,000,000 years old.”

— Matthew Kenzie, 1987-present : Discoverer of the Higgs Boson.

³²⁰

Chapter 1.

³²¹ Introduction

³²² During the 20th century great advances have been made in our understanding of the
³²³ universe, where it comes from, where it is going and what it is made of. The Standard
³²⁴ Model (**SM**) first formulated in the 1960's is one of the crowning achievements in science's
³²⁵ quest to explain the most fundamental processes and interactions that make up our
³²⁶ universe. It has provided a highly successful explanation of a wide range of phenomena
³²⁷ in Particle Physics and has stood up to extensive experimental scrutiny [1].

³²⁸ Despite it's successes it is not a complete theory, with significant questions remaining
³²⁹ unanswered. It describes only three of the four known forces with gravity not incorpo-
³³⁰ rated within the framework of the **SM**. Cosmological experiments infer that just $\sim 4\%$
³³¹ of the observable universe exists as matter, with elusive "Dark Matter" accounting for a
³³² further $\sim 23\%$ [2]. However no particle predicted by the **SM** is able to account for it. At
³³³ higher energy scales and small distances the (non-)unification of the fundamental forces
³³⁴ point to problems with the **SM** at least at higher energies not yet probed experimentally.

³³⁵ Many theories exist as extensions to the **SM** and predict a range of observables
³³⁶ that can be detected at the Large Hadron Collider (**LHC**) of which SUperSYmmetry
³³⁷ (**SUSY**) is one such example. It predicts a new symmetry of nature in which all current
³³⁸ particles in the **SM** would have a corresponding supersymmetric partner. Common to
³³⁹ most Supersymmetric theories is a stable, weakly interacting Lightest Supersymmetric
³⁴⁰ Partner (**LSP**), which has the properties of a possible dark matter candidate. The **SM**
³⁴¹ and the main principles of Supersymmetric theories are outlined in Chapter 2, with
³⁴² emphasis on placed on how experimental signatures of **SUSY** may reveal themselves at
³⁴³ the **LHC**.

344 The experimental goal of the **LHC** is to further test the framework of the **SM**,
345 exploring the TeV mass scale for the first time, and to seek a connection between the
346 particles produced in proton collisions and dark matter. The first new discovery by
347 this extraordinary machine was announced on the 4th of July 2012. The long-awaited
348 discovery was the culmination decades of experimental endeavours in the search for the
349 Higgs boson, providing an answer to the mechanism of electroweak symmetry breaking
350 within the **SM** [3][4].

351 This discovery was made possible through data taken by the two multi purpose
352 detectors (**CMS** and A Toroidal LHC ApparatuS (**ATLAS**)) located on the **LHC** ring.
353 An experimental description of the **CMS** detector and the **LHC** is described in Chapter 3,
354 including some of the object reconstruction used by **CMS** in searches for **SUSY** signatures.
355 The performance of the **CMS** Level-1 calorimeter trigger, benchmarked by the author is
356 also included within this chapter.

357 The analysis conducted by the author is detailed within Chapter 4. This chapter
358 contains a description of the search for evidence of the production of Supersymmetric
359 particles at the **LHC**. The main basis of the search centres around the kinematic
360 dimensionless α_T variable, which provides strong rejection of backgrounds with fake
361 missing energy signatures whilst maintaining good sensitivity to a variety of **SUSY**
362 topologies. The author's work as an integral part of the analysis group is documented in
363 detail, which has culminated in numerous publications over the past two years. The latest
364 of which was published in the European Physical Journal C (**EPJC**) [5] and contains the
365 results which are discussed within this and the sequential Chapter.

366 The author in particular has played a major role in the extension of the α_T analysis into
367 the additional b-tagged and jet multiplicity dimensions increasing the sensitivity of the
368 analysis to a range of **SUSY** topologies. Additionally the author has worked extensively
369 in both increasing the statistical precision of electroweak predictions measured from
370 simulation through analytical techniques, and the derivation of a data driven systematic
371 uncertainty through the establishment of closure tests within the control samples of the
372 analysis.

373 Additionally a method to search for **SUSY** signatures which are rich in top and bottom
374 flavoured jet final states is disscussd in Chapter 5. A parametrisation of the b-tagging
375 distribution for different Electroweak processes is used to establish templates, which
376 are then used to estimate the expected number of 3 or 4 b-tagged jet events from **SM**

377 processes. The α_T search is used as a cross check for this template method to establish
378 it's functionality.

379 Finally the interpretation of such results within the framework of a variety of Simplified
380 Model Spectra (**SMS**), which describe an array of possible **SUSY** event topologies is
381 documented in Chapter 6. A description of the statistical model used to derive these
382 interpretations and the possible implications of the results presented in this thesis is
383 discussed within this Chapter. Natural units are used throughout this thesis in which \hbar
384 = c = 1.

Chapter 2.

³⁸⁵ A Theoretical Overview

³⁸⁶ Within this chapter, a brief introduction and background to the **SM** is given. Its success
³⁸⁷ as a rigorously tested and widely accepted theory is discussed as well as the deficiencies
³⁸⁸ with this theory that hint there this theory is not a complete description of our universe.
³⁸⁹ The motivations for new physics at the TeV scale and in particular Supersymmetric
³⁹⁰ theories are outlined within Section (2.3), with the chapter concluding with how an
³⁹¹ experimental signature of such theories can be produced and observed at the **LHC**,
³⁹² Section (2.4).

³⁹³ 2.1. The Standard Model

³⁹⁴ The **SM** is the name given to the relativistic Quantum Field Theory (**QFT**), where
³⁹⁵ particles are represented as excitations of fields, which describes the interactions and
³⁹⁶ properties of all the known elementary particles [6][7][8][9]. It is a renormalisable field
³⁹⁷ theory which contains three symmetries: $SU(3)$ for colour charge, $SU(2)$ for weak isospin
³⁹⁸ and $U(1)$ relating to weak hyper charge, which require its Lagrangian \mathcal{L}_{SM} to be invariant
³⁹⁹ under local gauge transformation.

⁴⁰⁰ Within the **SM** theory, matter is composed of spin $\frac{1}{2}$ fermions, which interact with each
⁴⁰¹ other via the exchange of spin-1 gauge bosons. A summary of the known fundamental
⁴⁰² fermions and bosons is given in Table 2.1.

⁴⁰³ Fermions are separated into quarks and leptons of which only quarks interact with
⁴⁰⁴ the strong nuclear force. Quarks unlike leptons are not seen as free particles in nature,
⁴⁰⁵ but rather exist only within baryons, composed of three quarks with an overall integer
⁴⁰⁶ charge, and quark-anti-quark pairs called mesons. Both leptons and quarks are grouped

Particle	Symbol	Spin	Charge	Mass (GeV)
First Generation Fermions				
Electron Neutrino	ν_e	$\frac{1}{2}$	0	$< 2.2 \times 10^{-6}$
Electron	e	$\frac{1}{2}$	-1	0.51×10^{-3}
Up Quark	u	$\frac{1}{2}$	$\frac{2}{3}$	$2.3^{+0.7}_{-0.5} \times 10^{-3}$
Down Quark	d	$\frac{1}{2}$	$-\frac{1}{3}$	$4.8^{+0.7}_{-0.3} \times 10^{-3}$
Second Generation Fermions				
Muon Neutrino	ν_μ	$\frac{1}{2}$	0	-
Muon	μ	$\frac{1}{2}$	-1	1.05×10^{-3}
Charm Quark	c	$\frac{1}{2}$	$\frac{2}{3}$	1.275 ± 0.025
Strange Quark	s	$\frac{1}{2}$	$-\frac{1}{3}$	$95 \pm 5 \times 10^{-3}$
Third Generation Fermions				
Tau Neutrino	ν_τ	$\frac{1}{2}$	0	-
Tau	τ	$\frac{1}{2}$	-1	1.77
Top Quark	t	$\frac{1}{2}$	$\frac{2}{3}$	173.5 ± 0.8
Bottom Quark	b	$\frac{1}{2}$	$-\frac{1}{3}$	4.65 ± 0.03
Gauge Bosons				
Photon	γ	1	0	0
W Boson	W^\pm	1	± 1	80.385 ± 0.015
Z Boson	Z	1	0	91.187 ± 0.002
Gluons	g	1	0	0
Higgs Boson	H	0	0	125.3 ± 0.5 [4]

Table 2.1.: The fundamental particles of the SM, with spin, charge and mass displayed. Latest mass measurements taken from [1].

407 into three generations which have the same properties, but with ascending mass in each
 408 subsequent generation.

409 The gauge bosons mediate the interactions between fermions. The field theories
 410 of Quantum Electro-Dynamics (QED) and Quantum Chromo-Dynamics (QCD), yield
 411 massless mediator bosons, the photon and eight coloured gluons which are consequences
 412 of the gauge invariance of those theories, detailed in Section (2.1.1).

413 The unification of the electromagnetic and weak-nuclear forces into the current
 414 Electroweak theory yield the weak gauge bosons, W^\pm and Z through the mixing of the
 415 associated gauge fields. The force carriers of this theory were experimentally detected by
 416 the observation of weak neutral current, discovered in 1973 in the Gargamelle bubble

⁴¹⁷ chamber located at European Organization for Nuclear Research (**CERN**) [10], with the
⁴¹⁸ masses of and the weak gauge bosons measured by the UA1 and U2 experiments at the
⁴¹⁹ Super Proton Synchrotron (**SPS**) collider in 1983 [11][12].

⁴²⁰ 2.1.1. Gauge Symmetries of the SM

⁴²¹ Symmetries are of fundamental importance in the description of physical phenomena.
⁴²² Noether's theorem states that for a dynamical system, the consequence of any symmetry
⁴²³ is an associated conserved quantity [13]. Invariance under translations, rotations, and
⁴²⁴ Lorentz transformations in physical systems lead to conservation of momentum, energy
⁴²⁵ and angular momentum.

⁴²⁶ In the **SM**, a quantum theory described by Lagrangian formalism, the weak, strong and
⁴²⁷ electromagnetic interactions are described in terms of “gauge theories”. A gauge theory
⁴²⁸ possesses invariance under a set of “local transformations”, which are transformations
⁴²⁹ whose parameters are space-time dependent. The requirement of gauge invariance within
⁴³⁰ the **SM** necessitates the introduction of force-mediating gauge bosons and interactions
⁴³¹ between fermions and the bosons themselves. Given the nature of the topics covered by
⁴³² this thesis, the formulation of **EWK** within the **SM** Lagrangian is reviewed within this
⁴³³ section.

⁴³⁴ The simplest example of the application of the principle of local gauge invariance
⁴³⁵ within the **SM** is in Quantum Electro-Dynamics (**QED**), the consequences of which
⁴³⁶ require a massless photon field [14][15].

⁴³⁷ Starting from the free Dirac Lagrangian written as

$$\mathcal{L} = \bar{\psi}(i\gamma^\mu \partial_\mu - m)\psi, \quad (2.1)$$

⁴³⁸ where ψ represents a free non interacting fermionic field, with the matrices $\gamma^\mu, \mu \in$
⁴³⁹ $0, 1, 2, 3$ defined by the anti commutator relationship $\gamma^\mu \gamma^\nu + \gamma^\nu \gamma^\mu = 2\eta^{\mu\nu} I_4$ where $\eta^{\mu\nu}$ is
⁴⁴⁰ the flat space-time metric $(+, -, -, -)$ and I_4 is the 4×4 identity matrix.

⁴⁴¹ Under a local $U(1)$ abelian gauge transformation in which ψ transforms as:

$$\psi(x) \rightarrow \psi'(x) = e^{i\theta(x)}\psi(x) \quad \bar{\psi}(x) \rightarrow \bar{\psi}'(x) = e^{i\theta(x)}\bar{\psi}(x) \quad (2.2)$$

⁴⁴² the kinetic term of the Lagrangian does not remain invariant, due to the partial
⁴⁴³ derivative interposed between the $\bar{\psi}$ and ψ yielding,

$$\partial_\mu \psi \rightarrow e^{i\theta(x)} \partial_\mu \psi + i e^{i\theta(x)} \psi \partial_\mu \theta. \quad (2.3)$$

⁴⁴⁴ To ensure that \mathcal{L} remains invariant, a modified derivative, D_μ , that transforms
⁴⁴⁵ covariantly under phase transformations is introduced. In doing this a vector field A_μ
⁴⁴⁶ with transformation properties that cancel out the unwanted term in (2.3) must also be
⁴⁴⁷ included,

$$D_\mu \equiv \partial_\mu - ieA_\mu, \quad A_\mu \rightarrow A_\mu + \frac{1}{e} \partial_\mu \theta. \quad (2.4)$$

⁴⁴⁸ Invariance of the Lagrangian is then achieved by replacing ∂_μ by D_μ :

$$\begin{aligned} \mathcal{L} &= i\bar{\psi}\gamma^\mu D_\mu \psi - m\bar{\psi}\psi \\ &= \bar{\psi}(i\gamma^\mu \partial_\mu - m)\psi + e\bar{\psi}\gamma^\mu \psi A_\mu \end{aligned} \quad (2.5)$$

⁴⁴⁹ An additional interaction term is now present in the Lagrangian, coupling the Dirac
⁴⁵⁰ particle to this vector field, which is interpreted as the photon in QED. To regard this
⁴⁵¹ new field as the physical photon field, a term corresponding to its kinetic energy must be
⁴⁵² added to the Lagrangian from Equation (2.5). Since this term must also be invariant
⁴⁵³ under the conditions of Equation (2.4), it is defined in the form $F_{\mu\nu} = \partial^\mu A^\nu - \partial^\nu A^\mu$.

⁴⁵⁴ This then leads to the Lagrangian of QED:

$$\mathcal{L}_{QED} = \underbrace{i\bar{\psi}\gamma^\mu\partial_\mu\psi - \frac{1}{4}F_{\mu\nu}F^{\mu\nu}}_{\text{kinetic term}} + \underbrace{m\bar{\psi}\psi}_{\text{mass term}} + \underbrace{e\bar{\psi}\gamma^\mu\psi A_\mu}_{\text{interaction term}} \quad (2.6)$$

455 Within the Lagrangian there remains no mass term of the form $m^2A_\mu A^\mu$, which is
 456 prohibited by gauge invariance. This implies that the gauge particle, the photon, must
 457 be massless.

458 2.1.2. The Electroweak Sector and Electroweak Symmetry 459 Breaking

460 The same application of gauge symmetry and the requirement of local gauge invariance
 461 can be used to unify QED and the Weak force in the Electroweak Sector (EWK).
 462 The nature of EWK interactions is encompassed within a Lagrangian invariant under
 463 transformations of the group $SU(2)_L \times U(1)_Y$.

464 The weak interactions from experimental observation [16], are known to violate parity
 465 and are therefore not symmetric under interchange of left and right helicity fermions.
 466 Thus within the SM the left and right handed parts of these fermion fields are treated
 467 separately. A fermion field is then split into two left and right handed chiral components,
 468 $\psi = \psi_L + \psi_R$, where $\psi_{L/R} = (1 \pm \gamma^5)\psi$.

469 The $SU(2)_L$ group is the special unitary group of 2×2 matrices U satisfying $UU^\dagger = I$
 470 and $\det(U) = 1$. It may be written in the form $U = e^{-i\omega_i T_i}$, with the generators of the
 471 group $T_i = \frac{1}{2}\tau_i$ where τ_i , $i \in 1,2,3$ being the 2×2 Pauli matrices

$$\tau_1 = \begin{pmatrix} 0 & 1 \\ 1 & 0 \end{pmatrix} \quad \tau_2 = \begin{pmatrix} 0 & -i \\ i & 0 \end{pmatrix} \quad \tau_3 = \begin{pmatrix} 1 & 0 \\ 0 & -1 \end{pmatrix}, \quad (2.7)$$

472 which form a non Abelian group obeying the commutation relation $[T^a, T^b] \equiv$
 473 $if^{abc}T^c \neq 0$. The gauge fields that accompany this group are represented by $\hat{W}_\mu =$
 474 $(\hat{W}_\mu^1, \hat{W}_\mu^2, \hat{W}_\mu^3)$ and act only on the left handed component of the fermion field ψ_L .

⁴⁷⁵ One additional generator Y which represents the hypercharge of the particle under
⁴⁷⁶ consideration is introduced through the $U(1)_Y$ group acting on both components of the
⁴⁷⁷ fermion field, with an associated vector boson field \hat{B}_μ .

⁴⁷⁸ The $SU(2)_L \times U(1)_Y$ transformations of the left and right handed components of ψ
⁴⁷⁹ are summarised by,

$$\begin{aligned}\chi_L &\rightarrow \chi'_L = e^{i\theta(x) \cdot T + i\theta(x)Y} \chi_L, \\ \psi_R &\rightarrow \psi'_R = e^{i\theta(x)Y} \psi_R,\end{aligned}\tag{2.8}$$

⁴⁸⁰ where the left handed fermions form isospin doubles χ_L and the right handed fermions
⁴⁸¹ are isosinglets ψ_R . For the first generation of leptons and quarks this represents

$$\begin{aligned}\chi_L &= \begin{pmatrix} \nu_e \\ e \end{pmatrix}_L, & \begin{pmatrix} u \\ d \end{pmatrix}_L \\ \psi_R &= e_R, & u_R, d_R\end{aligned}\tag{2.9}$$

⁴⁸² Imposing local gauge invariance within \mathcal{L}_{EWK} is once again achieved by modifying
⁴⁸³ the covariant derivative

$$D_\mu = \partial_\mu - \frac{ig}{2} \tau^i W_\mu^i - \frac{ig'}{2} Y B_\mu,\tag{2.10}$$

⁴⁸⁴ where g and g' are the coupling constant of the $SU(2)_L$ and $U(1)_Y$ groups respectively.
⁴⁸⁵ Taking the example of the first generation of fermions defined in Equation.(2.9), with input
⁴⁸⁶ hypercharge values of -1 and -2 for χ_L and e_R respectively, would lead to a Lagrangian
⁴⁸⁷ \mathcal{L}_1 of the form,

$$\begin{aligned}\mathcal{L}_1 = &\bar{\chi}_L \gamma^\mu [i\partial_\mu - g \frac{1}{2} \tau \cdot W_\mu - g' (-\frac{1}{2}) B_\mu] \chi_L \\ &+ \bar{e}_R \gamma^\mu [i\partial_\mu - g' (-1) B_\mu] e_R - \frac{1}{4} W_{\mu\nu} \cdot W^{\mu\nu} - \frac{1}{4} B_{\mu\nu} B^{\mu\nu}.\end{aligned}\tag{2.11}$$

⁴⁸⁸ As in **QED**, these additional gauge fields introduce field strength tensors $B_{\mu\nu}$ and
⁴⁸⁹ $W_{\mu\nu}$,

$$\hat{B}_{\mu\nu} = \partial_\mu \hat{B}_\nu - \partial_\nu \hat{B}_\mu \quad (2.12)$$

$$\hat{W}_{\mu\nu} = \partial_\mu \hat{W}_\nu - \partial_\nu \hat{W}_\mu - g \hat{W}_\mu \times \hat{W}_\nu \quad (2.13)$$

⁴⁹⁰ corresponding to the kinetic energy and self coupling of the W_μ fields and the kinetic
⁴⁹¹ energy term of the B_μ field.

⁴⁹² None of these gauge bosons are physical particles, and instead linear combinations of
⁴⁹³ these gauge bosons make up γ and the W and Z bosons, defined as

$$W^\pm = \frac{1}{\sqrt{2}} (W_\mu^1 \mp i W_\mu^2) \quad \begin{pmatrix} Z_\mu \\ A_\mu \end{pmatrix} = \begin{pmatrix} \cos\theta_W & -\sin\theta_W \\ \sin\theta_W & \cos\theta_W \end{pmatrix} \begin{pmatrix} W_\mu^3 \\ B_\mu \end{pmatrix} \quad (2.14)$$

⁴⁹⁴ where the mixing angle, $\theta_w = \tan^{-1} \frac{g'}{g}$, relates the coupling of the neutral weak and
⁴⁹⁵ electromagnetic interactions.

⁴⁹⁶ As in the case of the formulation of the **QED** Lagrangian there remains no mass term
⁴⁹⁷ for the photon. However this is also the case for the W, Z and fermions in the Lagrangian,
⁴⁹⁸ contrary to experimental measurement. Any explicit introduction of mass terms would
⁴⁹⁹ break the symmetry of the Lagrangian and instead mass terms can be introduced through
⁵⁰⁰ spontaneous breaking of the **EWK** symmetry via the Higgs mechanism.

⁵⁰¹ The Higgs mechanism induces spontaneous symmetry breaking through the introduc-
⁵⁰² tion of a complex scalar SU(2) doublet field ϕ which attains a non-zero Vacuum
⁵⁰³ Expectation Value (**VEV**) [17][18][19][20].

$$\phi = \begin{pmatrix} \phi^+ \\ \phi^0 \end{pmatrix} \quad \text{with} \quad \begin{aligned} \phi^+ &\equiv (\phi_1 + i\phi_2)/\sqrt{2} \\ \phi^0 &\equiv (\phi_3 + i\phi_4)/\sqrt{2} \end{aligned} \quad (2.15)$$

504 The Lagrangian defined in Equation (2.11) attains an additional term \mathcal{L}_{Higgs} of the
 505 form

$$\mathcal{L}_{Higgs} = \overbrace{(D_\mu \phi)^\dagger (D^\mu \phi)}^{\text{kinetic}} - \overbrace{\mu^2 \phi^\dagger \phi - \lambda (\phi^\dagger \phi)^2}^{\text{potential } V(\phi)} \quad (\mu^2, \lambda) > 0 \in \mathbb{R},$$

$$\mathcal{L}_{SM} = \mathcal{L}_{EWK} + \mathcal{L}_{Higgs}, \quad (2.16)$$

506 where the covariant derivative D_μ is that defined in Equation (2.10). The last two
 507 terms of \mathcal{L}_{Higgs} correspond to the Higgs potential, in which positive real positive values
 508 of μ^2 and λ are required to ensure the generation of masses for the bosons and leptons.
 509 The minimum of this potential is found at $\phi^\dagger \phi = \frac{1}{2}(\phi_1^2 + \phi_2^2 + \phi_3^2 + \phi_4^2) = \mu^2/\lambda = v^2$,
 510 where v represents the **VEV**.

511 Defining the ground state of the ϕ field to be consistent with the $V(\phi)$ minimum, and
 512 then expanding around a ground state chosen to maintain an unbroken electromagnetic
 513 symmetry thus preserving a zero photon mass [21] leads to

$$\phi_0 = \sqrt{\frac{1}{2}} \begin{pmatrix} 0 \\ v \end{pmatrix}, \quad \phi(x) = e^{i\tau \cdot \theta(x)/v} \sqrt{\frac{1}{2}} \begin{pmatrix} 0 \\ v + h(x) \end{pmatrix}, \quad (2.17)$$

514 where the fluctuations from the vacuum ϕ_0 are parametrized in terms of four real
 515 fields, $\theta_1, \theta_2, \theta_3$ and $h(x)$.

516 Choosing to gauge away the three massless Goldstone boson fields by setting $\theta(x)$ to
 517 zero and substituting $\phi(x)$ back into kinetic term of \mathcal{L}_{Higgs} from Equation (2.16) leads to
 518 mass terms for the W^\pm and Z bosons

$$(D_\mu \phi)^\dagger (D^\mu \phi) = \frac{1}{2}(\partial_\mu h)^2 + \frac{g^2 v^2}{2} W_\mu^+ W^{-\mu} + \frac{v^2 g^2}{8 \cos^2 \theta_w} Z_\mu Z^\mu + 0 A_\mu A^\mu, \quad (2.18)$$

519 where the relations between the physical and electroweak gauge fields from Equation
 520 (2.14) are used. The W^\pm and Z bosons can then be determined to be

$$M_W = \frac{1}{2}gv \quad M_Z = \frac{1}{2} \frac{gv}{\cos \theta_w}. \quad (2.19)$$

521 This mechanism is also used to generate fermion masses by introducing a Yukawa
 522 coupling between the fermions and the ϕ field [22], with the coupling strength of a particle
 523 to the ϕ field governing its mass. Additionally a scalar boson h with mass $m_h = v\sqrt{\frac{\lambda}{2}}$, is
 524 also predicted as a result of this spontaneous symmetry breaking and became known as
 525 the Higgs boson. Its discovery by the CMS and ATLAS experiments in 2012 is concrete
 526 evidence to support this method of mass generation within the SM.

527 2.2. Motivation for Physics Beyond the Standard 528 Model

529 As has been described, the SM has proved to be a very successful theory, predicting the
 530 existence of the W^\pm and Z bosons and the top quark long before they were experimentally
 531 observed. However the theory does not accurately describe all observed phenomena and
 532 has some fundamental theoretical flaws that hint at the need for additional extensions to
 533 the current theory.

534 On a theoretical level, the SM is unable to incorporate the gravitational interactions
 535 of fundamental particles within the theory. Whilst at the electroweak energy scales the
 536 relative strength of gravity is negligible compared to the other three fundamental forces,
 537 at much higher energy scales $M_{planck} \sim 10^{18} GeV$ quantum gravitational effects become
 538 increasingly dominant. The failure to reconcile gravity within the SM, demonstrates that
 539 the SM must become invalid at some higher energy scale.

540 Some other deficiencies with the SM include the fact that the predicted rate of
 541 Charge-Parity violation does not account for the matter dominated universe which we
 542 inhabit, and the SM prediction of zero neutrino mass conflicts with the observation of
 543 neutrino flavour mixing, attributed to mixing between neutrino mass eigenstates [23][24].

544 Perhaps one of the most glaring gaps in the predictive power of the SM is that there
 545 exists no candidate to explain the cosmic dark matter observed in galactic structures
 546 through indirect techniques including gravitational lensing and measurement of the
 547 orbital velocity of stars in galactic edges. Any such candidate must be very weakly

548 interacting which must also be stable, owing to the lack of direct detection of the decay
 549 products of such an process. Providing a dark matter candidate is of the prime goals
 550 which be tackled by any Beyond Standard Model (**BSM**) physics model.

551 The recent discovery of the Higgs boson whilst a significant victory for the predictive
 552 power of the **SM**, brings with it still unresolved questions. This issue is commonly
 553 described as the “hierarchy problem”.

554 In the absence of new physics between the TeV and Planck scale, calculating beyond
 555 tree-level contributions to the Higgs mass term given by its self interaction, result in
 556 divergent terms that push the Higgs mass up to the planck mass M_{planck} .

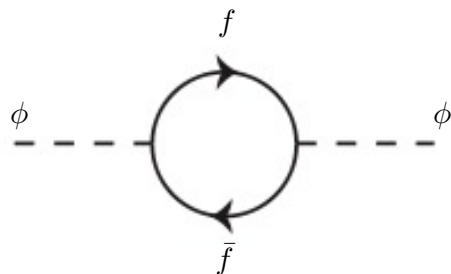


Figure 2.1.: One loop quantum corrections to the Higgs squared mass parameter m_h^2 due to a fermion.

557 This can be demonstrated by considering the one loop quantum correction to the
 558 Higgs mass with a fermion f , shown in Figure 2.1 with mass m_f . The Higgs field couples
 559 to f with a term in the Lagrangian $-\lambda_f h \bar{f} f$, yielding a correction of the form [25],

$$\delta m_h^2 = -\frac{|\lambda_f|^2}{8\pi^2} \Lambda^2 + \dots, \quad (2.20)$$

560 where λ_f represents the coupling strength for each type of fermion $\propto m_f$, and Λ the
 561 cutoff energy scale at which the **SM** ceases to be a valid theory.

562 To recover the mass of the now discovered Higgs boson would require a fine-tuning of
 563 the parameters to cancel out these mass corrections the the Higgs mass to the scale of
 564 30 orders of magnitude. This appears as an unnatural solution to physicists and it is
 565 this hierarchy problem that provides one of the strongest motivations for the theory of
 566 SUperSYmmetry (**SUSY**).

⁵⁶⁷ 2.3. Supersymmetry Overview

⁵⁶⁸ Supersymmetry provides potential solutions to many of the issues raised in the previous
⁵⁶⁹ section. It provides a dark matter candidate, can explain baryogenesis in the early
⁵⁷⁰ universe and also provides an elegant solution to the hierarchy problem [26][27][28][29].
⁵⁷¹ At its heart it represents a new space-time symmetry that relates fermions and bosons.
⁵⁷² This symmetry converts bosonic states into fermionic states, and vice versa, see Equation
⁵⁷³ (2.21) ,

$$Q|Boson\rangle = |Fermion\rangle \quad Q|Fermion\rangle = |Boson\rangle, \quad (2.21)$$

⁵⁷⁴ where the operator Q is the generator of these transformations. Quantum field theories
⁵⁷⁵ which are invariant under such transformations are called supersymmetric.

⁵⁷⁶ This symmetry operator therefore acts upon a particles spin altering it by a half integer
⁵⁷⁷ value. The consequences of the introduction of this additional space-time symmetry
⁵⁷⁸ introduce a new rich phenomenology. For example in supersymmetric theories, both
⁵⁷⁹ the left handed $SU(2)$ doublet and right handed singlet of fermions will have a spin-0
⁵⁸⁰ superpartner, containing the same electric charge, weak isospin, and colour as its **SM**
⁵⁸¹ partner. In the case of the leptons $(\nu_l, l)_L$ will have two superpartners, a sneutrino $\tilde{\nu}_l{}_L$
⁵⁸² and a slepton \tilde{l}_L , whilst the singlet l_R also has a superpartner slepton \tilde{l}_R .

⁵⁸³ Each particle in a supersymmetric theory is paired together with their superpartners
⁵⁸⁴ as a result of this supersymmetric transformations in a so called supermultiplet. These
⁵⁸⁵ superpartners will then consequently also contribute to the corrections to the Higgs mass.
⁵⁸⁶ Bosonic and fermionic loops contributing to the correction appear with opposite signs,
⁵⁸⁷ and therefore cancellation of these divergent terms will stabilise the Higgs mass, solving
⁵⁸⁸ the hierarchy problem [30][31].

⁵⁸⁹ One of the simplest forms of **SUSY** would predict a whole set of supersymmetric
⁵⁹⁰ partners to their **SM** counterparts with the same mass and interactions. However the
⁵⁹¹ currently lack of any experimental evidence for the predicted sparticle spectrum implies
⁵⁹² **SUSY** must be a broken symmetry in which any sparticle masses must be greater than
⁵⁹³ their SM counterparts.

⁵⁹⁴ There exist many techniques which can induce supersymmetric breaking [32][33][34].
⁵⁹⁵ Of particular interest to experimental physicists are those at which the breaking scale

⁵⁹⁶ is of an order that is experimentally accessible to the LHC i.e. \sim TeV scale. Whilst
⁵⁹⁷ there is no requirement for supersymmetric breaking to occur at this energy scale, for
⁵⁹⁸ supersymmetry to provide a solution to the hierarchy problem, it is necessary for this
⁵⁹⁹ scale to not differ too drastically from the EWK scale [35][36].

⁶⁰⁰ 2.3.1. R-Parity

⁶⁰¹ Some supersymmetric theories also present a solution to the dark matter problem. Such
⁶⁰² theories can contain a Lightest Supersymmetric Partner (LSP), which matches the criteria
⁶⁰³ of a Weakly Interacting Massive Particle (WIMP) required by cosmological observation
⁶⁰⁴ if R-parity is conserved.

⁶⁰⁵ Baryon (B) and Lepton (L) number conservation is forbidden in the SM by renor-
⁶⁰⁶ malisability requirements. The violation of Baryon or Lepton number would result in
⁶⁰⁷ the proton lifetime much shorter than those set by experimental limits [37]. Another
⁶⁰⁸ symmetry called R-parity is then often introduced to SUSY theories to maintain baryon
⁶⁰⁹ and lepton conservation.

⁶¹⁰ R-parity is described by the equation

$$R_P = (-1)^{3(B-L)+2s}, \quad (2.22)$$

⁶¹¹ where s represents the spin of the particles. $B = \pm \frac{1}{3}$ for quarks/antiquarks and $B = 0$
⁶¹² for all others, $L = \pm 1$ for leptons/antileptons, $L = 0$ for all others.

⁶¹³ R-parity ensures the stability of the proton in SUSY models, and also has other
⁶¹⁴ consequences for the production and decay of supersymmetric particles. At particle
⁶¹⁵ colliders supersymmetric particles can only be pair produced, and similarly the decay
⁶¹⁶ of any produced supersymmetric particle is restricted to a SM particle and a lighter
⁶¹⁷ supersymmetric particle as allowed by conservation laws. A further implication of R-
⁶¹⁸ parity is that once a supersymmetric particle has decayed to the LSP it remains stable,
⁶¹⁹ unable to decay into a SM particle.

⁶²⁰ A LSP would not interact in a detector at a particle collider, leaving behind a missing
⁶²¹ energy \cancel{E}_T signature. The assumption of R-parity and its consequences are used to
⁶²² determine the physical motivation and search strategies for SUSY model at the LHC.

623 2.4. Experimental signatures of SUSY at the LHC

624 Should strongly interacting sparticles be within the experimental reach of the LHC, then
625 it is expected that they can be produced in a variety of ways.

- 626 • squark/anti-squark and gluino pairs can be produced via both gluon fusion and
627 quark/anti-quark scattering.
- 628 • a gluino and squark produced together via quark-gluon scattering
- 629 • squark pairs produced via quark-quark scattering

630 Whilst most SUSY searches invoke the requirement of R-parity to explore parameter
631 phase space, there still exist a whole plethora of possible SUSY model topologies which
632 could be discovered at the LHC.

633 During the 2011 run period at a $\sqrt{s} = 7$ TeV particular models were used to benchmark
634 performance and experimental reach of both CMS searches and previous experiments.
635 The Compressed Minimal SuperSymmetric Model (CMSSM) was initially chosen for a
636 number of reasons [38]. One of the most compelling being the reduction from the up to
637 105 new parameters introduced by SUSY in addition to the existing 19 of the SM to that
638 of just 5 free extra free parameters. It was this simplicity, combined with the theory not
639 requiring any fine tuning of particle masses to produce the experimentally verified SM
640 that made it an attractive model to interpret physics results.

641 However recent results from the LHC now strongly disfavour large swathes of CMSSM
642 parameter space [39][40][41]. In the face of such results a more pragmatic model indepen-
643 dent search strategy is now applied across most SUSY searches at the LHC, see Section
644 (2.4.1).

645 As previously stated, a stable LSP that exhibits the properties of a dark matter would
646 be weakly interacting and therefore will not be directly detected in a detector environment.
647 Additionally the cascade decays of supersymmetric particles to the LSP would also result
648 in significant hadronic activity. These signatures can then be characterised through
649 large amounts of hadronic jets (see Section (3.3.1)), leptons and a significant amount of
650 missing energy dependent upon the size of the mass splitting between the LSP and the
651 supersymmetric particle it has decayed from.

652 Whilst the SM contains processes which can exhibit a similar event topology to that
653 described above. The largest contribution of which comes in from the general QCD

654 environment of a hadron collider. A multitude of different analytical techniques are used
655 by experimental physicists to reduce or estimate any reducible or irreducible backgrounds,
656 allowing a possible **SUSY** signature to be extracted. The techniques employed within
657 this thesis are described in great detail within Section (4.1).

658 2.4.1. Simplified Models

659 With such a variety of different ways for a **SUSY** signal to manifest itself, it is necessary
660 to be able to interpret experimental reach through the masses of gluinos and squarks
661 which can excluded by experimental searches rather than on a model specific basis.

662 This is accomplished through **SMS** models, which are defined by a set of hypothetical
663 particles and a sequence of their production and decay [42][43]. In the **SMS** models
664 considered within this thesis, only the production process for the two primary particles
665 are considered. Each primary particle can undergo a direct or a cascade decay through
666 an intermediate new particle. At the end of each decay chain there remains a neutral,
667 undetected **LSP** particle, denoted $\tilde{\chi}_{LSP}$ which can represent a neutralino or gravitino.
668 Essentially it is easier to consider each **SMS** with branching ratios set to 100% The
669 masses of the primary particle and the **LSP** remain as free parameters, in which the
670 absolute value and relative difference between the primary and **LSP** particle alter the
671 kinematics of the event.

672 Different **SMS** models are denoted with a T-prefix, with a summary of the types
673 interpreted within this thesis listed below [44].

- 674 • **T1,T1xxxx**, models represent a simplified version of gluino pair production with
675 each gluino (superpartner to the gluon) undergoing a three-body decay to a quark-
676 antiquark pair and the **LSP** (i.e. $\tilde{g} \rightarrow q\bar{q}\tilde{\chi}_{LSP}$). The resultant final state from this
677 decay is typically 4 jets + \cancel{E}_T in the absence of initial/final state radiation and
678 detector effects. xxxx denotes models in which the quarks are of a specific flavour,
679 typically t or b quark-antiquarks.
- 680 • **T2,T2xx**, models represent a simplified version of squark anti-squark production
681 with each squark undergoing a two-body decay into a light-flavour quark and **LSP**
682 (i.e. $\tilde{q} \rightarrow q\tilde{\chi}_{LSP}$). This results in final states with less jets than gluino mediated
683 production, typically 2 jets + \cancel{E}_T when again ignoring the effect of initial/final state
684 radiation and detector effects. xx models again represent decays in which both the
685 quark and the squark within the decay is of a specific flavour, typically \tilde{t}/t or \tilde{b}/b .

Models rich in b and t quarks are interpreted within this thesis as they remain of particular interest within “Natural SUSY” scenarios [45][46]. The largest contribution to the quadratic divergence in the Higgs mass parameter comes from a loop of top quarks via the Yukawa coupling. Cancellation of these divergences can be achieved in supersymmetric theories by requiring a light right handed top squark, \tilde{t}_R , and left-handed double $SU(2)_L$ doublet containing top and bottom squarks, $(\tilde{\frac{t}{b}})_L$ [47].

These theories therefore solve the hierarchy problem by predicting light \sim EWK scale third generation sleptons, to be accessible at the LHC. Search strategies involving the requirement of b-tagging (see Section (3.3.2)) are used to give sensitivity to these type of SUSY scenarios and are discussed in greater detail within Chapter 6.

Two example decay chains are shown in Figure 2.2; the pair production of gluinos (T1) and the pair production of squarks (T2) decaying into SM particles and LSP’s.

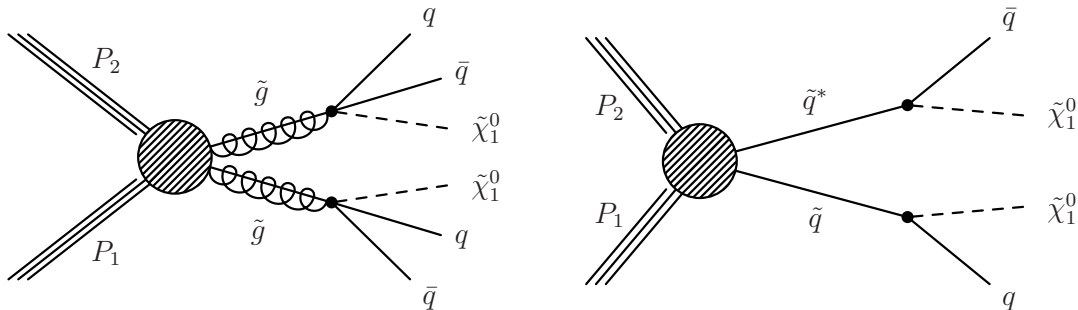


Figure 2.2.: Two example SMS model decays (T1 (left), T2 (right)), which are used in interpretations of physics reach by CMS.

Chapter 3.

⁶⁹⁸ The LHC and the CMS Detector

⁶⁹⁹ Probing the SM for signs of new physics would not be possible without the immensely
⁷⁰⁰ complex electronics and machinery that makes the TeV energy scale accessible for the
⁷⁰¹ first time. This chapter will cover the LHC based at European Organization for Nuclear
⁷⁰² Research (CERN) and the Compact Muon Solenoid (CMS) detector, being the experiment
⁷⁰³ the author is a member of. Section (3.2) serves to introduce an overview of the different
⁷⁰⁴ components of the CMS detector, with more detail spent on those that are relevant in
⁷⁰⁵ the search for Supersymmetric particles. Section (3.3) will focus on event and object
⁷⁰⁶ reconstruction again with more emphasis on jet level quantities which are most relevant
⁷⁰⁷ to the author's analysis research. Finally Section (3.4) will cover work performed by
⁷⁰⁸ the author, as service to the CMS Collaboration, in measuring the performance of the
⁷⁰⁹ Global Calorimeter Trigger (GCT) component of the L1 trigger during the 2012-2013
⁷¹⁰ run period.

⁷¹¹ 3.1. The LHC

⁷¹² The LHC is a storage ring, accelerator, and collider of circulating beams of protons or
⁷¹³ ions. Housed in the tunnel dug for the Large Electron-Positron collider (LEP), it is
⁷¹⁴ approximately 27 km in circumference, 100 m underground, and straddles the border
⁷¹⁵ between France and Switzerland outside of Geneva. It is currently the only collider
⁷¹⁶ in operation that is able to study physics at the TeV scale. A double-ring circular
⁷¹⁷ synchrotron, it was designed to collide both proton-proton (pp) and heavy ion (PbPb)
⁷¹⁸ with a centre of mass energy $\sqrt{s} = 14$ TeV at a final design luminosity of $10^{34}\text{cm}^{-2}\text{s}^{-1}$.

⁷¹⁹

These counter-circulating beams of protons/Pb ions are merged in four sections around the ring to enable collisions of the beams, with each interaction point being home to one of the four major experiments; A Large Ion Collider Experiment (**ALICE**) [48], A Toroidal LHC ApparatuS (**ATLAS**) [49], Compact Muon Solenoid (**CMS**) [50] and Large Hadron Collider Beauty (**LHC-B**) [51] which record the resultant collisions. The layout of the **LHC** ring is shown in Figure 3.1. The remaining four sections contain acceleration, collimation and beam dump systems. In the eight arc sections, the beams are steered by magnetic fields of up to 8 T provided by super conduction dipole magnets, which are maintained at temperatures of 2 K using superfluid helium. Additional magnets for focusing and corrections are also present in straight sections within the arcs and near the interaction regions where the detectors are situated.

731

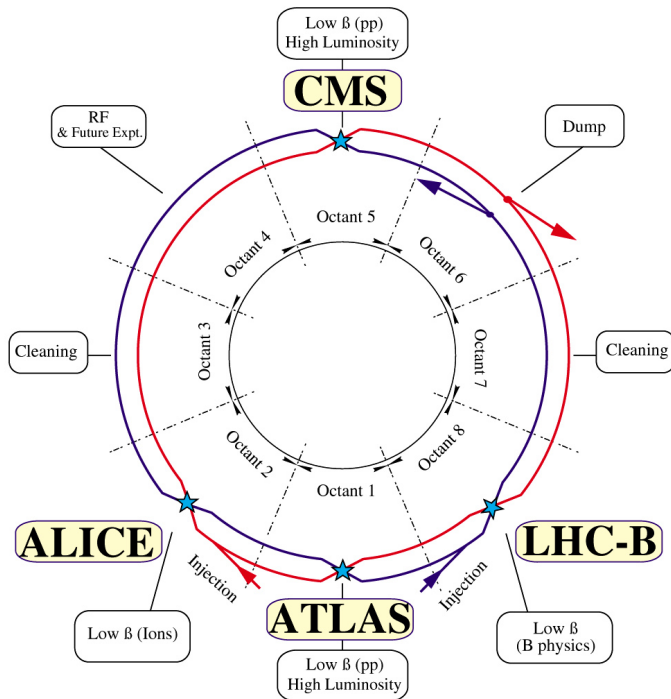


Figure 3.1.: A top down layout of the LHC. [52], with the position of the four main detectors labelled.

Proton beams are formed inside the Proton Synchrotron (**PS**) from bunches of protons 50 ns apart with an energy of 26 GeV. The protons are then accelerated in the Super Proton Synchrotron (**SPS**) to 450 GeV before being injected into the **LHC**. These **LHC** proton beams consists of many “bunches” i.e. approximately 1.1×10^{11} protons localized into less than 1 ns in the direction of motion. Before collision the beams are ramped to 4

736

737 TeV (2012) per beam in a process involving increasing the current passing through the
 738 dipole magnets. Once the desired \sqrt{s} energy is reached then the beams are allowed to
 739 collide at the interaction points. The luminosity falls regularly as the run progresses as
 740 protons are lost in collisions, and eventually the beam is dumped before repeating the
 741 process again.

742

743 Colliding the beams produced an instantaneous luminosity of approximately $5 \times$
 744 $10^{33} \text{ cm}^{-2}\text{s}^{-1}$ during the 2012 run. The high number of protons in each bunch increases
 745 the likelihood of multiple interactions with each crossing of the counter-circulating
 746 beams. This leads to isotropic energy depositions within the detectors positioned at these
 747 interaction points, increasing the energy scale of the underlying event. This is known as
 748 pile-up and the counteracting of it's effects are important to the many measurements
 749 performed at the LHC.

750 In the early phase of prolonged operation after the initial shutdown the machine
 751 operated in 2010-2011 at 3.5 TeV per beam, $\sqrt{s} = 7 \text{ TeV}$, delivering 6.13 fb^{-1} of data
 752 [53]. During the 2012-2013 run period, data was collected at an increased $\sqrt{s} = 8 \text{ TeV}$
 753 improving the sensitivity of searches for new physics. Over the whole run period 23.3
 754 fb^{-1} of data was delivered of which 21.8 fb^{-1} was recorded by the CMS detector as shown
 755 in Figure 3.2 [53]. A total of 12 fb^{-1} of 8 TeV certified data was collected by October
 756 2012, and it is this data which forms the basis of the results discussed within this thesis.

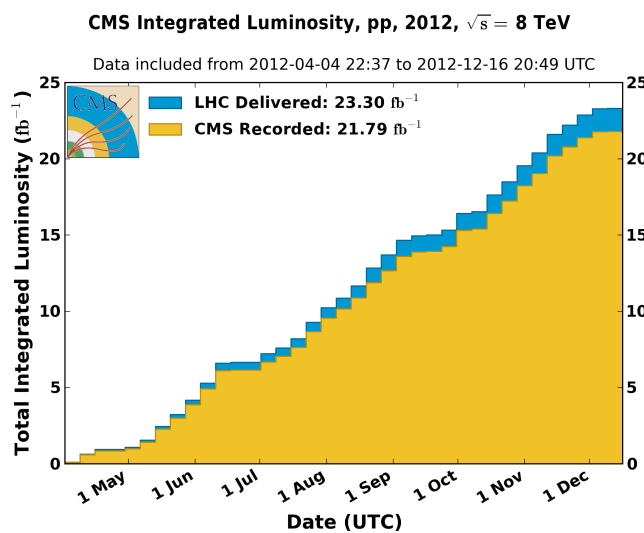


Figure 3.2.: The total integrated luminosity delivered to and collected by CMS during the 2012 8 TeV pp runs.

757 3.2. The CMS detector

758 The Compact Muon Solenoid (**CMS**) detector is one of two general purpose detectors
 759 at the **LHC** designed to search for new physics. The detector is designed to provide
 760 efficient identification and measurement of many physics objects including photons,
 761 electrons, muons, taus, and hadronic showers over wide ranges of transverse momentum
 762 and direction. Its nearly 4π coverage in solid angle allows for accurate measurement of
 763 global transverse momentum imbalance. These design factors give **CMS** the ability to
 764 search for direct production of **SUSY** particles at the TeV scale, making the search for
 765 Supersymmetric particles one of the highest priorities among the wide range of physics
 766 programmes at **CMS**.

767

768 **CMS** uses a right-handed Cartesian coordinate system with the origin at the interaction
 769 point and the z-axis pointing along the beam axis, the x-axis points radially inwards to
 770 the centre of the collider ring, with the y-axis points vertically upward. The azimuthal
 771 angle, ϕ ranging between $[-\pi, \pi]$ is defined in the x-y plane starting from the x-axis. The
 772 polar angle θ is measured from the z axis. The common convention in particle physics is
 773 to express an out going particle in terms of ϕ and its pseudorapidity defined as

$$\eta = -\log \tan \left(\frac{\theta}{2} \right). \quad (3.1)$$

774 The variable $\Delta R = \sqrt{\Delta\phi^2 + \Delta\eta^2}$ is commonly used to define angular distance
 775 between objects within the detector and additionally energy and momentum is typically
 776 measured in the transverse plane perpendicular to the beam line. These values are
 777 calculated from the x and y components of the object and are denoted as $E_T = E \sin \theta$
 778 and $p_T = \sqrt{p_x^2 + p_y^2}$.

779 3.2.1. Detector Subsystems

780 As the range of particles produced in pp collisions interact in different ways with mat-
 781 ter, **CMS** is divided into subdetector systems, which perform complementary roles to
 782 identify the identity, mass and momentum of the different physics objects present in
 783 each event. These detector sub-systems contained inside **CMS** are wrapped in layers

784 around a central 13 m long 4 T super conducting solenoid as shown in Figure 3.3. With
 785 the endcaps closed , CMS is a cylinder of length 22 m, diameter 15 m, and mass 12.5
 786 kilotons. A more detailed complete description of the detector can be found elsewhere [50].
 787

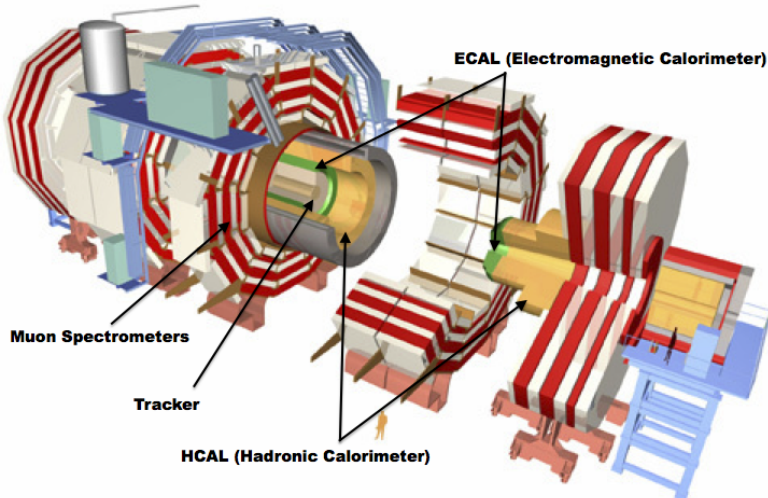


Figure 3.3.: A pictorial depiction of the CMS detector with the main detector subsystems labelled. [54]

788 3.2.2. Tracker

789 The inner-most subdetector of the barrel is the multi-layer silicon tracker, formed of a
 790 pixel detector component encased by layers of silicon strip detectors. The pixel detector
 791 consists of three layers of silicon pixel sensors providing measurements of the momentum,
 792 position coordinates of the charged particles as they pass, and the location of primary
 793 and secondary vertices between 4cm and 10cm transverse to the beam. Outside the pixel
 794 detector, ten cylindrical layers of silicon strip detectors extend the tracking system out to
 795 a radius of 1.20m from the beam line. The tracking system provides efficient and precise
 796 determination of the charges, momenta, and impact parameters of charged particles with
 797 the geometry of the tracker extending to cover a rapidity range up to $|\eta| < 2.5$.
 798

799 The tracking system also plays a crucial part in the identification of jets originating
 800 from b-quarks through measurement of displaced secondary vertices, which is covered in
 801 more detail in Section (3.3.2). The identification of b-jets is important in many searches

802 for natural SUSY models and forms an important part of the inclusive search strategy
803 described within Section (4.2).

804 **3.2.3. Electromagnetic Calorimeter**

805 Immediately outside of the tracker, but still within the magnet core, sits the Electromag-
806 netic CALorimeter (**ECAL**). Covering a pseudorapidity up to $|\eta| < 3$ and comprising
807 of over 75,000 PbWO₄ (lead tungstate) crystals that scintillate as particles deposit energy,
808 the **ECAL** provides high resolution measurements of the electromagnetic showers from
809 photons, electrons in the detector.

810

811 Lead tungstate is used because of its short radiation length ($X_0 \sim 0.9\text{cm}$) and small
812 Molieré radius ($\sim 2.1\text{cm}$) leading to high granularity and resolution. It's fast scintillation
813 time ($\sim 25\text{ns}$) reduces the effects of pile-up due to energy from previous collisions still
814 being read out, and its radiation hardness gives it longevity. The crystals are arranged
815 in modules which surround the beam line in a non-projective geometry, angled at 3°
816 with respect to the interaction point to minimise the risk of particles escaping down the
817 cracks between the crystals.

818

819 The **ECAL** is primarily composed of two sections, the Electromagnetic CALorime-
820 ter Barrel (**EB**) which extends in pseudo-rapidity to $|\eta| < 1.479$ with a crystal front
821 cross section of $22 \times 22 \text{ mm}^2$ and a length of 230 mm corresponding to 25.8 radia-
822 tion lengths, and the Electromagnetic CALorimeter Endcap (**EE**) covering a rapidity
823 range of $1.479 < |\eta| < 3.0$, which consists of two identical detectors on either side of
824 the **EB**. A lead-silicon sampling ‘pre-shower’ detector Electromagnetic CALorimeter
825 pre-Shower (**ES**) is placed before the endcaps to aid in the identification of neutral pions.
826 Their arrangement are shown in Figure 3.4.

827

828 Scintillation photons from the lead tungstate crystals are instrumented with Avalanche
829 Photo-Diodes (**APD**) and Vacuum Photo-Triodes (**VPT**) located in the **EB** and **EE**
830 respectively, converting the scintillating light into an electric signal which is consequently
831 used to determine the amount of energy deposited within the crystal . These instruments
832 are chosen for their resistance under operation to the strong magnetic field of **CMS**. The
833 scintillation of the **ECAL** crystals as well as the response of the **APDs** varies as a function

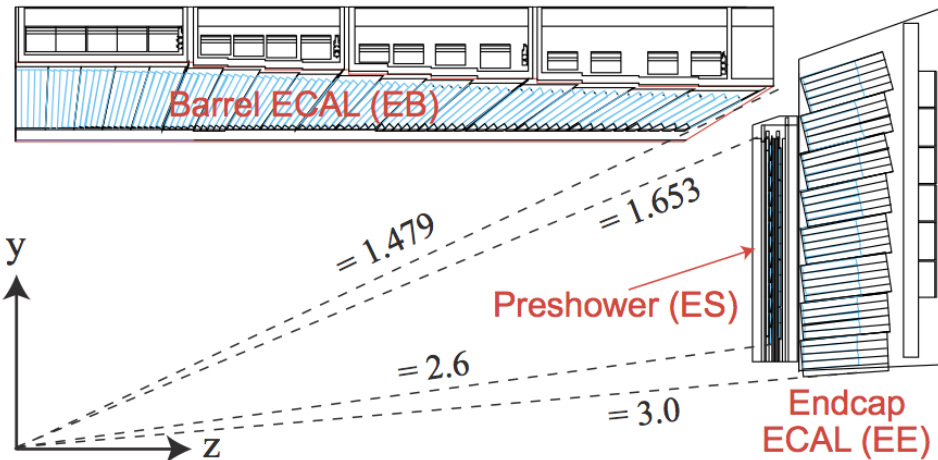


Figure 3.4.: Illustration of the **ECAL** showing the arrangement of the lead tungstate crystals in the **EB** and **EE**. The **ES** is also shown and is located in front of the **EE** [55].

834 of temperature and so cooling systems continually maintain an overall constant **ECAL**
 835 temperature $\pm 0.05^\circ C$.

836 3.2.4. Hadronic Calorimeter

837 Beyond the **ECAL** lies the Hadronic CALorimeter (**HCAL**) which is responsible for
 838 the accurate measurement of hadronic showers, crucial for analyses involving jets or
 839 missing energy signatures. The **HCAL** is a sampling calorimeter which consists of al-
 840 ternating layers of brass absorber and plastic scintillator, except in the hadron forward
 841 ($3.0 < |\eta| < 5.0$) region in which steel absorbers and quartz fibre scintillators are used
 842 because of their increased radiation tolerance. Hadron showers are initiated in the
 843 absorber layers inducing scintillation in the plastic scintillator tiles. These scintillation
 844 photons are converted by wavelength shifting fibres for read-out by hybrid photodiodes.
 845

846 The **HCAL**'s size is constrained to a compact size by the presence of the solenoid,
 847 requiring the placement of an additional outer calorimeter on the outside of the solenoid
 848 to increase the sampling depth of the **HCAL**. A schematic of the **HCAL** can be seen in
 849 Figure 3.5.

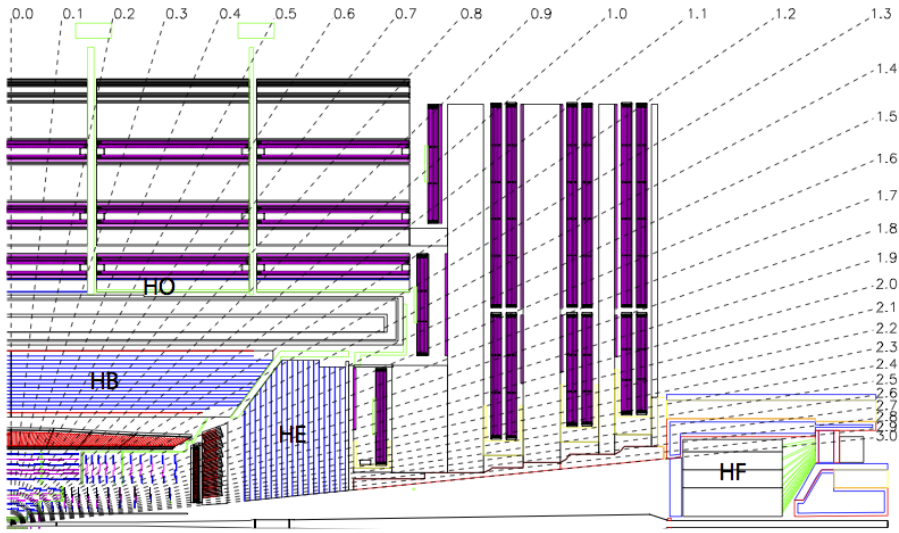


Figure 3.5.: Schematic of the hadron calorimeters in the r - z plane, showing the locations of the **HCAL** components and the **HF**. [50].

851 The **HCAL** covers the range $|\eta| < 5$ and consists of four subdetectors: the Hadron
 852 Barrel (**HB**) $|\eta| < 1.3$, the Hadron Outer (**HO**), the Hadron Endcaps (**HE**) $1.3 < |\eta| < 3.0$
 853 and the Hadron Forward (**HF**). The **HB** is contained between the outer edge of the **ECAL**
 854 and the inner edge of the solenoid, formed of 36 azimuthal wedges it is split between
 855 two half-barrel segments. Each wedge is segmented into four azimuthal angle (ϕ) sectors,
 856 and each half-barrel is further segmented into 16 η towers. The electronic readout chain,
 857 channels the light from the active scintillator layers from one ϕ -segment and all η -towers
 858 of a half-barrel to a Hybrid Photo Diode (**HPD**).

859 The relatively short number of interaction lengths (λ_l , the distance a hadron will
 860 travel through the absorber material before it has lost $\frac{1}{e}$ of its energy) within the **HB**,
 861 the lowest being $\lambda_l = 5.82$ for $|\eta| = 0$, facilitates the need for the ‘tail catching’ **HO**
 862 to increase the sampling depth in the central barrel rapidity region $|\eta| < 1.3$ to 11
 863 interaction lengths . Significant fractions of the hadrons energy will be deposited in the
 864 **ECAL** as it passed through the detector. Therefore measurements of hadron energies
 865 in the central regions $|\eta| < 3.0$ use both the **ECAL** and **HCAL** to reconstruct the true
 866 energy from showering hadrons.

867 **3.2.5. Muon Systems**

868 Muons being too massive to radiate away energy via Bremsstrahlung, interact little in
869 the calorimeters and mostly pass through the detector until they reach the system of
870 muon detectors which forms the outer most part of the **CMS** detector.

871 Outside of the superconducting solenoid are four muon detection layers interleaved
872 with the iron return yokes which measure the muons energy via ionisation of gas within
873 detector elements. Three types of gaseous chamber are used. The Drift Tube (**DT**),
874 Cathode Stripe Chamber (**CSC**), and Resistive Plate Chamber (**RPC**) systems provide
875 efficient detection of muons with pseudo-rapidity $|\eta| < 2.4$. The best reconstruction
876 performance is obtained when the muon chamber is combined with the inner tracking
877 information to determine muon trajectories and their momenta [56].

878

879 **3.3. Event Reconstruction and Object Definition**

880 The goal of event reconstruction is to take the raw information recorded by the detector
881 and to compute from it higher-level quantities which can be used at an analysis level.
882 These typically correspond to an individual particle’s energy and momenta, or groups of
883 particles which shower in a narrow cone and the overall global energy and momentum
884 balance of the event. The reconstruction of these objects are described in great detail in
885 [57], however covered below are brief descriptions of those which are most relevant to the
886 analysis detailed in Chapter 4.

887 **3.3.1. Jets**

888 Quarks and gluons are produced copiously at the LHC in the hard scattering of partons.
889 As these quarks and gluons fragment, they hadronise and decay into a group of strongly
890 interactive particles and their decay products. These streams of particles travel in the
891 same direction, as they have been “boosted” by the momentum of the primary hadron.
892 These collections of decay products are reconstructed and identified together as a “jet”.

893 At **CMS** jets are reconstructed from energy deposits in the detector using the anti-kt
894 algorithm [58] with size parameter $\Delta R = 0.5$. The anti-kt jet algorithm clusters jets by
895 defining a distance between hard (high p_T) and soft (low p_T) particles such that soft

896 particles are preferentially clustered with hard particles before being clustered between
897 themselves. This produces jets which are robust to soft particle radiation from the pile-up
898 conditions experienced at the **LHC**.

899

900 There are two main type of jet reconstruction used at **CMS**, Calorimeter (Calo) and
901 Particle Flow (PF) jets [59]. Calorimeter jets are reconstructed using both the **ECAL**
902 and **HCAL** cells, combined into calorimeter towers . These calorimeter towers consist of
903 geometrically matched **HCAL** cells and **ECAL** crystals. Electronics noise is suppressed by
904 applying a threshold to the calorimeter cells, with pile-up effects reduced by a requirement
905 placed on the tower energy [60]. Calorimter jets are the jets used within the analyses
906 described in this thesis.

907 PF jets are formed from combining information from all of the **CMS** subdetectors
908 systems to determine which final state particles are present in the event. Generally,
909 any particle is expected to produce some combination of a track in the silicon tracker,
910 a deposit in the calorimeters, or a track in the muon system. The PF jet momentum
911 and spatial resolutions are greatly improved with respect to calorimeter jets, as the use
912 of the tracking detectors and of the high granularity of **ECAL** allows resolution and
913 measurement of charged hadrons and photons inside a jet, which together constitute \sim
914 85% of the jet energy [61].

915 The jets reconstructed by the clustering algorithm in **CMS** typically have an energy
916 that differs to the ‘true’ energy measured by a perfect detector. This stems from the
917 non-linear and nonuniform response of the calorimeters as well as other residual effects
918 including pile-up and underlying events, and therefore additional corrections are applied
919 to recover a uniform relative response as a function of pseudo-rapidity. These are applied
920 as separate sub corrections [62].

- 921 • A PU correction is first applied to the jet. It subtracts the average extra energy
922 deposited in the jet that comes from other vertices present in the event and is
923 therefore not part of the hard jet itself.
- 924 • p_T and η dependant corrections derived from Monte Carlo simulations are used to
925 account for the non-uniform response of the detector.
- 926 • p_T and η residual corrections are applied to data only to correct for difference
927 between data and Monte Carlo. The residual is derived from QCD dijet samples
928 and the p_T residual from $\gamma+$ jet and $Z+$ jets samples in data.

929 **3.3.2. B-tagging**

930 The decays of b quarks are suppressed by small CKM matrix elements. As a result, the
931 lifetimes of b-flavoured hadrons, produced in the fragmentation of b quarks, are relatively
932 long; \mathcal{O} 1ps. The identification of jets origination from b quarks is very important for
933 searches for new physics and for measurements of standard model processes.

934

935 Many different algorithms developed by CMS select b-quark jets based on variables
936 such as the impact parameters of the charged-particle tracks, the properties of recon-
937 structed decay vertices, and the presence or absence of a lepton, or combinations thereof
938 [63]. One of the most efficient of which is the Combined Secondary Vertex (CSV) which
939 operates based on secondary vertex and track-based lifetime information, benchmarked
940 in ‘Loose’, ‘Medium’ and ‘Tight’ working points, of which the medium point is the tagger
941 used within the α_T search detailed in Section (4.1).

942 Using the CSV tagger, a likelihood-based discriminator distinguishes between jets
943 from b-quarks, and those from charm or light quarks and gluons, which is shown in Figure
944 3.6. The minimum thresholds on the discriminator for each working point correspond to
945 the misidentification probability for light-parton jets of 10%, 1%, and 0.1%, respectively,
946 in jets with an average p_T of about 80 GeV.

947 The b-tagging performance is evaluated to measure the b-jet tagging efficiency ϵ_b ,
948 and the misidentification probability of charm ϵ_c and light-parton jets ϵ_s . The tagging
949 efficiencies for each of these three jet flavours are compared between data and MC
950 simulation, from which a series of p_T and $|\eta|$ binned jet corrections are determined,

$$SF_{b,c,s} = \frac{\epsilon_{b,c,s}^{data}}{\epsilon_{b,c,s}^{MC}}. \quad (3.2)$$

951 These are collectively named ‘Btag Scale Factors’ and allow MC simulation to accu-
952 rately reflect the running conditions and performance of the tagging algorithm in data.
953 Understanding of the b-tagging efficiency is essential in order to minimise systematic
954 uncertainties in physics analyses that employ b-tagging.

955

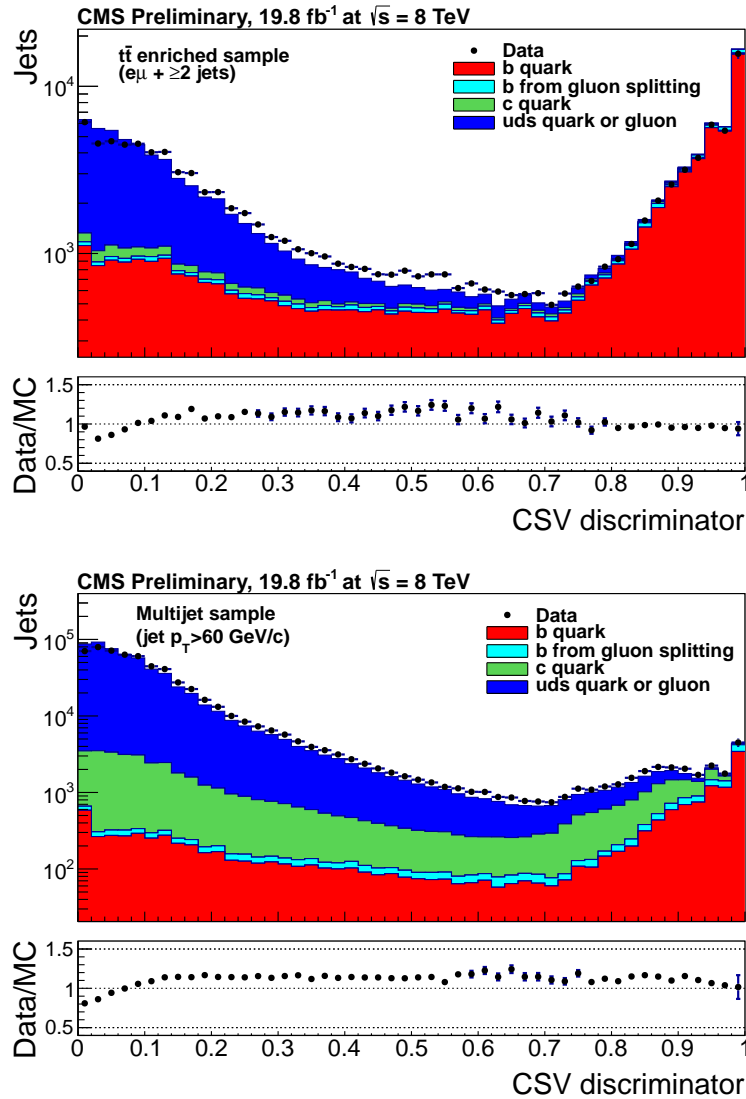


Figure 3.6.: CSV algorithm discriminator values in enriched $t\bar{t}$ (top) and inclusive multi jet samples (bottom) for b,c and light flavoured jets [64]. Working points are determined from the misidentification probability for light-parton jets to be tagged as a b-jet and are given as 0.244, 0.679 and 0.898 for L,M and T working points respectively.

956 The b-tagging efficiency is measured in data using several methods applied to multi
 957 jet events, primarily based on a sample of jets enriched in heavy flavour content. One
 958 method requires the collection of events with a soft muon within a cone $\Delta R < 0.4$ around
 959 the jet axis. Because the semileptonic branching fraction of b hadrons is significantly
 960 larger than that for other hadrons, these jets are more likely to arise from b quarks than
 961 from another flavour, with the resultant momentum component of the muon transverse
 962 to the jet axis larger for muons from b-hadron decays than from light or charm jets.

963 Additionally the performance of the tagger can also be benchmarked in $t\bar{t}$ events where
 964 in the SM, the top quark is expected to decay to a W boson and a b quark about 99.8%
 965 of the time [1]. Further selection criteria is applied to these events to further enrich the
 966 b quark content of these events. The methods to identify b-jets in data are discussed
 967 in great detail at [65]. The jet flavours are determined in simulation using truth level
 968 information and are compared to data to determine the correction scale factors (SF_b),
 969 which are displayed for the CSVM tagger in Figure 3.7.

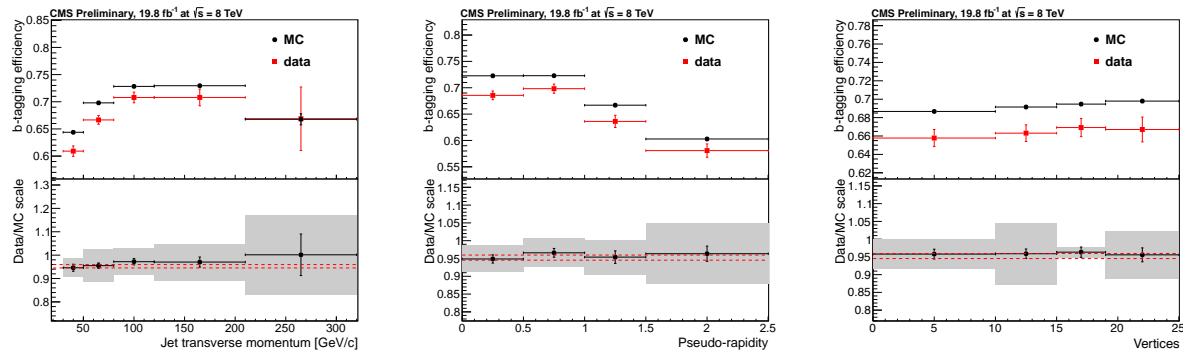


Figure 3.7.: Measured in $t\bar{t} \rightarrow$ di-lepton events using the CSVM tagger: (upper panels) b-tagging efficiencies and (lower panels) data/MC scale factor SF_b as a function of (left) jet p_T , (middle) jet $|\eta|$ and (right) number of primary vertices. In the lower panels, the grey filled areas represent the total statistical and systematic uncertainties, whereas the dotted lines are the average SF_b values within statistical uncertainties.

970 The measurement of the misidentification probability for light-parton jets relies on
 971 the inversion of tagging algorithms, selecting non-b jets using the same variables and
 972 techniques used in benchmarking the b-tagging efficiency. The scale factors (SF_s) to be
 973 applied to MC are shown in Figure 3.8 for the CSVM tagger.

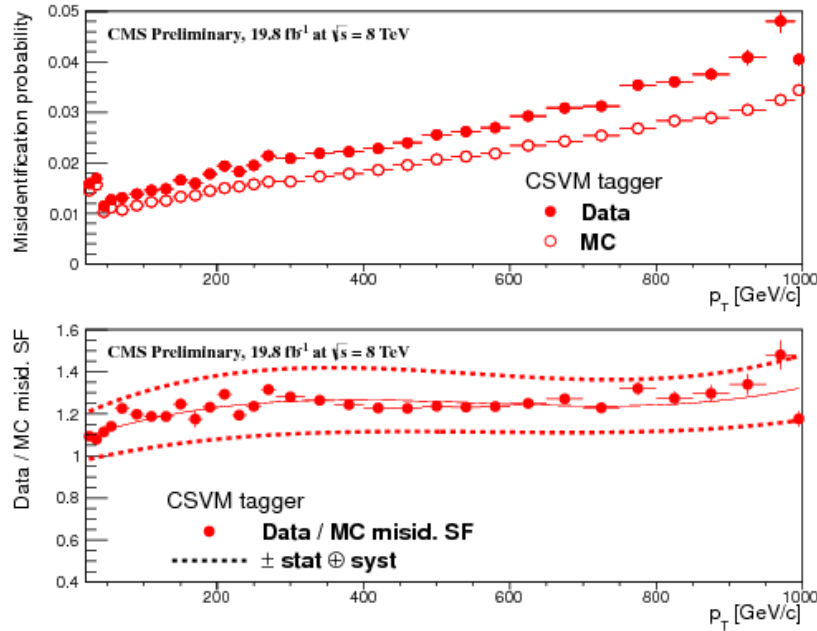


Figure 3.8.: For the **CSV**M tagging criterion: (top) misidentification probability in data (filled circles) and simulation (open circles); (bottom) scale factor for the misidentification probability. The last p_T bin in each plot includes all jets with $p_T > 1000$ GeV. The solid curve is the result of a polynomial fit to the data points. The dashed curves represent the overall statistical and systematic uncertainties on the measurements.

974 3.4. Triggering System

975 With bunch crossings separated by just 25 ns, the rate at which data from all collisions
 976 would have to be written out and processed would be unfeasible. A two-tiered triggering
 977 system is applied at **CMS** in order to cope with the high collision rate of protons. The
 978 **CMS** trigger is designed to use limited information from each event to determine whether
 979 to record the event, reducing the rate of data taking to manageable levels whilst ensuring
 980 a high efficiency of interesting physics object events are selected.

981 The **L1** is a pipelined, dead-timeless system based on custom-built electronics [66],
 982 and is a combination of several sub systems which is shown pictorially in Figure 3.9. The
 983 L1 system is covered in more detail within the following section along with a description
 984 of the service work undertaken by the author to benchmark the performance of the L1
 985 calorimeter trigger during the 2012 8 TeV run period.

986 The Higher Level Trigger (**HLT**) is a large farm of commercial computers [67]. The
 987 **HLT** processes events with software reconstruction algorithms that are more detailed,
 988 giving performance more similar to the reconstruction used offline. The **HLT** reduces

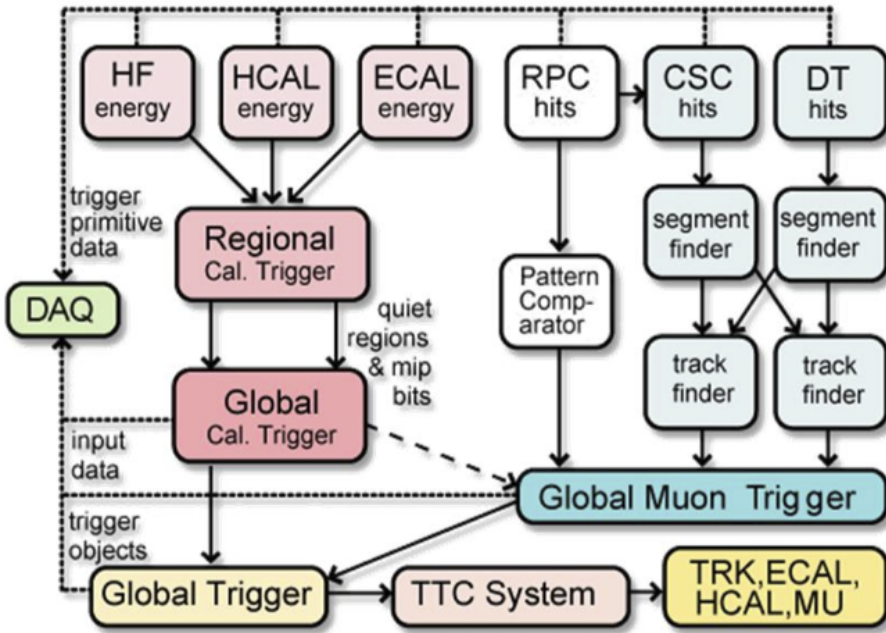


Figure 3.9.: The CMS L1 Trigger system.

the event rate written to disk by a factor of ~ 500 ($\sim 200\text{Hz}$). The recorded events are transferred from CMS to the CERN computing centre, where event reconstruction is performed, and then distributed to CMS computing sites around the globe for storage and analysis.

3.4.1. The Level-1 Trigger

The L1 trigger reduces the rate of events collected from 40 MHz to $\sim 100\text{ kHz}$ using information from the calorimeters and muon chambers, but not the tracker. A tree system of triggers is used to decide whether to pass on an event to the HLT for further reconstruction. Firstly the calorimeter and muon event information is kept separate, with local reconstruction of objects ($\mu, e, \gamma, \text{jets}$) performed by the Regional Calorimeter Trigger (RCT) and Regional Muon Trigger (RMT) respectively. The RCT generates up to 72 isolated and non-isolated electromagnetic objects. These are sorted by rank, which is equivalent to transverse energy E_T , with the four highest ranked electromagnetic objects being passed via the Global Calorimeter Trigger (GCT) and Global MuonTrigger (GMT) to the Global Trigger (GT).

1004 In the L1 **GCT**, coarse measurements of the energy deposited in the electromagnetic
1005 and hadronic calorimeters are combined and by using sophisticated algorithms the
1006 following physics objects are formed:

- 1007 • isolated and non-isolated electromagnetic objects (e and γ);
- 1008 • hadronic jets in the central and forward sections of the hadronic calorimeters;
- 1009 • hadronically decaying tau leptons;
- 1010 • total transverse energy (E_T), the scalar sum of the energy measured at L1, and
1011 missing transverse energy (\cancel{E}_T), defined as the vector sum of the energy of L1
1012 objects;
- 1013 • total transverse jet energy (H_T), the scalar sum of the energy of all L1 jet objects,
1014 and missing transverse jet energy (\cancel{H}_T), defined as the vector sum of the energy of
1015 L1 jets, are calculated from uncorrected L1 jets.

1016 In addition quantities suitable for triggering minimum bias events, forward physics and
1017 beam background events are calculated. Additionally relevant muon isolation information
1018 is also passed on to the **GMT** for decisions involving the muon triggers where it is
1019 combined with information from across the three muon sub-systems. The resultant final
1020 accept/reject decision at **L1** is then performed by the **GT** based on the objects received
1021 from the **GCT** and **GMT** (e/γ , μ , jets, E_T , \cancel{E}_T , H_T).

1022 The L1 trigger is therefore of upmost importance to the functioning of the detector.
1023 Without a high-performing trigger and a good understanding of its performance, there
1024 would be no data to analyse. Observations of how the L1 trigger performance is affected
1025 by changing **LHC** running conditions over the 2012 run period and also the introduction
1026 of a jet seed threshold to the L1 jet trigger algorithm is presented in the following Sections
1027 (3.4.2 - 3.4.6).

1028 3.4.2. L1 Trigger Jet Algorithm

1029 The L1 jet trigger uses the transverse energy sums computed in the calorimeter (both
1030 hadronic and electromagnetic) trigger regions. Each region consists of 4×4 trigger tower
1031 windows, spanning a region of $\Delta\eta \times \Delta\phi = 0.087 \times 0.087$ in pseudorapidity-azimuth. The
1032 jet trigger uses a 3×3 calorimeter region (112 trigger towers) sliding window technique
1033 which spans the full (η, ϕ) coverage of the **CMS** calorimeter as shown in Figure 3.10.

1034 In forming a L1 jet is it required that the central region to be higher than the eight
1035 neighbouring regions $E_{T\text{central}} > E_{T\text{surround}}$. Additionally a minimum threshold of 5 GeV
1036 on $E_{T\text{central}}$ was introduced during the 2012 run period to suppress noise from pile-up,
1037 the effects of which are shown in Section (3.4.4).

1038 The L1 jets are characterised by the E_T , summed over the 3×3 calorimeter regions,
1039 which corresponds to 12×12 trigger towers in barrel and endcap or 3×3 larger **HF**
1040 towers in the **HF**. The ϕ size of the jet window is the same everywhere, whilst the η
1041 binning gets somewhat larger at high η due to calorimeter and trigger tower segmentation.
1042 The jets are labelled by (η, ϕ) indexes of the central calorimeter region.

1043 Jets with $|\eta| > 3.0$ are classified as forward jets, whereas those with $|\eta| < 3.0$ are
1044 classified as central. The four highest energy central, forward and τ jets in the calorimeter
1045 are passed through Look Up Table (**LUT**)'s, which apply a programmable η -dependent
1046 jet energy scale correction. These are then used to make L1 trigger decisions.

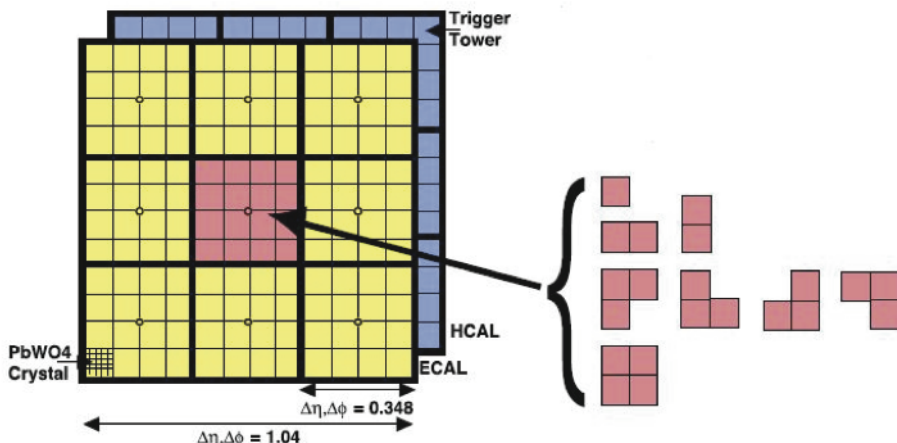


Figure 3.10.: Illustration of the Level-1 jet finding algorithm.

1047 The performance of the L1 jets is evaluated with respect to offline jets, which are
1048 taken from the standard Calo jet and the PF jet reconstruction algorithms of **CMS**.
1049 Jets are corrected for pile-up and detector effects as described in 3.3.1. A moderate
1050 level of noise rejection is applied to the offline jets by selecting jets passing the “loose
1051 identification criteria for both Calo and PF. These criteria are summarised in Appendix
1052 (A).

1053 **3.4.3. Measuring L1 Jet Trigger Efficiencies**

1054 The L1 jet efficiency is defined as the fraction of leading offline jets which were matched
1055 with a L1 tau or central jet above a certain trigger threshold, divided by all the leading
1056 offline jets in the event. This quantity is then plotted as a function of the offline jet E_T ,
1057 η and ϕ .

1058 The efficiency is determined by matching the L1 and reconstructed offline jets spatially
1059 in $\eta - \phi$ space. This is done by calculating the minimum separation in ΔR between the
1060 highest offline reconstructed jet in E_T ($E_T > 10$ GeV, $|\eta| < 3$) and any L1 jet. A jet will
1061 be matched if this value is found to be < 0.5 . Should more than one jet satisfy this, the
1062 jet closest in ΔR is taken as the matched jet. The matching efficiency is close to 100%,
1063 above $\sim 30(45)$ GeV for run 2012B(C) data (see Appendix (??)).

1064 Each efficiency curve is fitted with a function which is the cumulative distribution
1065 function of an Exponentially Modified Gaussian (EMG) distribution:

$$\text{f}(x; \mu, \sigma, \lambda) = \frac{\lambda}{2} \cdot e^{\frac{\lambda}{2}(2\mu + \lambda\sigma^2 - 2x)} \cdot \text{erfc}\left(\frac{\mu + \lambda\sigma^2 - x}{\sqrt{2}\sigma}\right) \quad (3.3)$$

where erfc is the complementary error function defined as:

$$\text{erfc}(x) = 1 - \text{erf}(x) = \frac{2}{\sqrt{\pi}} \int_x^\infty e^{-t^2} dt.$$

1067 In this functional form, the parameter μ determines the point of 50% of the plateau
1068 efficiency and the σ gives the resolution. This parametrisation is used to benchmark
1069 the efficiency at the plateau, the turn-on points and resolution for each L1 Jet trigger.
1070 The choice of function is purely empirical. Previous studies used the error function
1071 alone, which described the data well at high threshold values but could not describe the
1072 efficiencies well at lower thresholds [68].

1073 The efficiency turn-on curves for various L1 jet thresholds are evaluated as a function
1074 of the offline reconstructed jet E_T for central jets with $|\eta| < 3$. These are measured using
1075 single isolated μ triggers which have high statistics, and are orthogonal and therefore
1076 unbiased to the hadronic triggers under study. The efficiency is calculated with respect to
1077 offline Calo and PF Jets in Figure 3.11. Table 3.1 shows the values of these parameters,
1078 calculated for three example L1 single jet triggers taken from 2012 8 TeV data.

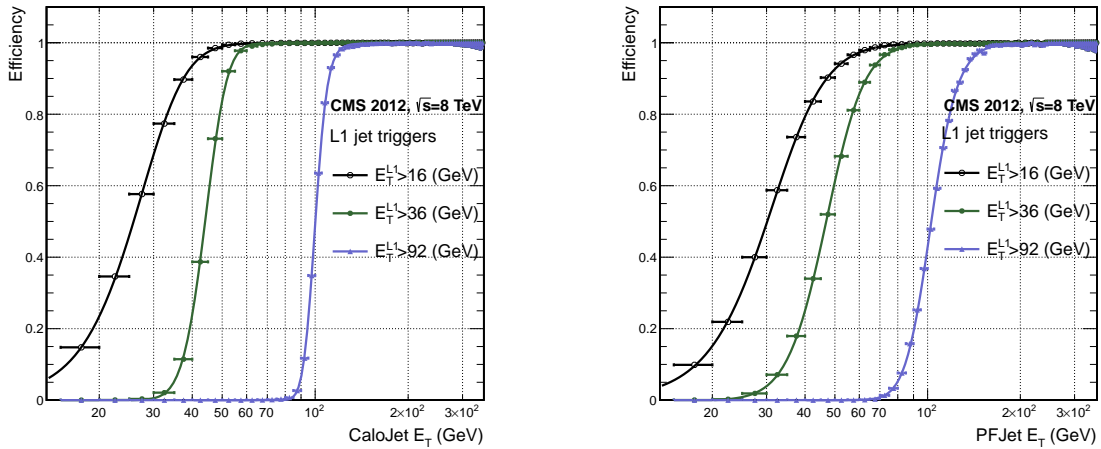


Figure 3.11.: L1 jet efficiency turn-on curves as a function of the offline CaloJet E_T (left) and PFJet E_T (right), measured in 2012 Run Period C data and collected with an isolated single μ data sample.

Trigger	Calo		PF	
	μ	σ	μ	σ
L1_SingleJet16	21.09 \pm 0.03	7.01 \pm 0.02	22.17 \pm 0.04	7.83 \pm 0.03
L1_SingleJet36	41.15 \pm 0.05	5.11 \pm 0.02	39.16 \pm 0.06	8.04 \pm 0.03
L1_SingleJet92	95.36 \pm 0.13	5.62 \pm 0.03	90.85 \pm 0.19	11.30 \pm 0.10

Table 3.1.: Results of a cumulative EMG function fit to the turn-on curves for L1 single jet triggers in run 2012 Run Period C, measured in an isolated μ data sample. The turn-on point, μ , and resolution, σ , of the L1 jet triggers are measured with respect to offline Calo Jets (left) and PF Jets (right).

1079 The results from the L1 single jet triggers shows good performance for both Calo and

1080 PF jets. A better resolution for Calo jets with respect to L1 jets quantities is observed.

1081 This effect is due to Calo jet reconstruction using the same detector systems as in L1 jets,

1082 whereas with PF jet construction using tracker and muon information, a more smeared

1083 resolution when compared to L1 is expected.

1084 3.4.4. Effects of the L1 Jet Seed

1085 Between run period B and C of the 2012 data taking period, a jet seed threshold was
 1086 introduced into the L1 trigger jet algorithm. There was previously no direct requirement
 1087 made on the energy deposited in the central region. The introduction of a jet seed

threshold required that the central region have $E_T \geq 5\text{ GeV}$, and was introduced to counteract the effects of high pile up running conditions which create a large number of soft non-collimated jets, that are then added to the jets from the primary interaction or other soft jets from other secondary interactions [69]. This in turn causes a large increase in trigger rate due to the increase in the likelihood that the event causes the L1 trigger to fire. This was implemented to maintain trigger thresholds by cutting the rate of events recorded without significant reduction in the efficiency of physics events of interest.

The effect of the introduction of this jet seed threshold between these two run periods is benchmarked through a comparison of the efficiency of the L1 jet triggers with respect to offline Calo jets shown in Figure 3.12, and the L1 H_T trigger efficiency in Figure 3.14 which is compared to offline H_T constructed from Calo jets with $E_T \geq 40\text{ GeV}$.

To negate any effects from different pile-up conditions in the run periods, the efficiencies are measured in events which contain between 15 and 20 primary vertices as defined in Appendix (A.2).

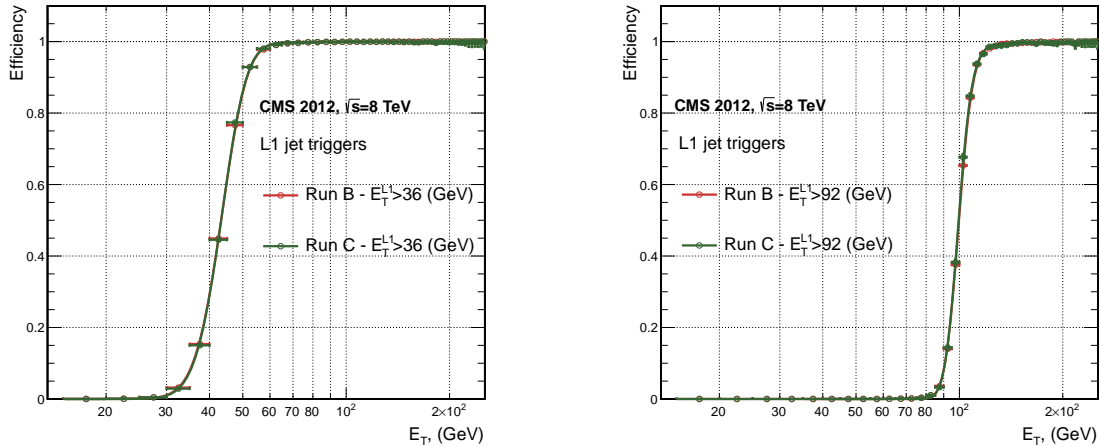


Figure 3.12.: L1 jet efficiency turn-on curves as a function of the offline CaloJet E_T , measured for the L1 SingleJet 36 and 92 trigger in 2012 run period B and C collected with an isolated single μ' sample.

It can be seen that the performance of the $E_T > 36, 92$ single jet are almost identical, with the jet seed having no measurable effect on these triggers as shown in Table 3.2 .

For the H_T triggers, a large increase in rate during high pile-up conditions is expected. This is due to the low energy threshold required for a jet to be added to the L1 H_T sum, which is compiled from all uncorrected L1 jets formed in the RCT. The introduction of the jet seed threshold removes the creation of many of these soft low E_T jets, thus

Trigger	2012B		2012C	
	μ	σ	μ	σ
L1_SingleJet36	40.29 ± 0.04	5.34 ± 0.02	40.29 ± 0.11	5.21 ± 0.05
L1_SingleJet92	94.99 ± 0.09	5.93 ± 0.06	94.82 ± 0.29	5.74 ± 0.18

Table 3.2.: Results of a cumulative EMG function fit to the turn-on curves for L1 single jet triggers in the 2012 run period B and C, preselected on an isolated muon trigger. The turn-on point μ and resolution σ of the L1 jet triggers are measured with respect to offline Calo Jets in run B (left) and run C (right).

₁₁₀₈ lowering the H_T calculation at L1. The effect on the trigger cross section for L1 H_T 150
₁₁₀₉ trigger can be seen in Figure 3.13.

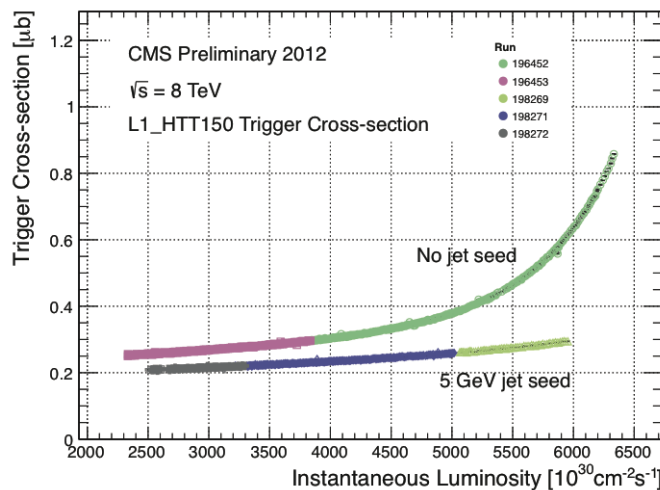


Figure 3.13.: Trigger cross section for the L1HTT150 trigger path. Showing that a 5 GeV jet seed threshold dramatically reduces the dependance of cross section on the instantaneous luminosity for L1 H_T triggers [70].

₁₁₁₀ Different behaviours for the trigger turn ons between these run periods are therefore
₁₁₁₁ expected. The turn on point is observed to shift to higher H_T values after the introduction
₁₁₁₂ of the jet seed threshold, whilst having a sharper resolution due to less pile-up jets being
₁₁₁₃ included the H_T sum, the results are shown in Table 3.3.

₁₁₁₄ 3.4.5. Robustness of L1 Jet Performance against Pile-up

₁₁₁₅ The performance of the L1 single jet triggers is evaluated in different pile-up conditions
₁₁₁₆ to benchmark any dependence on pile-up. Three different pile-up bins of 0-10, 10-20 and
₁₁₁₇ >20 vertices are defined, reflecting the low, medium and high pile-up running conditions

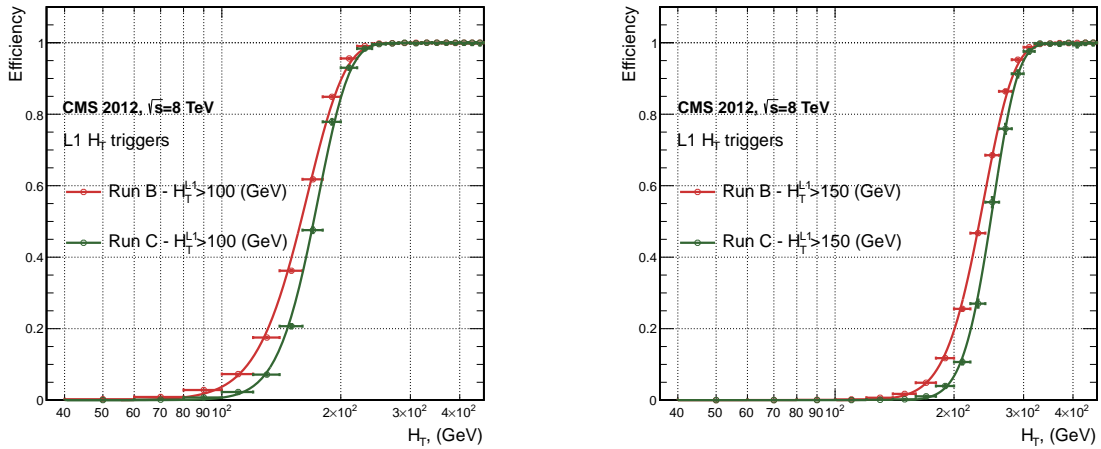


Figure 3.14.: L1 H_T efficiency turn-on curves as a function of the offline CaloJet H_T , measured for the L1 H_T 100 and 150 trigger during the run 2012 B and C collected using an isolated single μ triggered sample.

Trigger	2012B		2012C	
	μ	σ	μ	σ
L1 HT-100	157.5 ± 0.08	32.9 ± 0.08	169.8 ± 0.08	28.7 ± 0.03
L1 H1-150	230.9 ± 0.02	37.3 ± 0.01	246.4 ± 0.16	31.8 ± 0.05

Table 3.3.: Results of a cumulative EMG function fit to the turn-on curves for H_T in run 2012 B and C, preselected on an isolated single μ trigger. The turn-on point μ , resolution σ of the L1 H_T triggers are measured with respect to offline H_T formed from CaloJets with a $E_T \geq 40$ in run period B (left) and C (right).

at CMS in 2012. This is benchmarked relative to Calo and PF jets for the run 2012 C period where the jet seed threshold is applied, with L1 single jet thresholds of 16, 36 and 92 GeV, shown in Figure 3.15. The results of fits to these efficiency turn-on curves are given in Table 3.4 and Table 3.5 for Calo and PF jets respectively.

No significant drop in efficiency is observed in the presence of a high number of primary vertices. The increase in hadronic activity in higher pile-up conditions, combined with the absence of pile-up subtraction for L1 jets, results in the expected observation of a decrease in the μ value of the efficiency turn-ons as a function of pile-up, while the resolution, σ of the turn-ons are found to gradually worsen as expected with increasing pile-up.

These features are further emphasised when shown as a function of

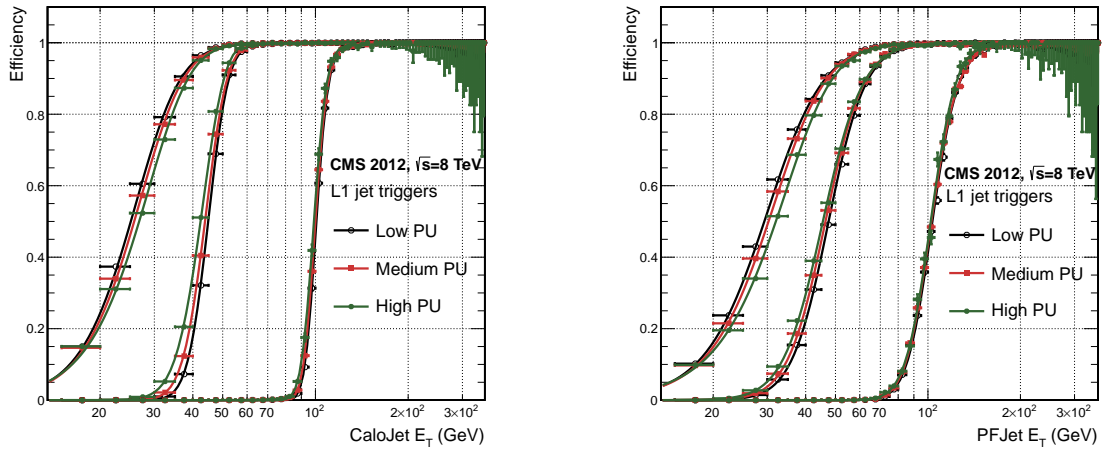


Figure 3.15.: L1 jet efficiency turn-on curves as a function of the leading offline E_T Calo (left) and PF (right) jet, for low, medium and high pile-up conditions.

Vertices	0-10		11-20		> 20	
	μ	σ	μ	σ	μ	σ
L1_SingleJet16	19.9 ± 0.1	6.1 ± 0.3	20.8 ± 0.1	6.5 ± 0.1	22.3 ± 0.2	7.5 ± 0.1
L1_SingleJet36	41.8 ± 0.1	4.6 ± 0.1	40.9 ± 0.1	5.1 ± 0.1	40.6 ± 0.6	5.9 ± 0.2
L1_SingleJet92	95.9 ± 0.2	5.4 ± 0.1	95.2 ± 0.2	5.6 ± 0.1	94.5 ± 0.6	6.2 ± 0.3

Table 3.4.: Results of a cumulative EMG function fit to the efficiency turn-on curves for L1 single jet triggers in the 2012 run period C, measured from isolated μ triggered data. The turn-on point, μ , and resolution, σ , of the L1 jet triggers are measured with respect to offline Calo jets in low (left), medium (middle) and high (right) pile-up conditions.

$$\frac{(L1 E_T - Offline E_T)}{Offline E_T} \quad (3.4)$$

in bins of matched leading offline jet E_T , of which the individual fits can be found in Appendix (B.2). Each of these distributions are fitted with an EMG function as defined in Equation (3.3).

The μ , σ and λ values extracted for the low, medium and high pile-up conditions are shown for Calo and PF jets in Figure 3.16 and Figure 3.17 respectively. The central value of $\frac{(L1 E_T - Offline E_T)}{Offline E_T}$ is observed to increase as a function of jet E_T , whilst the resolution is also observed to improve at higher offline jet E_T .

Vertices	0-10		11-20		> 20	
	μ	σ	μ	σ	μ	σ
L1_SingleJet16	21.1 ± 0.1	7.16 ± 0.05	22.34 ± 0.1	7.9 ± 0.1	24.6 ± 0.2	9.5 ± 0.1
L1_SingleJet36	39.6 ± 0.1	7.4 ± 0.1	38.4 ± 0.1	7.4 ± 0.1	37.1 ± 0.2	7.5 ± 0.1
L1_SingleJet92	91.6 ± 0.3	11.3 ± 0.2	90.4 ± 0.3	11.2 ± 0.1	92.0 ± 0.9	12.1 ± 0.4

Table 3.5.: Results of a cumulative **EMG** function fit to the efficiency turn-on curves for Level-1 single jet triggers in the 2012 run period C, measured from isolated μ triggered data. The turn-on point, μ , and resolution, σ , of the L1 jet triggers are measured with respect to offline PF jets in low (left), medium (middle) and high (right) pile-up conditions.

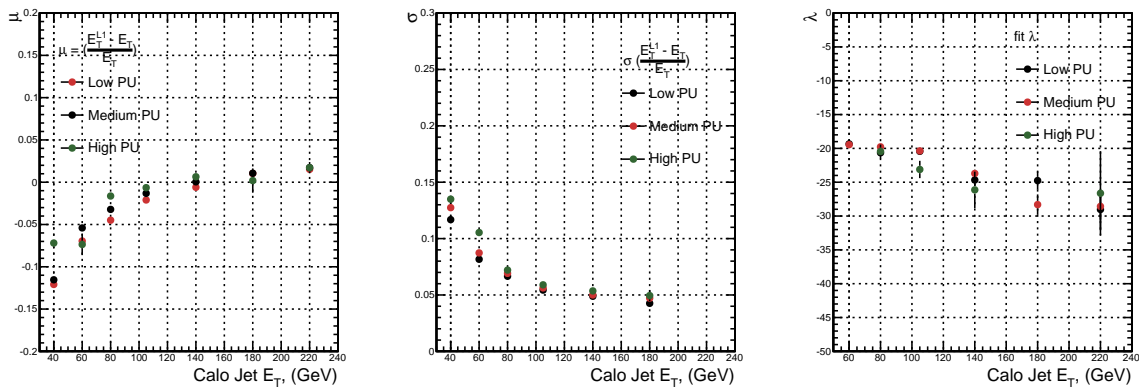


Figure 3.16.: Fit values from an **EMG** function fitted to the resolution plots of leading Calo jet E_T measured as a function of $\frac{(L1 E_T - \text{Offline } E_T)}{\text{Offline } E_T}$ for low, medium and high pile-up conditions. The plots show the mean μ (left), resolution σ (middle) of the Gaussian as well as the decay term λ (right) of the exponential.

The resolution of other L1 energy sum quantities, H_T , Z_T and $\sum E_T$ parameterised as in Equation (3.4), can be found in Appendix (B.3). The same behaviour observed for the single jet triggers is also found for these quantities, where in the presence of higher pile-up the μ values are shifted to higher values, with a worsening resolution, σ again due to the increase in soft pile-up jets and the absence of pile-up subtraction at L1.

3.4.6. Summary

The performance of the CMS Level-1 Trigger has been studied and evaluated for jets and energy sum quantities using data collected during the 2012 LHC 8TeV run. These studies include the effect of introduction of a 5 GeV jet seed threshold into the jet algorithm

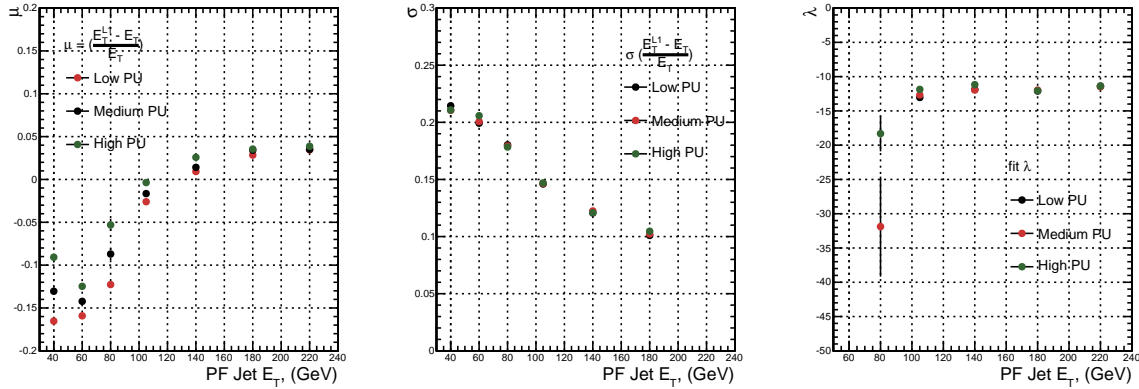


Figure 3.17.: Fit values from an **EMG** function fitted to the resolution plots of leading PF jet E_T measured as a function of $\frac{(L1 E_T - \text{Offline } E_T)}{\text{Offline } E_T}$ for low and medium pile-up conditions. The plots show the mean μ (left), resolution σ (middle) of the Gaussian as well as the decay term λ (right) of the exponential.

1145 configuration, the purpose of which is to mitigate the effects of pile-up on the rate of
 1146 L1 triggers whilst not adversely affecting the efficiency of these triggers. No significant
 1147 change in performance is observed with this change and good performance is observed
 1148 for a range of L1 quantities.

Chapter 4.

¹¹⁴⁹ SUSY searches in Hadronic Final ¹¹⁵⁰ States

¹¹⁵¹ In this chapter a model independent search for **SUSY** in hadronic final states with \cancel{E}_T
¹¹⁵² using the α_T variable and b-quark multiplicity is introduced and described in detail. The
¹¹⁵³ results presented are based on a data sample of pp collisions collected in 2012 at $\sqrt{s} = 8$
¹¹⁵⁴ TeV, corresponding to an integrate luminosity of $11.7 \pm 0.5 \text{ fb}^{-1}$.

¹¹⁵⁵ The kinematic variable α_T is motivated as a variable to provide strong rejections
¹¹⁵⁶ of QCD backgrounds, whilst maintaining sensitivity to possible a **SUSY** signal within
¹¹⁵⁷ Section (4.1). The search and trigger strategy in addition to the event reconstruction
¹¹⁵⁸ and selection are outlined within Sections (4.2-4.3).

¹¹⁵⁹ The method in which the **SM** background is estimated using an analytical technique
¹¹⁶⁰ to improve statistical precision at higher b-tag multiplicities is detailed within Section
¹¹⁶¹ (4.5), with a discussion on the impact of b-tagging and mis-tagging scale factors between
¹¹⁶² data and MC on any background predictions.

¹¹⁶³ A description of the formulation of appropriate systematic uncertainties applied to
¹¹⁶⁴ the background predictions to account for theoretical uncertainties and limitations in the
¹¹⁶⁵ simulation modelling of event kinematics and instrumental effects is covered in Section
¹¹⁶⁶ (4.6).

¹¹⁶⁷ Finally the statistical likelihood model to interpret the observations in the signal and
¹¹⁶⁸ control samples is described in Section (4.7). The experimental reach of the analysis
¹¹⁶⁹ discussed within this thesis is interpreted in two classes of **SMS** models, the topologies
¹¹⁷⁰ of which are detailed in Section (2.4.1). The **SMS** models considered in this analysis

1171 are summarised in Table 4.1. For each model, the **LSP** is assumed to be the lightest
1172 neutralino.

1173 Within the table are also defined reference points, parameterised in terms of parent
1174 gluino/squark and **LSP** sparticle masses, m_{parent} and m_{LSP} , respectively, which are used
1175 within the following chapters to demonstrate potential yields within the signal region
1176 of the search. The masses are chosen to reflect parameter space which is within the
1177 expected sensitivity reach of the search.

Model	Production/decay mode	Reference model	
		m_{parent}	m_{LSP}
G1 (T1)	$pp \rightarrow \tilde{g}\tilde{g}^* \rightarrow q\bar{q}\tilde{\chi}_1^0 q\bar{q}\tilde{\chi}_1^0$	700	300
G2 (T1bb)	$pp \rightarrow \tilde{g}\tilde{g}^* \rightarrow b\bar{b}\tilde{\chi}_1^0 b\bar{b}\tilde{\chi}_1^0$	900	500
G3 (T1tt)	$pp \rightarrow \tilde{g}\tilde{g}^* \rightarrow t\bar{t}\tilde{\chi}_1^0 t\bar{t}\tilde{\chi}_1^0$	850	250
D1 (T2)	$pp \rightarrow \tilde{q}\tilde{q}^* \rightarrow q\tilde{\chi}_1^0 \bar{q}\tilde{\chi}_1^0$	600	250
D2 (T2bb)	$pp \rightarrow \tilde{b}\tilde{b}^* \rightarrow b\tilde{\chi}_1^0 \bar{b}\tilde{\chi}_1^0$	500	150
D3 (T2tt)	$pp \rightarrow \tilde{t}\tilde{t}^* \rightarrow t\tilde{\chi}_1^0 \bar{t}\tilde{\chi}_1^0$	400	0

Table 4.1.: A summary of the **SMS** models interpreted in this analysis, involving both direct (D) and gluino-induced (G) production of squarks and their decays. Reference models are also defined in terms of parent and **LSP** sparticle mass

1178 4.1. An introduction to the α_T search

1179 The experimental signature of **SUSY** signal in the hadronic channel would manifest as a
1180 final state containing energetic jets and \cancel{E}_T . The search focuses on topologies where new
1181 heavy supersymmetric, R-parity conserving particles are pair-produced in pp collisions.
1182 These particles decaying to a **LSP** escape the detector undetected, leading to significant
1183 missing energy and missing hadronic transverse energy,

$$\mathcal{H}_T = \left| \sum_{i=1}^n p_T^{jet_i} \right|, \quad (4.1)$$

1184 defined as the vector sum of the transverse energies of jets selected in an event.
1185 Energetic jets produced in the decay of these supersymmetric particles also can produce
1186 significant visible transverse energy,

$$H_T = \sum_{i=1}^n E_T^{jet_i}, \quad (4.2)$$

1187 defined as the scalar sum of the transverse energies of jets selected in an event.

1188 A search within this channel is greatly complicated in a hadron collider environment,
1189 where the overwhelming background comes from inherently balanced multi-jet (“QCD”)
1190 events which are produced with an extremely large cross section as demonstrated within
1191 Figure 4.1. \cancel{E}_T can appear in such events with a substantial mis-measurement of jet
1192 energy or missed objects due to detector miscalibration or noise effects.

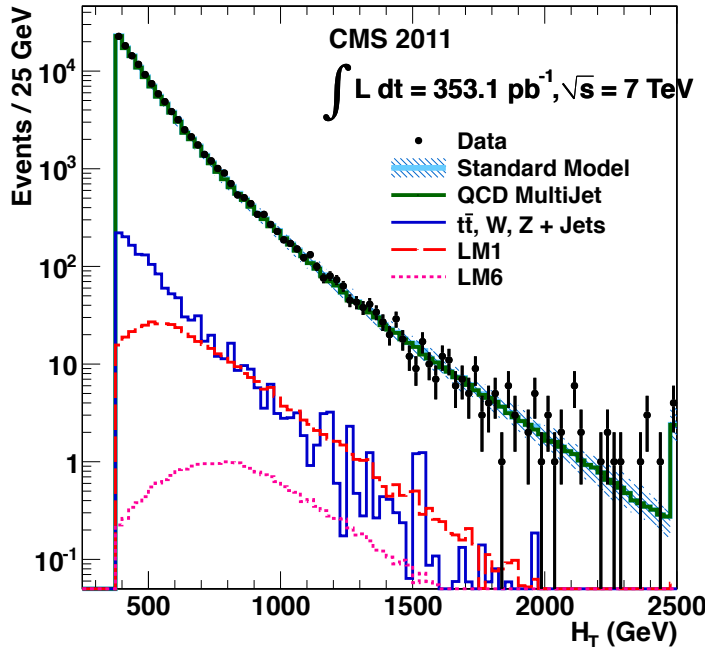


Figure 4.1.: Reconstructed offline H_T for 11.7fb^{-1} of data after a basic pre-selection. Sample is collected from prescaled H_T triggers. Overlaid are expectations from MC simulation of EWK processes as well as a reference signal model (labelled D2 from Table.4.1).

1193 Additional SM background from EWK processes with genuine \cancel{E}_T from escaping
1194 neutrinos comprise the irreducible background within this search and come mainly from:

- 1195 • $Z \rightarrow \nu\bar{\nu} + \text{jets}$,

- 1196 • $W \rightarrow l\nu + \text{jets}$ in which a lepton falls outside of detector acceptance, or the lepton
- 1197 decays hadronically $\tau \rightarrow \text{had}$,
- 1198 • $t\bar{t}$ with at least one leptonic W decay,
- 1199 • small background contributions from DY, single top and Diboson (WW,ZZ,WZ)
- 1200 processes.

1201 The search is designed to have a strong separation between events with genuine and
1202 “fake” \cancel{E}_T which is achieved primarily through the dimensionless kinematic variable, α_T
1203 [71][72].

1204 4.1.1. The α_T variable

1205 For a perfectly measured di-jet QCD event, conservation laws dictate that they must be
1206 produced back-to-back and of equal magnitude. However in di-jet events with real \cancel{E}_T ,
 both of these jets are produced independently of one another, depicted in Figure 4.2.

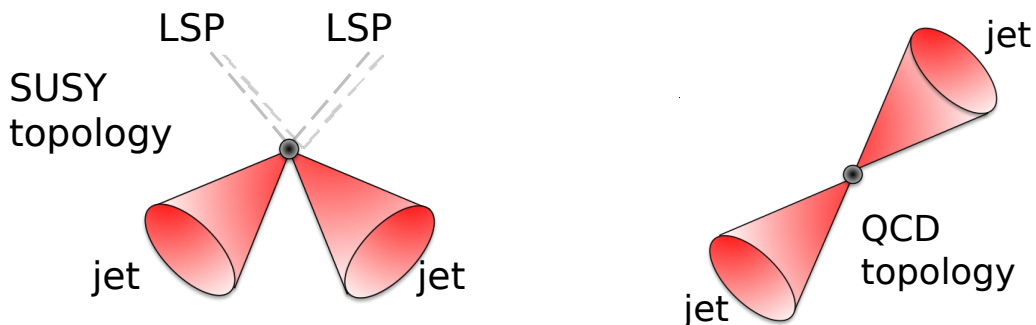


Figure 4.2.: The event topologies of background QCD di-jet events (right) and a generic SUSY signature with genuine \cancel{E}_T (left).

1207

1208 Exploiting this feature leads to the formulation of α_T in di-jet systems defined as,

$$\alpha_T = \frac{E_T^{j2}}{M_T}, \quad (4.3)$$

1209 where E_T^{j2} is the transverse energy of the least energetic of the two jets and M_T
1210 defined as:

$$M_T = \sqrt{\left(\sum_{i=1}^2 E_T^{j_i}\right)^2 - \left(\sum_{i=1}^2 p_x^{j_i}\right)^2 - \left(\sum_{i=1}^2 p_y^{j_i}\right)^2} \equiv \sqrt{H_T^2 - \cancel{H}_T^2}. \quad (4.4)$$

1211 A perfectly balanced di-jet event i.e. $E_T^{j_1} = E_T^{j_2}$ would give an $\alpha_T = 0.5$, where as
 1212 events with jets which are not back-to-back, for example in events in which a W or Z
 1213 recoils off a system of jets, α_T can achieve values in excess of 0.5.

1214 α_T can be extended to apply to any arbitrary number of jets, undertaken by modelling
 1215 a system of n jets as a di-jet system, through the formation of two pseudo-jets [73].
 1216 The two pseudo-jets are built by merging the jets present in the event such that the 2
 1217 pseudo-jets are chosen to be as balanced as possible, i.e the $\Delta H_T \equiv |E_T^{pj_1} - E_T^{pj_2}|$ is
 1218 minimised between the two pseudo jets. Using Equation (4.4), α_T can be rewritten as,

$$\alpha_T = \frac{1}{2} \frac{H_T - \Delta H_T}{\sqrt{H_T^2 - \cancel{H}_T^2}} = \frac{1}{2} \frac{1 - \Delta H_T/H_T}{\sqrt{1 - (\cancel{H}_T/H_T)^2}}. \quad (4.5)$$

1219 The distribution of α_T for the two jet categories used within this analysis, 2,3 and
 1220 ≥ 4 jets, is shown in the Figure 4.3, demonstrating the ability of the α_T variable to
 1221 discriminate between multi jet events and EWK processes with genuine \cancel{E}_T in the final
 1222 state.

1223 The α_T requirement used within the search is chosen to be $\alpha_T > 0.55$ to ensure
 1224 that the QCD multijet background is negligible even in the presence of moderate jet
 1225 mis-measurement. There still remains other effects which can cause multijet events to
 1226 artificially have a large α_T value, which are discussed in detail in Section (4.2.2).

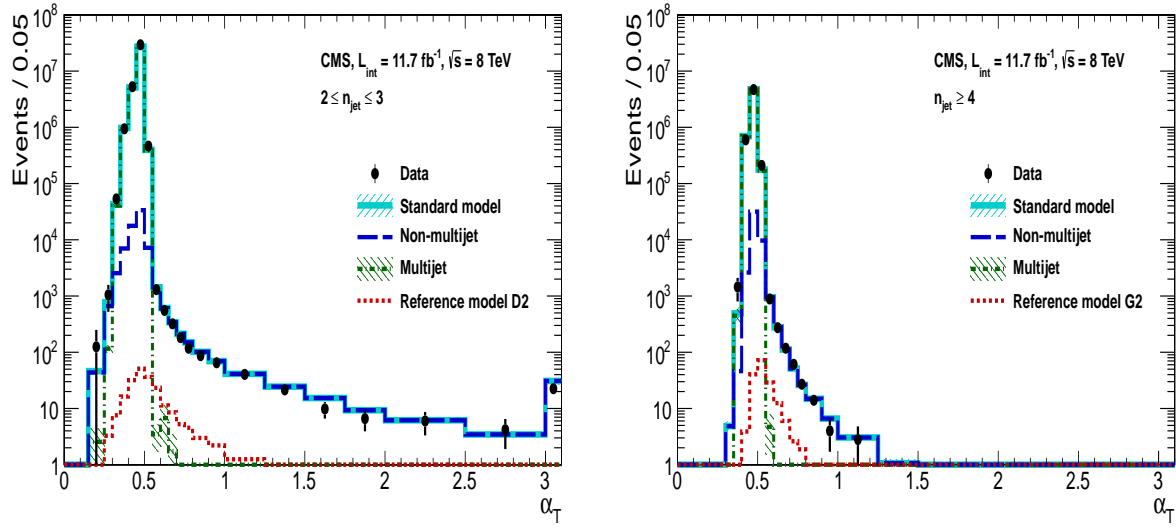


Figure 4.3.: The α_T distributions for the low 2-3 (left) and high ≥ 4 (right) jet multiplicities after a full analysis selection and shown for $H_T > 375$. Data is collected using both prescaled H_T triggers and dedicated α_T triggers for below and above $\alpha_T = 0.55$ respectively. . Expected yields as given by simulation are also shown for multijet events (green dash-dotted line), EWK backgrounds with genuine \cancel{E}_T (blue long-dashed line), the sum of all SM processes (cyan solid line) and the reference signal model D2 (left, red dotted line) or G2 (right, red dotted line).

1227 4.2. Search Strategy

1228 The aim of the analysis presented in this thesis is to identify an excess of events in data
 1229 over the SM background expectation in multi-jet final states and significant \cancel{E}_T . The
 1230 essential suppression of the dominant QCD background for such a search is addressed by
 1231 the α_T variable described in the previous section. For estimation of the remaining EWK
 1232 backgrounds, three independent data control samples are used to predict the different
 1233 processes that compose the background :

- 1234 • $\mu + \text{jets}$ to determine $W + \text{jets}$, $t\bar{t}$ and single top backgrounds,
- 1235 • $\gamma + \text{jets}$ to determine the irreducible $Z \rightarrow \nu\bar{\nu} + \text{jets}$ background,
- 1236 • $\mu\mu + \text{jets}$ to determine the irreducible $Z \rightarrow \nu\bar{\nu} + \text{jets}$ background.

1237 These control samples are chosen to both be rich in specific EWK processes, be free of
 1238 QCD multi-jet events and to also be kinematically similar to the hadronic signal region
 1239 that they are estimating the backgrounds of, see Section (4.2.3).

1240 To remain inclusive to a large range of possible **SUSY** models, the signal region is
1241 binned in the following categories to allow for increased sensitivity in the interpretation
1242 of results for different **SUSY** topologies:

1243 **Sensitivity to a range of SUSY mass splittings**

1244 The hadronic signal region is defined by $H_T > 275$, divided into eight bins in H_T .

- 1245 – Two bins of width 50 GeV in the range $275 < H_T < 375$ GeV,
1246 – five bins of width 100 GeV in the range $375 < H_T < 875$ GeV,
1247 – and a final open bin, $H_T > 875$ GeV.

1248 The choice at low H_T is driven primarily by trigger constraints. The mass difference
1249 between the **LSP** and the particle that it decays from is an important factor in the
1250 amount of hadronic activity in the event.

1251 A large mass splitting will lead to hard high p_T jets which contribute to the H_T
1252 sum. From Figure 4.1 it can be seen that the **SM** background falls sharply at high
1253 H_T values, therefore a large number of H_T bins will lead to easier identification
1254 of such signals. Conversely smaller mass splittings lead to softer jet p_T 's which will
1255 subsequently fall into the lower H_T range.

1256 **Sensitivity to production method of SUSY particles**

1257 The production mechanism of any potential **SUSY** signal can lead to different event
1258 topologies. One such way to discriminate between gluino ($g\tilde{g}$ - “high multiplicity”),
1259 and direct squark ($q\tilde{q}$ - “low multiplicity”) induced production of **SUSY** particles is
1260 realised through the number of reconstructed jets in the final state.

1261 The analysis is thus split into two jet categories : 2-3 jets , ≥ 4 jets to give sensitivity
1262 to both of these mechanisms.

1263 **Sensitivity to “Natural SUSY” via tagging jets from b-quarks**

1264 Jets originating from bottom quarks (b-jets) are identified through vertices that
1265 are displaced with respect to the primary interaction. The algorithm used to tag
1266 b-jets is the Combined Secondary Vertex Medium Working Point (**CSV**) tagger,
1267 described within Section (3.3.2). A cut is placed on the discriminator variable of
1268 > 0.679 , leading to a gluon/light-quark mis-tag rate of 1% and a jet p_T dependant
1269 b-tagging efficiency of 60-70% [64].

1270 Natural **SUSY** models would be characterised through final-state signatures rich
 1271 in bottom quarks. A search relying on methods to identify jets originating from
 1272 bottom quarks through b-tagging, will significantly improve the sensitivity to this
 1273 class of signature.

1274 This is achieved via the binning of events in the signal region according to the
 1275 number of b-tagged jets reconstructed in each event, in the following: 0,1,2,3, ≥ 4
 1276 b-tag categories . In the highest ≥ 4 b-tag category due to a limited number of
 1277 expected signal and background, just three H_T bins are employed: 275-325 GeV,
 1278 325-375 GeV, ≥ 375 GeV.

1279 This characterisation is identically mirrored in all control samples, with the infor-
 1280 mation from all samples and b-tag categories used simultaneously in the likelihood
 1281 model, see Section (4.7), in order to interpret the results in a coherent and powerful
 1282 way.

1283 The combination of the H_T , jet multiplicity and b-tag categorisation of the signal
 1284 region as described above, resultantly leads to 67 different bins in which the analysis is
 1285 interpreted in, which is depicted in Figure 4.4.

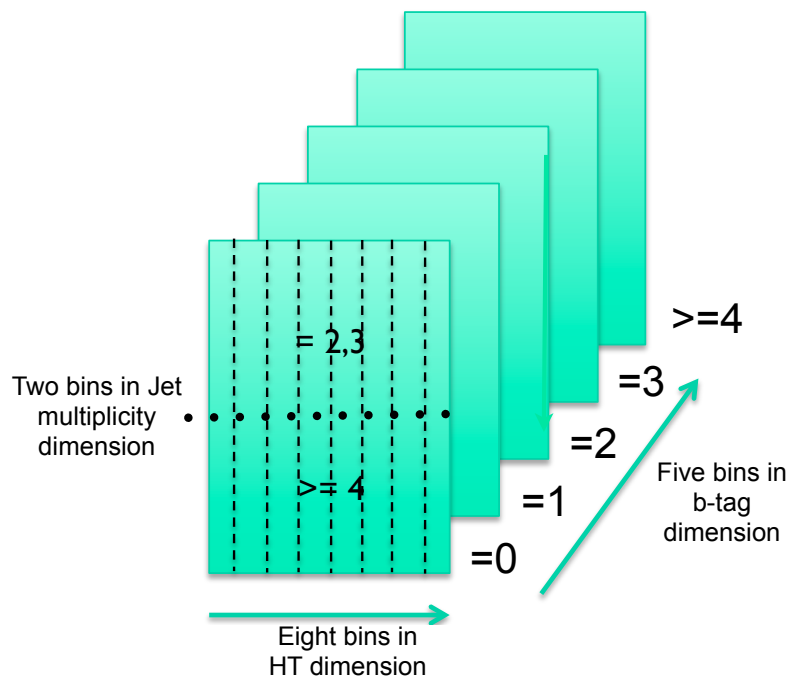


Figure 4.4.: Pictorial depiction of the analysis strategy employed by the α_T search to increase sensitivity to a wide spectra of **SUSY** models.

1286 **4.2.1. Physics Objects**

1287 The physics objects used in the analysis defined below, follow the recommendation of
1288 the various CMS Physics Object Groups ([POGs](#)).

1289 **• Jets**

1290 The jets used in this analysis are CaloJets, reconstructed as described in Section
1291 ([3.3.1](#)) using the anti- k_T jet clustering algorithm.

1292 To ensure the jet object falls within the calorimeter systems a pseudo-rapidity
1293 requirement of $|\eta| < 3$ is applied. Each jet must pass a “loose” identification criteria
1294 to reject jets resulting from unphysical energy, the criteria of which are detailed in
1295 Table A.1 of Appendix A [[74](#)].

1296 **• Muons**

1297 Muons are selected in the $\mu + \text{jets}$ and $\mu\mu + \text{jets}$ control samples, and vetoed in
1298 the signal region. The same cut based identification criteria is applied to muons in
1299 both search regions and is summarised in Table 4.2 [[75](#)].

Categories	Criteria
Global Muon	True
PFMuon	True
χ^2	< 10
Muon chamber hits	> 0
Muon station hits	> 1
Transvere impact d_{xy}	< 0.2mm
Longitudinal distance d_z	< 0.5mm
Pixel hits	> 0
Track layer hits	> 5
PF Isolation (DeltaB corrected)	<0.12

Table 4.2.: Muon Identification criteria used within the analysis for selection/veto purposes in the muon control/signal selections.

1300 Additionally muons are required to be within the acceptance of the muon tracking
1301 systems. For the muon control samples, trigger requirements necessitate a $|\eta| <$
1302 2.1 for the selection of muons. In the signal region where muons are vetoed these

1303 conditions are relaxed to $|\eta| < 2.5$ and a minimum threshold of $p_T > 10$ GeV is
1304 required of muon objects.

1305 • **Photons**

1306 Photons are selected within the $\gamma +$ jets control sample and vetoed in all other
1307 selections. Photons are identified in both cases according to the cut based criteria
1308 listed in Table 4.3 [76].

Variable	Definition
$H/E < 0.05$	The ratio of hadronic energy in the HCAL tower directly behind the ECAL super-cluster and the ECAL super-cluster itself.
$\sigma_{i\eta i\eta} < 0.011$	The log energy weighted width (σ), of the extent of the shower in the η dimension.
$R9 < 1.0$	The ratio of the energy of the 3×3 crystal core of the super-cluster compared to the total energy stored in the 5×5 super-cluster.
Combined Isolation < 6 GeV	The photons are required to be isolated with no electromagnetic or hadronic activity within a radius $\Delta R = 0.3$ of the photon object. A combination of the pileup subtracted [77], ECAL , HCAL and tracking isolation sums are used to determine the combined total isolation value.

Table 4.3.: Photon Identification criteria used within the analysis for selection/veto purposes in the $\gamma +$ jets control/signal selections.

1309 Photon objects are also required to have a minimum momentum of $p_T > 25$ GeV.

1310 • **Electrons**

1311 Electron identification is defined for veto purposes. They are selected according to
1312 the following cut-based criteria listed in Table 4.4, utilising PF-based isolation.

1313 Electrons are required to be identified at $|\eta| < 2.5$, with a minimum $p_T > 10$ GeV
1314 threshold to ensure that the electron falls within the tracking system of the detector.

1315 • **Noise and E_T Filters**

1316 A series of Noise filters are applied to veto events which contain spurious non-physical
1317 jets that are not picked up by the jet id, and events which give large unphysical E_T
1318 values. These filters are listed within Table A.3 of Appendix A.

Categories	Barrel	EndCap
$\Delta\eta_{In}$	0.007	0.009
$\Delta\phi_{In}$	0.15	0.10
$\sigma_{in\eta}$	0.01	0.03
H/E	0.12	0.10
d0 (vtx)	0.02	0.02
dZ (vtx)	0.20	0.20
$ (1/E_{ECAL} - 1/p_{track}) $	0.05	0.05
PF Combined isolation/ p_T	0.15	0.15
Vertex fit probability	10^{-6}	10^{-6}

Table 4.4.: Electron Identification criteria used within the analysis for veto purposes.

1319 4.2.2. Event Selection

1320 The selection criteria for events within the analysis are detailed below. A set of common
1321 cuts are applied to both signal (maximise acceptance to a range of **SUSY** signatures), and
1322 control samples (retain similar jet kinematics for background predictions), with additional
1323 selection cuts applied to each control sample to enrich the sample in a particular **EWK**
1324 processes, see Section (4.2.3).

1325 The jets considered in the analysis are required to have a transverse momentum $p_T >$
1326 50 GeV, with a minimum of two jets required in the event. The highest E_T jet is required
1327 to lie within the central tracker acceptance $|\eta| < 2.5$, and the two leading p_T jets must
1328 each have $p_T > 100$ GeV. Any event which has a jet with $p_T > 50$ GeV that either fails
1329 the “loose” identification criteria described in Section(4.2.1) or has $|\eta| > 3.0$, is rejected.
1330 Similarly events in which an electron, muon or photon fails object identification but pass
1331 η and p_T restrictions are identified as an “odd” lepton/photon and the event is vetoed.

1332 At low H_T , the jet threshold requirements applied to be considered as part of the
1333 analysis and enter the H_T sum are scaled downwards. These are scaled down in order to
1334 not restrict phase space, preserving jet multiplicities and background admixture in the
1335 lower H_T bins, as listed in Table 4.5.

1336 Within the signal region to suppress **SM** processes with genuine E_T' from neutrinos,
1337 events containing isolated electrons or muons are vetoed. Furthermore to ensure a pure
1338 multi-jet topology, events are vetoed if an isolated photon is found with $p_T > 25$ GeV.

H_T bin	minimum jet p_T	second leading jet p_T
$275 < H_T < 325$	36.7	73.3
$325 < H_T < 375$	43.3	86.6
$375 < H_T$	50.0	100.0

Table 4.5.: Jet thresholds used in the three H_T regions of the analysis.

1339 An α_T requirement of > 0.55 is required to reduce the QCD multi-jet background
 1340 to a negligible amount. Finally additional cleaning cuts are applied to protect against
 1341 pathological deficiencies such as reconstruction failures or severe energy mis-measurements
 1342 due to detector inefficiencies:

- Significant \cancel{H}_T can arise in events with no real \cancel{E}_T due to multiple jets falling below the p_T threshold used for selecting jets. This in turn leads to events which can then incorrectly pass the α_T requirements of the analysis. This effect can be negated by requiring that the missing transverse momentum reconstructed from jets alone does not greatly exceed the missing transverse momentum reconstructed from all of the detector's calorimeter towers,

$$R_{miss} = \cancel{H}_T / \cancel{E}_T < 1.25.$$

1343 • Fake \cancel{E}_T and \cancel{H}_T can arise due to significant jet mis-measurements caused by a small
 1344 number of non-functioning **ECAL** regions. These regions absorb electromagnetic
 1345 showers which are subsequently not added to the jet energy sum. To circumvent
 1346 this problem the following procedure is employed : For each jet in the event, the
 1347 angular separation

$$\Delta\phi_j^* \equiv \Delta\phi(p_j^\rightarrow - \sum_{i \neq j} p_i^\rightarrow), \quad (4.6)$$

1348 is calculated where that jet is itself removed from the event. Here $\Delta\phi^*$ is a measure
 1349 of how aligned the \cancel{H}_T of an event is with a jet, a small value is compatible with the
 1350 hypothesis of an inherently balanced event in which a jet has been mis-measured.
 1351 For every jet in an event with $\Delta\phi^* < 0.5$, if the ΔR distance between the selected jet
 1352 and the closest dead **ECAL** region is also < 0.3 , then the event is rejected. Similarly

1353 events are rejected if the jet points within $\Delta R < 0.3$ of the **ECAL** barrel-endcap
1354 gap at $|\eta| = 1.5$.

1355 Some of the key distributions of the data used in this analysis compared to MC
1356 simulation are shown in Figure 4.5. The MC samples are normalised to a luminosity of
1357 11.7 fb^{-1} , with no requirement placed upon the number of b-tagged jets or number of
1358 jets in the events.

1359 The distributions shown are presented for purely illustrative purposes, with the MC
1360 simulation itself not used in absolute term to estimate the yields from background
1361 processes, see Sections (4.2.3,4.5). However it is nevertheless important to demonstrate
1362 that good agreement exists between simulation and observation in data.

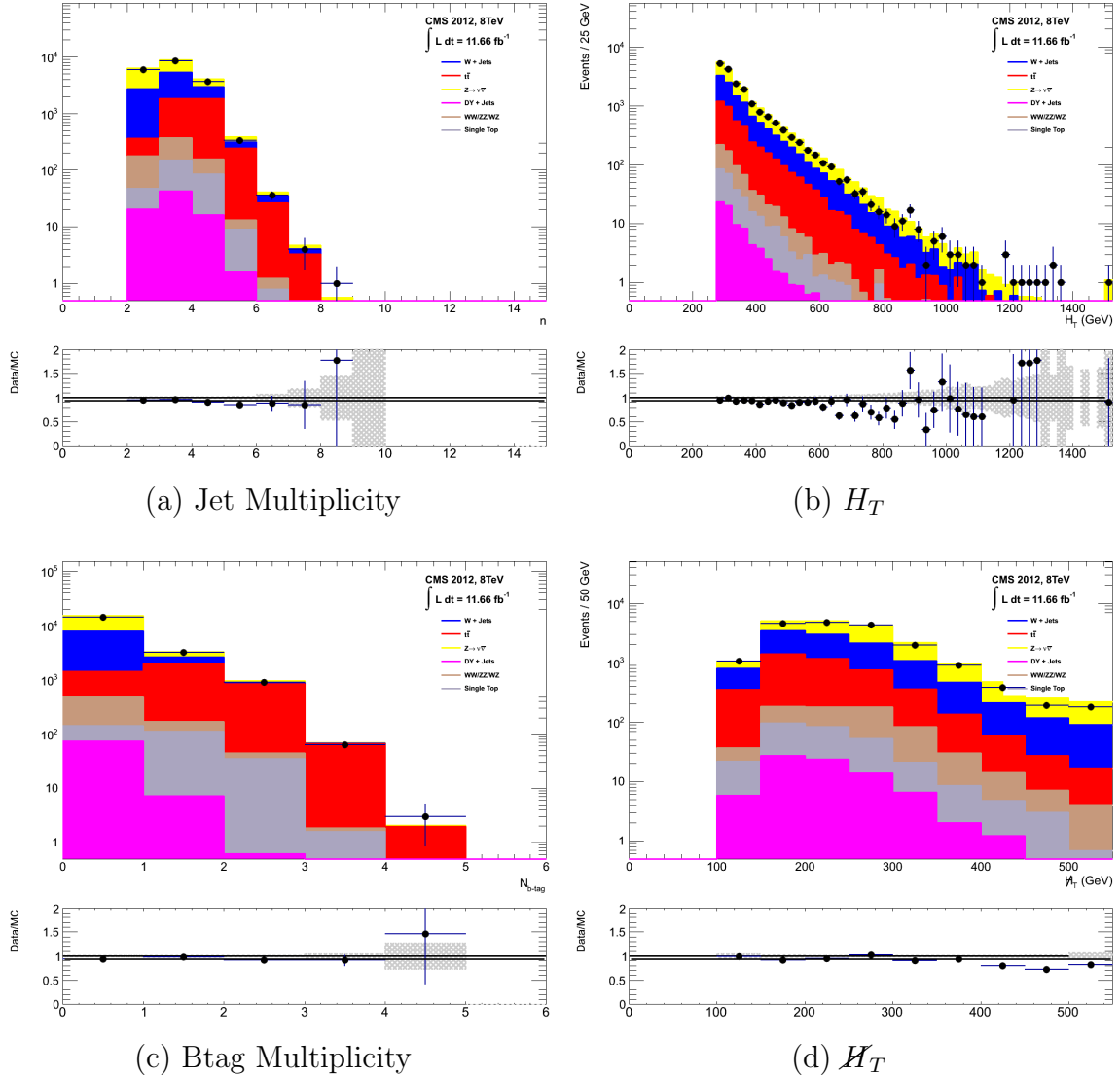


Figure 4.5.: Data/MC comparisons of key variables for the hadronic signal region, following the application of the hadronic selection criteria and the requirements of $H_T > 275$ GeV and $\alpha_T > 0.55$. Bands represent the uncertainties due to the statistical size of the MC samples. No requirement is made upon the number of b-tagged jets or jet multiplicity in these distributions.

4.2.3. Control Sample Definition and Background Estimation

The method used to estimate the background contributions in the hadronic signal region relies on the use of a Transfer Factor (TF). This is determined from MC simulation in both the control, N_{MC}^{control} , and signal, N_{MC}^{signal} , region to transform the observed yield measured in data for a control sample, $N_{\text{obs}}^{\text{control}}$, into a background prediction, $N_{\text{pred}}^{\text{signal}}$, via Equation (4.7),

$$N_{\text{pred}}^{\text{signal}} = \frac{N_{\text{MC}}^{\text{signal}}}{N_{\text{MC}}^{\text{control}}} \times N_{\text{obs}}^{\text{control}}. \quad (4.7)$$

1370 All MC samples are normalised to the luminosity of the data samples, 11.7 fb^{-1} .
 1371 Through this method, “vanilla” predictions for the **SM** background in the signal region
 1372 can be made by considering separately the sum of the prediction from either the $\mu + \text{jets}$
 1373 and $\gamma + \text{jets}$ or $\mu + \text{jets}$ and $\mu\mu + \text{jets}$ samples. However the final background estimation
 1374 from which results are interpreted, is calculated via a fitting procedure defined formally
 1375 by the likelihood model described in Section (4.7).

1376 The sum of the expected yields from all MC processes, in each control sample enter
 1377 the denominator, $N_{\text{MC}}^{\text{control}}$, of the **TF** defined in Eq (4.7). However for the numerator
 1378 , $N_{\text{MC}}^{\text{signal}}$, only the relevant processes that the control sample is used in estimating a
 1379 background for, enter into the **TF**.

1380 For the $\mu + \text{jets}$ sample the simulated MC processes which enter the numerator of
 1381 the **TF** are,

$$N_{\text{MC}}^{\text{signal}}(H_T, n_{\text{jet}}) = N_W + N_{t\bar{t}} + N_{DY} + N_t + N_{di-boson}, \quad (4.8)$$

1382 whilst for both the $\mu\mu + \text{jets}$ and $\gamma + \text{jets}$ samples the only MC process used in the
 1383 numerator is,

$$N_{\text{MC}}^{\text{signal}}(H_T, n_{\text{jet}}) = N_{Z \rightarrow \nu\bar{\nu}}. \quad (4.9)$$

1384 The control samples and the **EWK** processes they are specifically tuned to select
 1385 are defined below, with distributions of key variables for each of the control samples
 1386 shown for illustrative purposes in Figures 4.6, 4.7 and 4.8. No requirement is placed
 1387 upon the number of b-tagged jets or jet multiplicity in the distributions shown. The
 1388 MC distributions highlight the background compositions of each control sample, where
 1389 in general, good agreement is observed between data and simulation, giving confidence

1390 that the samples are well understood. The contribution from QCD multi-jet events is
1391 expected to be negligible :

1392 **The $\mu +$ jets control sample**

1393 Events from $W +$ jets and $t\bar{t}$ processes enter into the hadronic signal sample due to
1394 unidentified leptons from acceptance or threshold effects and hadronic tau decays.
1395 These leptons originate from the decay of high p_T W bosons.

1396 The control samples specifically identifies $W \rightarrow \mu\bar{\nu}$ decays within the same phase-
1397 space of the signal region, where the muon is subsequently ignored in the calculation
1398 of event level variables, i.e. H_T , \mathcal{H}_T , α_T . All kinematic jet-based cuts are identical
1399 to those applied in the hadronic search region detailed in Section (4.2.2), with the
1400 same H_T , jet multiplicity and b-jet multiplicity binning described above.

- 1401 – Muons originating from W boson decays are selected by requiring one tightly
1402 isolated muon defined in Table 4.2, with a $p_T > 30$ GeV and $|\eta| < 2.1$. Both of
1403 these threshold arise from trigger restrictions.
- 1404 – The transverse mass of the W candidate must satisfy $M_T(\mu, \cancel{E}_T) < 30$ GeV (to
1405 suppress QCD multi-jet events).
- 1406 – Events which contain a jet overlapping with a muon $\Delta R(\mu, \text{jet}) < 0.5$ are vetoed
1407 to remove events from muons produced as part of a jet’s hadronisation process.
- 1408 – Events containing a second muon candidate which has failed id, but passed p_T
1409 and $|\eta|$ requirements, are checked to have an invariant mass that satisfies $m_Z - 25 < M_{\mu_1\mu_2} > m_Z + 25$, thus removing $Z \rightarrow \mu\mu$ contamination.

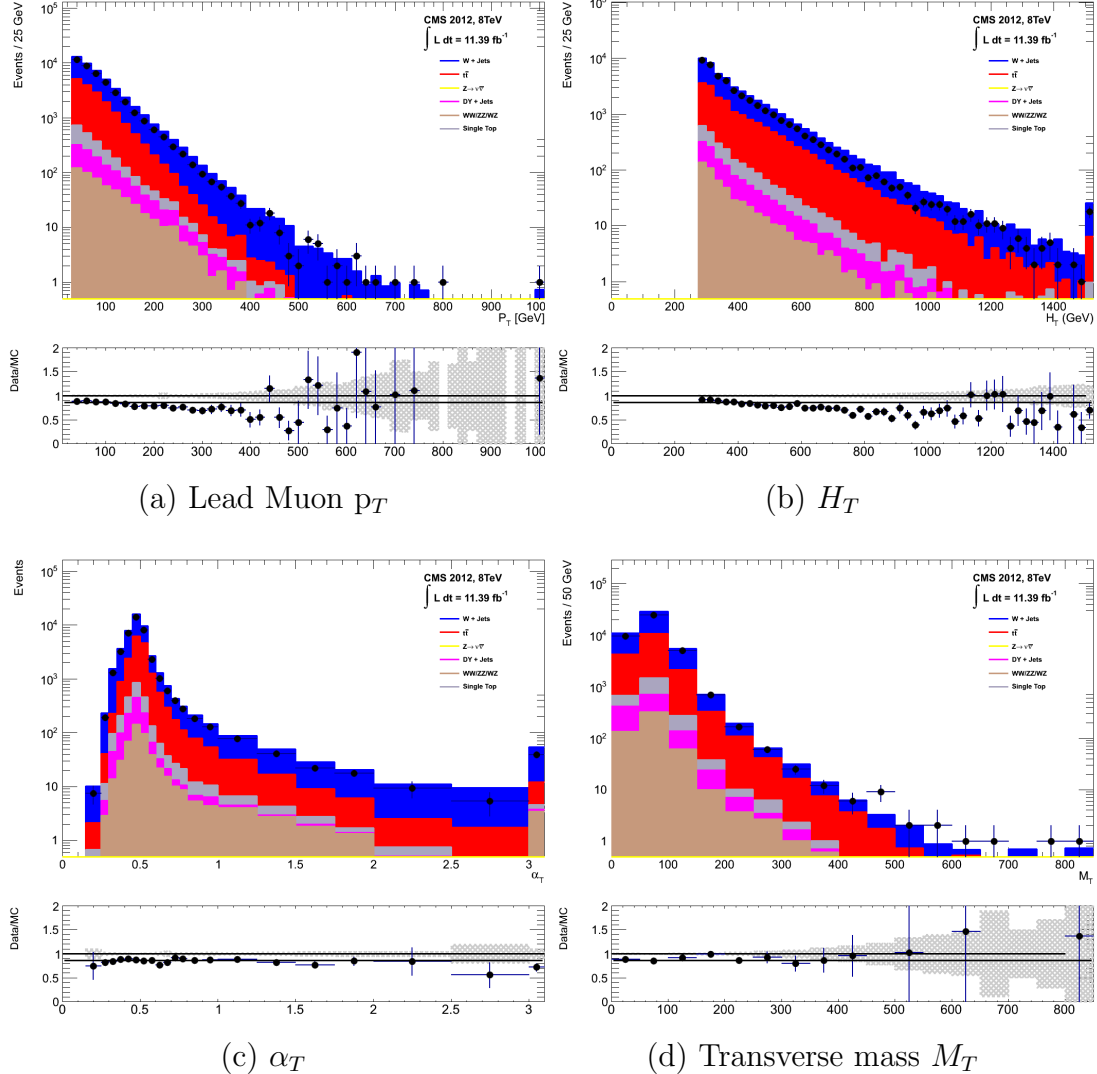


Figure 4.6.: Data/MC comparisons of key variables for the $\mu + \text{jets}$ selection, following the application of selection criteria and the requirements that $H_T > 275$ GeV. Bands represent the uncertainties due to the statistical size of the MC samples. No requirement is made upon the number of b-tagged jets or jet multiplicity in these distributions.

The $\mu\mu + \text{jets}$ control sample

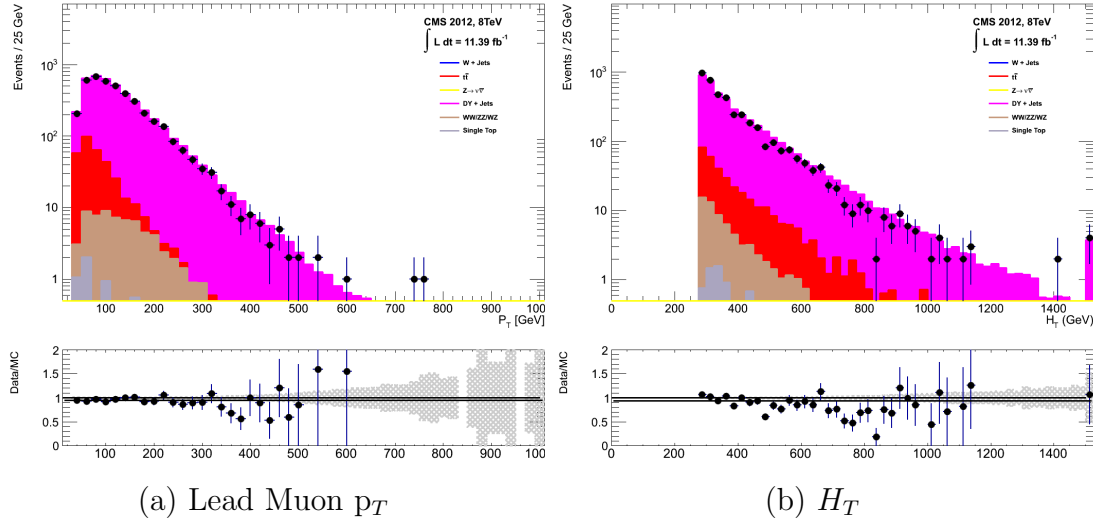
The $Z \rightarrow \nu\bar{\nu} + \text{jets}$ background enters into the signal region from genuine E_T from the escaping neutrinos. This background is estimated using two control samples, the first of which is the $Z \rightarrow \mu\bar{\mu} + \text{jets}$ process, which posses identical kinematic properties, but with different acceptance and branching ratio [1].

The same acceptance requirements as the $\mu + \text{jets}$ selection for muons is applied, as defined in Table 4.2. Muons in the event are ignored for the purpose of the

calculation of event level variables. Kinematic jet-based cuts and phase space binning identical to the hadronic search region are also applied.

- Muons origination from a Z boson decay are selected requiring exactly two tightly isolated muons. Due to trigger requirements the leading muon is required to have $p_T > 30$ GeV and $|\eta| < 2.1$. The requirement of the p_T on the second muon is relaxed to 10 GeV.
- Events are vetoed if containing a jet overlapping with a muon $\Delta R(\mu, \text{jet}) < 0.5$.
- In order to specifically select two muons both originating from a single Z boson decay, the invariant mass of the two muons must satisfy $m_Z - 25 > M_{\mu_1\mu_2} < m_Z + 25$.

The $\mu\mu + \text{jets}$ sample is used to make predictions in the signal region in the two lowest H_T bins, providing coverage where the $\gamma + \text{jets}$ sample is unable to, due to trigger requirements. In higher H_T bins, the higher statistics of the $\gamma + \text{jets}$ sample is instead used to determine the $Z \rightarrow \nu\bar{\nu}$ estimation.



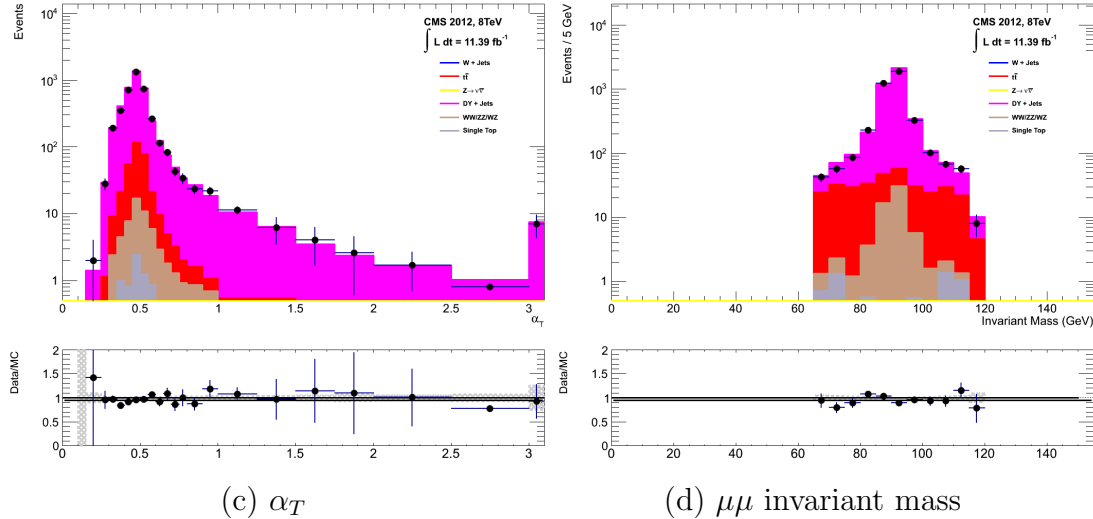


Figure 4.7.: Data/MC comparisons of key variables for the $\mu\mu + \text{jets}$ selection, following the application of selection criteria and the requirements that $H_T > 275$ GeV. Bands represent the uncertainties due to the statistical size of the MC samples. No requirement is made upon the number of b-tagged jets or jet multiplicity in these distributions.

The $\gamma + \text{jets}$ control sample

The $Z \rightarrow \nu\bar{\nu} + \text{jets}$ background is also estimated from a $\gamma + \text{jets}$ control sample, which possesses a larger cross section and kinematic properties similar to those of $Z \rightarrow \mu\bar{\mu}$ events where the photon is ignored [78][79]. The photon is ignored for the purpose of the calculation of event level variables, and identical selection cuts to the hadronic signal region are applied.

- Exactly one photon is selected, satisfying identification criteria as detailed in Table 4.3, with a minimum $p_T > 165$ GeV to satisfy trigger thresholds and $|\eta| < 1.45$ to ensure the photon remains in the barrel of the detector.
- A selection criteria of $\Delta R(\gamma, \text{jet}) < 1.0$, between the photon and all jets is applied to ensure the acceptance of only well isolated $\gamma + \text{jets}$ events.
- Given that the photon is ignored, this control sample can only be applied in the H_T region > 375 GeV, due to the trigger thresholds on the minimum p_T of the photon, and the H_T requirement of an $\alpha_T > 0.55$ cut from Equation (4.5).

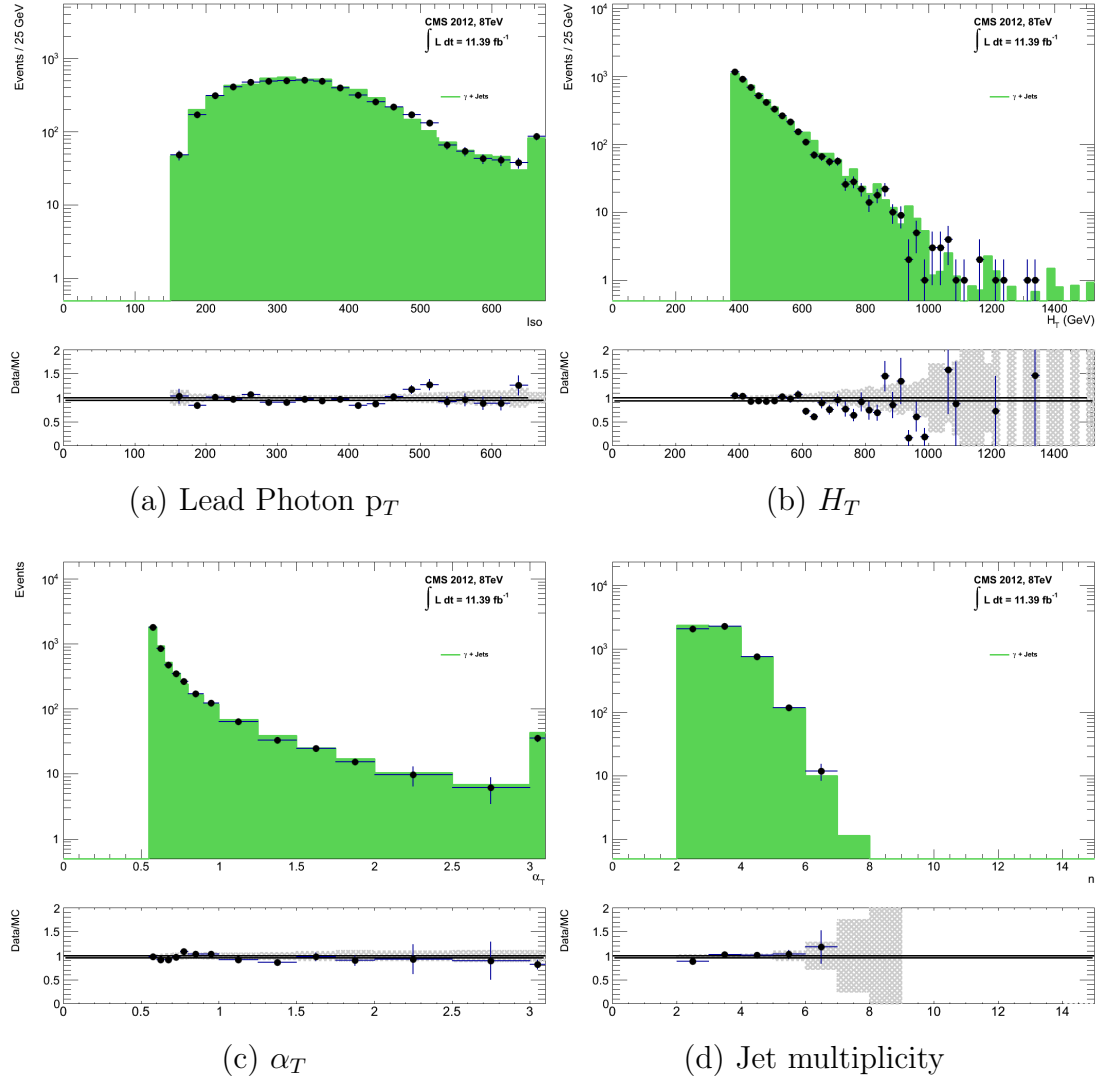


Figure 4.8.: Data/MC comparisons of key variables for the $\gamma + \text{jets}$ selection, following the application of selection criteria and the requirements that $H_T > 375 \text{ GeV}$ and $\alpha_T > 0.55$. Bands represent the uncertainties due to the statistical size of the MC samples. No requirement is made upon the number of b-tagged jets or jet multiplicity in these distributions.

The selection criteria of the three control samples are defined to ensure background composition and event kinematics mirror closely the signal region. This is done in order to minimise the reliance on MC simulation to model correctly the backgrounds and event kinematics in the control and signal samples.

However in the case of the $\mu + \text{jets}$ and $\mu\mu + \text{jets}$ samples, the α_T requirement is relaxed in the selection criteria of these samples. This is made possible as contamination from QCD multi-jet events is suppressed to a negligible level by the other kinematic selection criteria within the two control samples, to select pure EWK processes. Thus in

¹⁴⁵⁹ this way, the acceptance of the two muon control samples can be significantly increased,
¹⁴⁶⁰ which simultaneously improves their predictive power and further reduces the effect of
¹⁴⁶¹ any potential signal contamination.

¹⁴⁶² The modelling of the α_T variable is probed through a dedicated set of closure tests,
¹⁴⁶³ described in Section (4.6), which demonstrate that the different α_T acceptances for the
¹⁴⁶⁴ control and signal samples have no significant systematic bias on the prediction.

¹⁴⁶⁵ 4.2.4. Estimating the QCD Background Multi-jet Background

¹⁴⁶⁶ A negligible background from QCD multi-jet events within the hadronic signal region
¹⁴⁶⁷ is expected due to the selection requirement, and additional cleaning filters applied.
¹⁴⁶⁸ However a conservative approach is still adopted and the likelihood model, see Section
¹⁴⁶⁹ (??), is given the freedom to estimate any potential QCD multi-jet contamination.

¹⁴⁷⁰ Any potential contamination can be identified through the variable R_{α_T} , defined as
¹⁴⁷¹ the ratio of events above and below the α_T threshold value used in the analysis. This is
¹⁴⁷² modelled by a H_T dependant falling exponential function which takes the form,

$$R_{\alpha_T}(H_T) = A \exp^{-k_{QCD} H_T}, \quad (4.10)$$

¹⁴⁷³ where the parameters A and k_{QCD} are the normalisation and exponential decay
¹⁴⁷⁴ constants respectively.

¹⁴⁷⁵ For QCD event topologies this exponential behaviour is expected as a function of H_T
¹⁴⁷⁶ for several reasons. The improvement of jet energy resolution at higher H_T due to higher
¹⁴⁷⁷ p_T jets leads to a narrower peaked distribution, causing R_{α_T} to fall. Similarly at higher
¹⁴⁷⁸ H_T values > 375 GeV, the jet multiplicity rises slowly with H_T . As shown in Figure 4.3,
¹⁴⁷⁹ at higher jet multiplicities, the result of the combinatorics used in the determination of
¹⁴⁸⁰ α_T , also lead to a narrower α_T distribution.

¹⁴⁸¹ The value of the decay constant k_{QCD} is constrained via measurements within data
¹⁴⁸² sidebands to the signal region. This is also done to validate the falling exponential
¹⁴⁸³ assumption for QCD multi-jet topologies. The sidebands are enriched in QCD multi-jet
¹⁴⁸⁴ background and defined as regions where α_T is relaxed or that the R_{miss} cut is inverted.

1485 Figure 4.9 depicts the definition of these data sidebands used to constrain the value of
1486 k_{QCD} .

1487

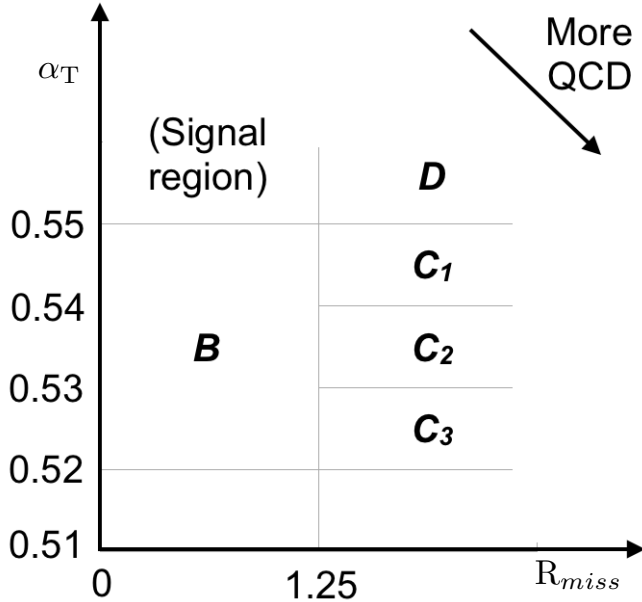


Figure 4.9.: QCD sideband regions, used for determination of k_{QCD} .

1488 The fits to determine the value of k_{QCD} are shown in Appendix (C.1), for which the best
1489 fit value obtained from sideband region B is determined to be $k_{QCD} = 2.96 \pm 0.64 \times 10^{-2}$
1490 GeV^{-1} .

1491 The best fit values of the remaining three C sideband regions are used to estimate
1492 the systematic uncertainty on the central value obtained from sideband region B. The
1493 variation of these measured values is used to determine the error on the determined
1494 central value, and is calculated to be $1.31 \pm 0.26 \times 10^{-2} \text{GeV}^{-1}$. This relative error of \sim
1495 20% gives an estimate of the systematic uncertainty of the measurement to be applied to
1496 k_{QCD} .

1497 Finally the same procedure is performed for sideband region D to establish that the
1498 value of k_{QCD} extracted from a lower α_T slice can be applied to the signal region $\alpha_T >$
1499 0.55. The likelihood fit is performed across all H_T bins within the QCD enriched region
1500 with no constraint applied to k_{QCD} . The resulting best fit value for k_{QCD} shows good
1501 agreement between that and the weighted mean determined from the three C sidebands
1502 regions. This demonstrates that the assumption of using the central value determined
1503 from sideband region B, to provide an unbiased estimator for k_{QCD} in the signal region
1504 ($\alpha_T > 0.55$) is valid.

1505 Table 4.6, summarises the best fit k_{QCD} values determined for each of the sideband
1506 regions to the signal region.

Sideband region	$k_{QCD} (\times 10^{-2} GeV^{-1})$	p-value
B	2.96 ± 0.64	0.24
C ₁	1.19 ± 0.45	0.93
C ₂	1.47 ± 0.37	0.42
C ₃	1.17 ± 0.55	0.98
C(weighted mean)	1.31 ± 0.26	-
D(likelihood fit)	1.31 ± 0.09	0.57

Table 4.6.: Best fit values for the parameters k_{QCD} obtained from sideband regions B,C₁,C₂,C₃. The weighted mean is determined from the three measurements made within sideband region C. The maximum likelihood value of k_{QCD} given by the simultaneous fit using sideband region D. Quotes errors are statistical only.

1507 4.3. Trigger Strategy

1508 A cross trigger based on the quantities H_T and α_T , labelled is used with varying thresholds
1509 across H_T bins to record the events used in the hadronic signal region. The α_T legs of the
1510 HT_alphaT triggers used in the analysis are chosen to fully suppress QCD multi-jet events,
1511 whilst maintaining a sustainable trigger rate. To further maintain an acceptable rate for
1512 these analysis specific triggers, only calorimeter information is used in the reconstruction
1513 of the H_T sum, leading to the necessity for Calo jets to be used within the analysis.

1514 A single object prescaled H_T trigger is used to collect events for the hadronic control
1515 region described above in Section (4.2.4).

1516 The performance of the α_T and H_T triggers used to collect data for the signal and
1517 hadronic control region is measured with respect to a reference sample collected using the
1518 muon system. This allows measurement of both the Level 1 seed and higher level triggers
1519 simultaneously, as the reference sample is collected independent of any jet requirements.

1520 The selection for the trigger efficiency measurement is identical to that described in
1521 Section (4.2.2), with the requirement of exactly one well identified muon with $p_T > 30$
1522 GeV which is subsequently ignored.

1523 The efficiencies measured for the HT_alphaT triggers in bins individual H_T and α_T
1524 legs, is summarised in Table 4.7.

H_T range (GeV)	ϵ on H_T leg (%)	ϵ on α_T leg (%)
275-325	$87.7^{+1.9}_{-1.9}$	$82.8^{+1.0}_{-1.1}$
325-375	$90.6^{+2.9}_{-2.9}$	$95.9^{+0.7}_{-0.9}$
375-475	$95.7^{+0.1}_{-0.1}$	$98.5^{+0.5}_{-0.9}$
475- ∞	$100.0^{+0.0}_{-0.0}$	$100.0^{+0.0}_{-4.8}$

Table 4.7.: Measured efficiencies of the H_T and α_T legs of the HT and HT_alphaT triggers in independent analysis bins. The product of the two legs gives the total efficiency of the trigger in a given offline H_T bin.

1525 Data for the control samples of the analysis, detailed in Section (4.2.3), are collected
 1526 using single object photon trigger for the $\gamma +$ jets sample, and a single object muon
 1527 trigger for both the $\mu +$ jets and $\mu\mu +$ jets control samples. The photon trigger is
 1528 measured to be full efficient for the threshold $p_T^{photon} > 150 GeV$, whilst the single muon
 1529 efficiency satisfying $p_T^{muon} > 30 GeV$ is measured to have an efficiency of $(88 \pm 2)\%$ that
 1530 is independent of H_T . In the case of the $\mu\mu +$ jets control sample, the efficiency is
 1531 measured to be $(95 \pm 2)\%$ for the lowest H_T bin, rising to $(98 \pm 2)\%$ for the highest H_T
 1532 bin.

1533 4.4. Measuring MC normalisation factors via H_T 1534 sidebands

1535 The theoretical cross sections of different SM processes at Next to Next Leading Order
 1536 (NNLO) and the number of MC simulated events generated for that particular process,
 1537 is typically used to determine the appropriate normalisation for a MC sample. However
 1538 within the particular high- H_T and high- \cancel{E}_T corners of kinematic phase space probed
 1539 within this search, the theoretical cross sections for various processes are far less well
 1540 understood.

1541 To mitigate the problem of theoretical uncertainties and arbitrary choices of cross
 1542 sections, the normalisation of MC samples used in the analysis are determined through
 1543 the use data sidebands. The sidebands are used to calculated sample specific correct
 1544 factors (k-factors) that are appropriate for the H_T - \cancel{E}_T phase space covered by this analysis.

1545 They are defined within the $\mu +$ jets and $\mu\mu +$ jets control sample, by the region $200 <$
 1546 $H_T < 275$, using the same jet p_T thresholds as the adjacent first analysis bin. Individual

1547 **EWK** processes are isolated within each of these control samples via requirements on
1548 jet multiplicity and the requirement on b-tags, summarised in Table 4.8. The purity of
1549 the samples are typically $> 90\%$ with any residual contamination corrected for. The
1550 resultant k-factor for each process is determined by then taking ratio of the data yield
1551 over the MC expectation in the sideband. Subsequently these k-factors are then applied
1552 to the processes within the phase space of the analysis.

Process	Selection	Observation	MC expectation	k-factor
W + jets	$\mu + \text{jets}, n_b=0, n_{jet} = 2,3$	26950	29993.2 ± 650.1	0.90 ± 0.02
$Z \rightarrow \mu\mu + \text{jets}$	$\mu\mu + \text{jets}, n_b=0, n_{jet} = 2,3$	3141	3402.0 ± 43.9	0.92 ± 0.02
$t\bar{t}$	$\mu + \text{jets}, n_b=2, n_{jet} = \geq 4$	2190	1967.8 ± 25.1	1.11 ± 0.02

Table 4.8.: k-factors calculated for different **EWK** processes. All k-factors are derived relative to theoretical cross sections calculated in **NNLO**. The k-factors measured for the $Z \rightarrow \mu\mu + \text{jets}$ processes, are also applied to the $Z \rightarrow \nu\bar{\nu} + \text{jets}$ and $\gamma + \text{jets}$ MC samples.

1553 **4.5. Determining MC Yields With Higher
1554 Statistical Precision**

1555 Reconstructing events from **EWK** processes with many b-tagged jets (≥ 3), n_b^{reco} , is largely
1556 driven by the mis-tagging of light jets within the event. This is clear when considering
1557 the main **EWK** backgrounds in the analysis, such as $t\bar{t} + \text{jets}$ events, which typically
1558 contain two b-flavoured jets from the decay of the top quarks, whilst W + jets and
1559 Z $\rightarrow \mu\mu + \text{jets}$ events will typically contain no b-flavoured jets.

1560 When the expectation for the number of n_b^{reco} is taken directly from simulation, the
1561 statistical uncertainty at large b-tag multiplicities becomes relatively large. In order to
1562 reduce this uncertainty one approach is to use the information encoded throughout all
1563 events in the simulation sample, to measure each of the four ingredients:

- 1564 1. the b-tagging efficiency in the event selection,
- 1565 2. the charm-tagging efficiency in the event selection
- 1566 3. the mis-tagging rate in the event selection,
- 1567 4. the underlying flavour distribution of the jets in the events,

1568 that determine the n_b^{reco} distribution of the process being measured. This method
1569 allows the determination of higher b-tag multiplicities to a higher degree of accuracy
1570 reducing the statical uncertainties of the MC which enter into the TF's. For the discussion
1571 that follows, these predictions are determined on average (i.e not on an event-by-event
1572 basis), and is known as the formula method.

1573 4.5.1. The formula method

1574 The assigning of jet flavours to reconstruction level jets in simulation is achieved via an
1575 algorithmic method defined as:

- 1576 • Try to find the parton that most likely determines the properties of the jet and
1577 assign that flavour as true flavour,
- 1578 • Here, the “final state” partons (after showering, radiation) are analysed (also within
1579 $\Delta R < 0.3$ of reconstructed jet cone),
- 1580 • Jets from radiation are matched with full efficiency,
- 1581 • If there is a b/c flavoured parton within the jet cone: label as b/c flavoured jet,
- 1582 • Otherwise: assign flavour of the hardest parton.

1583 Within each individual MC process and each H_T - n_{jet} bin in the analysis, the n_b^{reco}
1584 distribution is constructed in the following way:

1585 Let $N(n_b^{gen}, n_c^{gen}, n_q^{gen})$ represent the yield in simulation of events with b underlying
1586 b-quarks, c underlying c-quarks and q underlying light quarks which are matched to
1587 reconstructed jets. Light quarks are defined as those which originate from a u,d,s,g and
1588 τ jets which are grouped together having similar mis-tagging rates. Similarly defining ϵ ,
1589 β and m , which represent the measured b-tagging,c-tagging and mis-tagging efficiency
1590 averaged over all the jets within that particular analysis bin.

1591 Using this information the expected number of jets which have been b-tagged can be
1592 analytically calculated using the formula :

$$N(n_b) = \sum_{n_b^{gen} + n_c^{gen} + n_q^{gen} = n_{jet}} \sum_{n_b^{tag} + n_c^{tag} + n_q^{tag} = n_b} N(n_b^{gen}, n_c^{gen}, n_q^{gen}) \times P(n_b^{tag}, n_b^{gen}, \epsilon) \times \\ P(n_c^{tag}, n_c^{gen}, \beta) \times P(n_q^{tag}, n_q^{gen}, m), \quad (4.11)$$

with $N(n_b)$ representing the event yield where n_b jets have been b-tagged, n_b^{tag} , n_c^{tag} and n_q^{tag} represent the number of times that a particular jet flavour results in a b-tagged jet, and $P(n_b^{tag}, n_b^{gen}, \epsilon)$, $P(n_c^{tag}, n_c^{gen}, \beta)$ and $P(n_q^{tag}, n_q^{gen}, m)$ represent the binomial probabilities for that to happen.

This approach ultimately results in a more precise n_b^{reco} distribution prediction as information from throughout the entire MC sample is used to estimate the high n_b^{reco} bins.

4.5.2. Establishing proof of principle

In order to validate the procedure, the predictions obtained from the formula method summarised in Eq (4.11), are compared directly to those obtained directly from simulation. These results for the $\mu +$ jets control sample are summarised in Table 4.9, for the 0,1,2 and 3 n_b^{reco} bins.

Process	Selection	Observation	MC expectation	k-factor
---------	-----------	-------------	----------------	----------

Table 4.9.: place holder

4.5.3. Correcting Measured Efficiencies In Simulation To Data

As detailed in Section (3.3.2), it is necessary for certain p_T and η dependant corrections, to be applied to both the b-tagging efficiency and mis-tagging rates in order correct the efficiencies from simulation to the distributions seen in data. These corrections are factored in.

Show plot of before and after correction to btag/mistag rate.

These corrections come with uncertainties..

show plot of effect of scaling correction factor up and down. 2

1613 4.6. Systematic Uncertainties On Transfer Factors

1614 Since the TF's used to establish the background prediction are obtained from simulation,
1615 an appropriate systematic uncertainty is assigned to each factor to account for theoretical
1616 uncertainties [80] and limitations in the simulation modelling of event kinematics and
1617 instrumental effects.

1618 The magnitudes of these systematic uncertainties are established through a set of data
1619 driven method, in which the three independent control samples of the analysis ($\mu + \text{jets}$,
1620 $\mu\mu + \text{jets}$, $\gamma + \text{jets}$) are used to in a series of closure tests. The yields from one of these
1621 control samples, along with the corresponding TF obtained from simulation, are used to
1622 predict the yields in another control sample, using the same method of establishing a
1623 background prediction for the signal region as described in Section (4.2.3).

1624 The level of agreement between the predicted and observed yields is expressed as the
1625 ratio

$$\frac{(N_{obs} - N_{pred})}{N_{pred}}, \quad (4.12)$$

1626 while considering only the statistical uncertainties on N_{pred} , the prediction, and N_{obs} ,
1627 the observation. No systematic uncertainty is assigned to the prediction, and resultantly
1628 the level of closure is defined by the statistical significance of a deviation from the ratio
1629 from zero.

1630 This ratio is measured for each H_T bin in the analysis, allowing these closure tests to
1631 be sensitive to both the presence of any significant biases or any possible H_T dependence
1632 on the level of closure.

1633 Eight sets of closure tests are defined between the three data control samples, con-
1634 ducted independently between the two jet multiplicity ($2 \leq n_{jets} \leq 3$, $n_{jet} \geq 4$) bins.
1635 Each of these tests are specifically chosen to probe each of the different key ingredients
1636 of the simulation modelling that can affect the background prediction.

1637 Each of the different modelling components and the relevant closure tests are described
1638 below :

1639 **α_T modelling**

1640 The modelling of the α_T distribution in genuine Z_T events is probed with the $\mu +$
1641 jets control sample. This test is important to verify the approach of remove the α_T
1642 > 0.55 requirement from the $\mu +$ jets and $\mu\mu +$ jets samples to increase the precision
1643 of the background prediction. The test uses the $\mu +$ jets sample without an α_T cut
1644 to make a prediction into the $\mu +$ jets sample defined with the requirement $\alpha_T >$
1645 0.55 .

1646 **Background admixture**

1647 The sensitivity of the translation factors to the relative admixture of events from
1648 $W +$ jets and $t\bar{t}$ processes is probed by two closure tests. These tests represent
1649 an extremely conservative approach as the admixture of the background remains
1650 similar between the $\mu +$ jets sample and the signal region, contrary to the defined
1651 closure tests which make predictions between two very different admixtures of $W +$
1652 jets and $t\bar{t}$ events.

1653 Within the $\mu +$ jets sample, a W boson enriched sub-sample ($n_b = 0$) is used to
1654 predict yields in a $t\bar{t}$ enriched sub-sample ($n_b = 1$). Similarly the
1655 $t\bar{t}$ enriched sub-sample ($n_b = 1$) is also used to predict yields for a further enriched
1656 $t\bar{t}$ sub-sample ($n_b = 2$).

1657 Similarly a further closure test probes the relative contribution of $Z +$ jets to $W +$ jets
1658 and $t\bar{t}$ events, through the use of the $\mu +$ jets sample to predict yields for the $\mu\mu +$
1659 jets control sample. This closure test, also at some level probes the muon trigger
1660 and reconstruction efficiencies, given that exactly one and two muons are required
1661 by the different selections.

1662 **Consistency between control samples**

1663 An important consistency check between the $\mu\mu +$ jets jets and $\gamma +$ jets, which are
1664 both used in the prediction of the $Z \rightarrow \nu\bar{\nu}$ in the signal region, is measured by using
1665 the $\gamma +$ jets sample to predict yields for the $\mu\mu +$ jets control sample.

1666 **Modelling of jet multiplicity**

1667 The simulation modelling of the jet multiplicity within each control sample is
1668 important due to the exclusive jet multiplicity binning within the analysis. This is
1669 probed via the use of each of the three control samples to independently predict
1670 from the lower jet multiplicity category $2 \leq n_{jet} \leq 3$, to the high jet category ≥ 4 .

1671 For the case of the $\mu + \text{jets}$ and $\mu\mu + \text{jets}$ control samples this test this is also a
1672 further probe of the admixture between $W + \text{jets}/Z + \text{jets}$ and $t\bar{t}$.

1673 To test for the assumption that no H_T dependences exist within the background
1674 predictions of the analysis, the first five closure tests defined above are taken, with zeroeth
1675 and first order polynomial fits are applied to each. This is summarised in Table 4.10 and
1676 Table 4.11 which show the results for both the $2 \leq n_{jet} \leq 3$ and ≥ 4 jet multiplicity bins
1677 respectively.

Closure test	Symbol	Constant fit		Linear fit	
		Best fit value	p-value	Slope (10^{-4})	p-value
$\alpha_T < 0.55 \rightarrow \alpha_T > 0.55 (\mu + \text{jets})$	Circle	-0.06 ± 0.02	0.93	-1.3 ± 2.2	0.91
$0 \text{ b-jets} \rightarrow 1 \text{ b-jet } (\mu + \text{jets})$	Square	0.07 ± 0.02	0.98	-1.6 ± 1.6	1.00
$1 \text{ b-jets} \rightarrow 2 \text{ b-jet } (\mu + \text{jets})$	Triangle	-0.07 ± 0.03	0.76	-2.7 ± 3.0	0.76
$\mu + \text{jets} \rightarrow \mu\mu + \text{jets}$	Cross	0.10 ± 0.03	0.58	-1.1 ± 2.3	0.49
$\mu\mu + \text{jets} \rightarrow \gamma + \text{jets}$	Star	-0.06 ± 0.04	0.31	4.2 ± 4.3	0.29

Table 4.10.: A summary of the results obtained from fits of zeroeth order polynomials (i.e. a constant) to five sets of closure tests performed in the $2 \leq n_{jet} \leq 3$ bin. The final two columns show the best fit value for the slope obtained when performing a linear fit and the p-value for the linear fit.

Closure test	Symbol	Constant fit		Linear fit	
		Best fit value	p-value	Slope (10^{-4})	p-value
$\alpha_T < 0.55 \rightarrow \alpha_T > 0.55 (\mu + \text{jets})$	Circle	-0.05 ± 0.03	0.21	3.0 ± 2.9	0.21
$0 \text{ b-jets} \rightarrow 1 \text{ b-jet } (\mu + \text{jets})$	Square	-0.03 ± 0.03	0.55	-1.0 ± 1.9	0.47
$1 \text{ b-jets} \rightarrow 2 \text{ b-jet } (\mu + \text{jets})$	Triangle	-0.02 ± 0.03	0.39	1.1 ± 2.2	0.31
$\mu + \text{jets} \rightarrow \mu\mu + \text{jets}$	Cross	0.08 ± 0.07	0.08	4.8 ± 4.3	0.07
$\mu\mu + \text{jets} \rightarrow \gamma + \text{jets}$	Star	-0.03 ± 0.10	0.72	-4.0 ± 7.0	0.64

Table 4.11.: A summary of the results obtained from fits of zeroeth order polynomials (i.e. a constant) to five sets of closure tests performed in the $n_{jet} \geq q$ bin. The final two columns show the best fit value for the slope obtained when performing a linear fit and the p-value for the linear fit.

1678 Table 4.12 shows the same fits applied to the three closure tests that probe the
1679 modelling between the different n_{jet} bins. The best fit value and its uncertainty is listed
1680 for each set of closure tests in all three tables, along with the p-value of the constant and
1681 linear fits applied.

Closure test	Symbol	Constant fit		Linear fit	
		Best fit value	p-value	Slope (10^{-4})	p-value
$\mu + \text{jets}$	Inverted triangle	-0.03 ± 0.02	0.02	0.0 ± 1.0	0.01
$\mu + \text{jets}$ (outlier removed)	Inverted triangle	-0.04 ± 0.01	0.42	-1.4 ± 1.1	0.49
$\gamma + \text{jets}$	Diamond	0.12 ± 0.05	0.79	6.0 ± 4.7	0.94
$\mu\mu + \text{jets}$	Asterisk	-0.04 ± 0.07	0.20	4.9 ± 4.4	0.20

Table 4.12.: A summary of the results obtained from fits of zeroeth order polynomials (i.e. a constant) to five sets of closure tests performed in the $2 \leq n_{\text{jet}} \leq 3$ bin. The final two columns show the best fit value for the slope obtained when performing a linear fit and the p-value for the linear fit.

1682 The best fit value for the constant parameter is indicative of the level of closure,
 1683 averaged across the full range of H_T bins in the analysis, and the p-value an indicator of
 1684 any significant dependence on H_T within the closure tests. The best fit values of all the
 1685 tests are either statistically compatible with zero bias (i.e, less than 2σ from zero) or at
 1686 the level of 10% or less, with the exception of one closure test discussed below.

1687 Within Table 4.12, there exists one test that does not satisfy the above statement,
 1688 which is the $2 \leq n_{\text{jet}} \leq 3 \rightarrow n_{\text{jet}} \geq 4$ test using the $\mu + \text{jets}$ control sample. The low
 1689 p-value can be largely attributed to an outlier in the $675 < H_T < 775$ GeV bin, rather
 1690 than any significant trend in H_T . Removing this single outlier from the constant fit
 1691 performed, gives a best fit value of -0.04 ± 0.01 , $\chi^2/\text{d.o.f} = 6.07/6$. and a p-value of
 1692 0.42. These modified fit results are included within Table 4.12 .

1693 In addition the best fit values for the slope terms of the linear fits in all three tables
 1694 are of the order 10^{-4} , which corresponds to a percent level change per 100 GeV. However
 1695 in all cases, the best fit values are fully compatible with zero (within 1σ) once again with
 1696 the exception detailed above, indicating that the level of closure is H_T independent.

1697 4.6.1. Determining systematic uncertainties from closure tests

1698 Once it has been established that no significant bias or trend has been exist within
 1699 the closure tests, systematic uncertainties are determined. The statistical precision
 1700 of the closure tests is considered a suitable benchmark for determining the systematic
 1701 uncertainties that are assigned to the TF's, which are propagated through to the likelihood
 1702 fit.

1703 The systematic uncertainty band is split into five separate regions of H_T :

1704 1. $275 < H_T < 325\text{GeV}$

1705 2. $325 < H_T < 375\text{GeV}$

1706 3. $375 < H_T < 575\text{GeV}$

1707 4. $575 < H_T < 775\text{GeV}$

1708 5. $H_T > 775\text{ GeV}$

1709 Within each region the square root of the sample variance, σ^2 , is taken over the eight
1710 closure tests to determine the systematic uncertainties to be applied within that region.

1711 Using this procedure the systematic uncertainties for each region are calculated and
1712 are shown in Table 4.13, with the systematic uncertainty to be used in the likelihood
1713 model conservatively rounded up to the nearest decile, shown in brackets.

H_T band (GeV)	$2 \leq n_{jet} \leq 3$	$n_{jet} \geq 4$
$275 < H_T < 325$	6 (10)%	3 (10)%
$325 < H_T < 375$	6 (10)%	6 (10)%
$375 < H_T < 575$	7 (10)%	9 (10)%
$575 < H_T < 775$	13 (20)%	15 (20)%
$H_T > 775$	19 (20)%	21 (30)%

Table 4.13.: Calculated systematic uncertainties for the five H_T regions, determined from the closure tests. Uncertainties shown for both jet multiplicity categories. Values used within the likelihood model are conservatively rounded up to the nearest decile and shown in brackets.

1714 Figure 4.10 shows the sets of closure tests overlaid on top of grey bands that represent
1715 the H_T dependent systematic uncertainties. These systematic uncertainties are assumed
1716 to fully uncorrelated between the different n_b multiplicity categories and across the five
1717 H_T regions. This can be considered a more conservative approach given that some
1718 correlations between adjacent H_T bins could be expected due to comparable kinematics.

1719 As already referenced. These closure tests represent a conservative estimate of the
1720 systematic uncertainty in making a background prediction for the signal region. This
1721 is due to significant differences in the background composition and event kinematics
1722 between the two sub-samples used in the closure tests. This is contrary to the signal
1723 region prediction where the two sub-samples are both have a comparable background

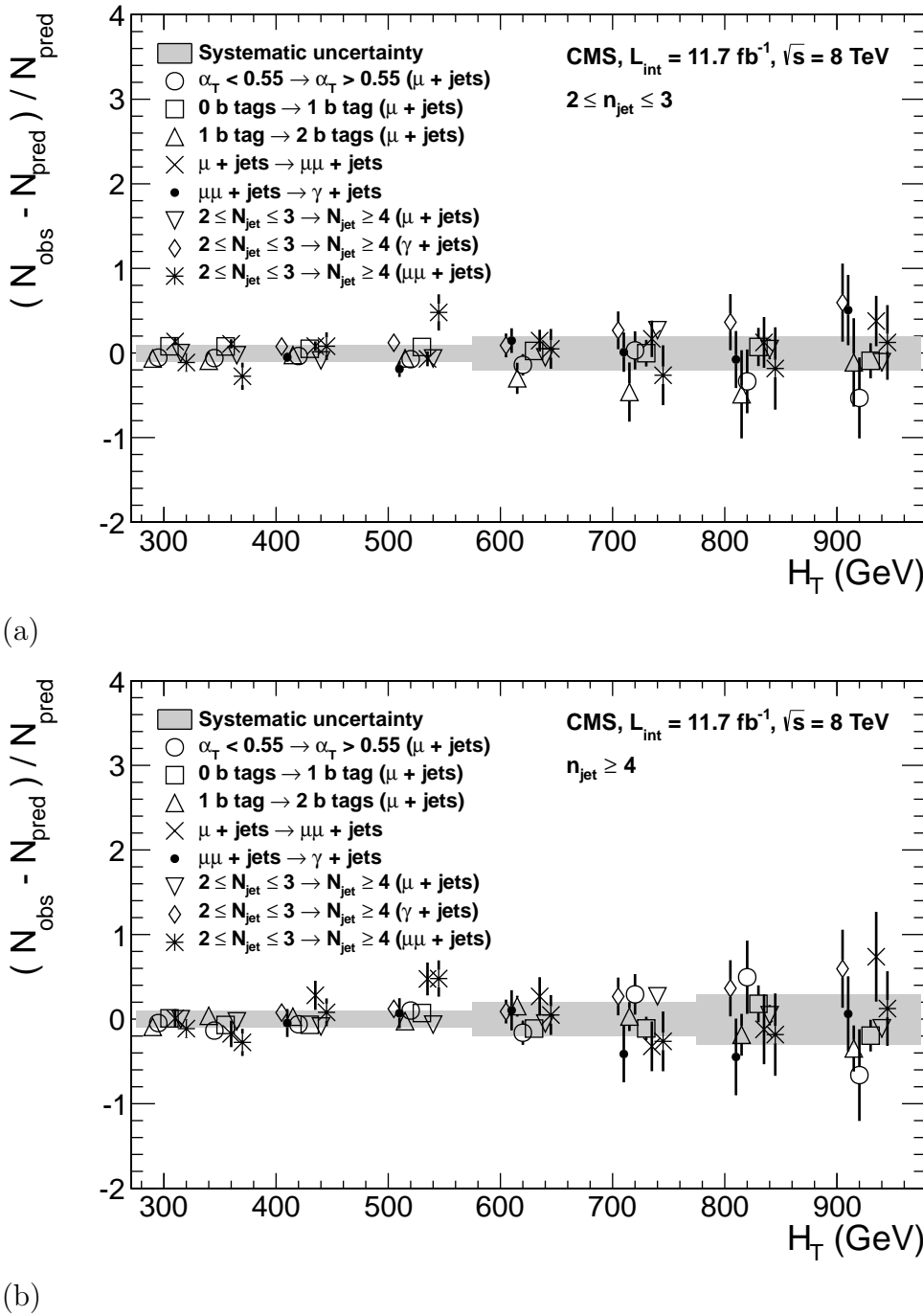


Figure 4.10.: Sets of closure tests (open symbols) overlaid on top of the systematic uncertainty used for each of the five H_T regions (shaded bands) and for the two different jet multiplicity bins: (a) $2 \leq n_{\text{jet}} \leq 3$ and (b) $n_{\text{jet}} \geq 4$.

1724 admixture and similar kinematics owing to the fact that the predictions are always made
 1725 using the same $(n_{\text{jet}}, n_b, H_T)$ bin.

1726 This point is emphasised when we examine the sensitivity of the **TF**'s to a change
1727 in the admixture of $W + \text{jets}$ and $t\bar{t}$ with the control and signal samples. This is
1728 accomplished by varying the cross sections of the $W + \text{jets}$ and $t\bar{t}$ by +20% and -20%,
1729 respectively. Figures C.2 and C.3 within Appendix C, show the effect upon the closure
1730 tests for both jet multiplicity categories. Given these variations in cross sections, the
1731 level of closure is found to be significantly worse, with biases as large as $\sim 30\%$, most
1732 apparent in the lowest H_T bins. However the **TF**'s used to extrapolate from control to
1733 signal are seen to change only at the percent level by this large change in cross section,
1734 shown in Table C.1.

1735 Given the robust behaviour of the translation factors with respect to large (and
1736 opposite) variations in the $W + \text{jets}$ and $t\bar{t}$ cross sections, one can assume with confidence
1737 that any bias in the translation factors is adequately (and conservatively) covered by the
1738 systematic uncertainties used in the analysis.

1739 4.7. Statistical Framework

1740 For a given category of events satisfying requirements on both n_{jet} and n_b^{reco} , a likelihood
1741 model of the observations in multiple data samples is used to gauge agreement between
1742 the observed yields in the hadronic signal region, and the predicted yields obtained from
1743 the control samples. In addition to checking whether the predictions are compatible with
1744 a **SM** only hypothesis, the likelihood model is also used to test for the presence of a
1745 variety of signal models.

1746 4.7.1. Hadronic sample

1747 Let N be the number of bins on H_T , with n^i the number of events observed satisfying
1748 all selection requirements in each H_T bin i. The likelihood of the observations can then
1749 be written :

$$L_{had} = \prod_i \text{Pois}(n^i | b^i + s^i), \quad (4.13)$$

₁₇₅₀ where b^i represents the expected SM background ($EW K_i + QCD_i$) and s^i the expected
₁₇₅₁ number of signal events from the different SMS models interpreted. Pois refers to the
₁₇₅₂ Poission distribution of these values and is defined as :

$$\text{Pois}(\chi|\lambda) = \frac{\lambda^\chi \exp^{-\lambda}}{k!}. \quad (4.14)$$

₁₇₅₃ **4.7.2. H_T evolution model**

Chapter 5.

¹⁷⁵⁴ Searches For Natural SUSY With ¹⁷⁵⁵ B-tag Templates.

¹⁷⁵⁶ Within this chapter a complimentary technique is discussed as a means to predict the
¹⁷⁵⁷ distribution of three and four reconstructed b-quark jets in an event. The recent discovery
¹⁷⁵⁸ of the Higgs boson has made third-generation “Natural SUSY” models attractive, given
¹⁷⁵⁹ that light top and bottom squarks are a candidate to stabilise divergent loop corrections
¹⁷⁶⁰ to the Higgs boson mass.

¹⁷⁶¹ Using the α_T search as a base, a simple templated fit is employed to estimate the
¹⁷⁶² SM background in higher b-tag multiplicities (3-4) from a region of a low number of
¹⁷⁶³ reconstructed b-jets (0-2). As a proof-of-concept, the procedure after being shown to
¹⁷⁶⁴ close in simulation, is applied to the SM enriched $\mu +$ jets control sample of the α_T
¹⁷⁶⁵ all-hadronic search detailed in Chapter 4. To highlight the relative insensitivity of the
¹⁷⁶⁶ choice of the b-tagging algorithm working points in the effectiveness of the procedure,
¹⁷⁶⁷ results are presented using the CSV tagger (introduced in Section (3.3.2)) for the “Loose”,
¹⁷⁶⁸ “Medium” and “Tight” working points.

¹⁷⁶⁹ 5.1. Concept

¹⁷⁷⁰ The dominant SM backgrounds most SUSY searches are typically $t\bar{t} +$ jets, $W +$ jets and
¹⁷⁷¹ $Z \rightarrow \nu\bar{\nu} +$ jets. These process are characterised by typically having zero or two underlying
¹⁷⁷² b-quarks per event. The first step in this approach is to categorise two templates to be
¹⁷⁷³ fitted to the low n_b^{reco} multiplicity in terms of these underlying b-quark event topologies :

₁₇₇₄ Z0 - W + jets, Z $\rightarrow \nu\bar{\nu}$ + jets, DY + jets

₁₇₇₅ Z2 - $t\bar{t}$, single top

₁₇₇₆ where Z0 and Z2 represent processes which have an underlying b-quark content of
₁₇₇₇ zero or two respectively.

₁₇₇₈ Both these templates can be generated through the application of the relevant event
₁₇₇₉ selection and taking the underlying n_b^{reco} distribution directly from simulation. However
₁₇₈₀ as discussed within Section (4.5), there are large uncertainties for high n_b^{reco} multiplicities
₁₇₈₁ due to limited MC statistics. This is particularly prominent for the Z0 templates, where
₁₇₈₂ the number of reconstructed b-tags is driven primarily by the light-quark mis-tagging
₁₇₈₃ rate. Therefore to improve the statistical precision of the predictions the formula method,
₁₇₈₄ introduced in Section (4.5.1) is used.

₁₇₈₅ The generation of these templates is then dependant upon the jet-flavour content and
₁₇₈₆ b-tagging rate within the phase space of interest, with the tagging probabilities of a jet
₁₇₈₇ being a function of the jet p_T , the pseudo-rapidity $|\eta|$, and the jet-flavour. This can be
₁₇₈₈ observed in Figure 5.1, where the b-tagging / c-quark mis-tagging / light mis-tagging
₁₇₈₉ efficiency for the three working points of the CSV tagger is shown as a function of jet p_T .

₁₇₉₀ Before the templates are generated, the relevant jet p_T and η corrections are applied
₁₇₉₁ to correct simulation to data, as specified in Section (4.5.3), to then determine the average
₁₇₉₂ tagging rates per analysis bin.

₁₇₉₃ These two templates are then fit to data in the low n_b^{reco} region (0-2). The fit result
₁₇₉₄ is used, along with the knowledge of the template shapes, to extrapolate an estimate to
₁₇₉₅ the high n_b^{reco} signal region (3,4), which is then compared to what is observed in data.

₁₇₉₆ This method can, in principle, be applied to any analysis where the signal hypothesis
₁₇₉₇ has a larger underlying b-quark spectra than the SM backgrounds, as it solely relies on
₁₇₉₈ fitting to the shape of the n_b^{reco} distribution.

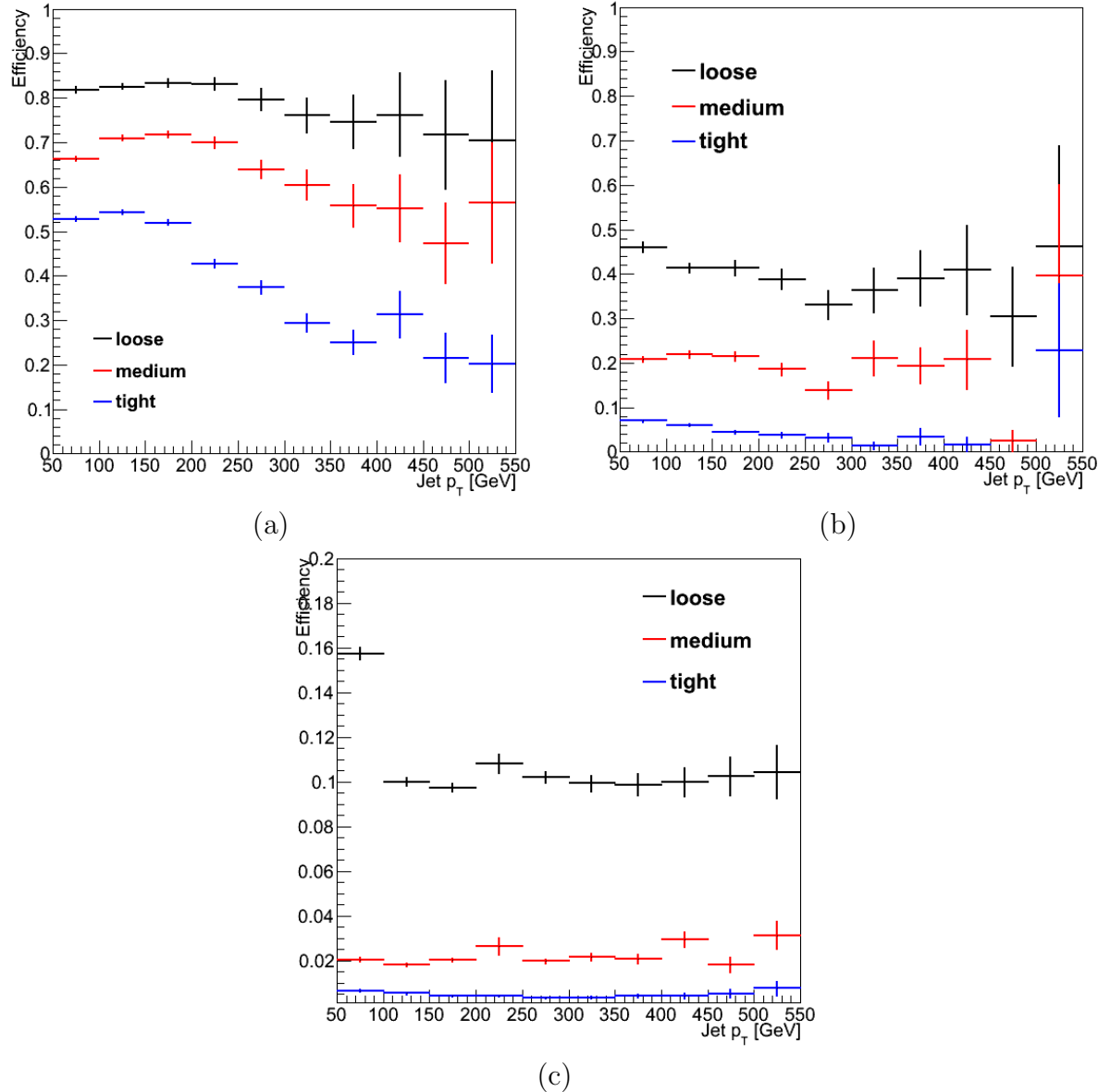


Figure 5.1.: The b-tagging (a), c-quark mis-tagging (b), and light-quark mis-tagging rate (c) as measured in simulation after the α_T analysis, $\mu + \text{jets}$ control sample selection in the region $H_T > 375$.

¹⁷⁹⁹ 5.2. Application to the α_T search

¹⁸⁰⁰ As detailed in the previous chapter, the α_T analysis is a search for **SUSY** particles
¹⁸⁰¹ in all-hadronic final states, utilising the kinematic variable α_T to suppress QCD to a
¹⁸⁰² negligible level. **SM** enriched control samples are used to estimate the background within
¹⁸⁰³ an all-hadronic signal region.

1804 The selection for the $\mu +$ jets control samples defined in Section (4.2.3) is used to
1805 demonstrate the template fitting procedure both conceptually in simulation, and also
1806 when applied in data. This is chosen, as such a selection is dominated by events stemming
1807 from the SM processes with little or no signal contamination from potential new physics..
1808 Neither are contributions from rate SM processes with a higher underlying b-quark
1809 content (e.g. $t\bar{t}bb$) expected. For these reasons, there is a degree of confidence that the
1810 procedure should close when applied to this phase space.

1811 The analysis presented here is binning in source jet multiplicity bins, of 3,4 and ≥ 5
1812 reconstructed jets per event (di-jet events are not included as there is no contribution
1813 to the high n_b^{reco} region (3,4)) , in order to reduce the kinematic jet p_T dependence.
1814 Furthermore the analysis is split into three H_T regions,

1815 • 275-325 GeV

1816 • 325-375 GeV

1817 • > 375 GeV

1818 contrary to the eight used within the α_T analysis. Templates for both underlying
1819 b-quark content hypotheses are then generated for the nine defined analysis bins.

1820 5.2.1. Proof of principle in simulation

1821 In order to demonstrate that the template procedure produces accurate predictions
1822 within simulation, the simulation samples in the analysis are firstly split into two to allow
1823 for statistically independent fits to be performed.

1824 By combining the relevant ingredients necessary to employ the formula method, n_b^{reco}
1825 templates for $Z = 0$ and $Z= 2$ are generated individually for each n_{jet} and H_T bin using
1826 one half of each simulation sample. A fit of these two templates is then performed in the
1827 low n_b^{reco} (0-2) region, back to the sum of the other halves of each simulation sample in
1828 order to check that the relevant information can be recovered in the n_b^{reco} signal region
1829 (3-4).

1830 The fits are performed independently within each of the defined analysis bins to
1831 reduce the dependence of the shapes of these distributions on simulation. The half of
1832 the simulation sample for which the templates are fitted too, are taken directly from
1833 simulation, extending this procedure to also be a validation of the formula method to

1834 accurately estimate the n_b^{reco} distribution. Additionally as this test is performed in
 1835 simulation, the relevant corrections of the b-tagging rates between data and simulation
 1836 are *not* applied.

1837 Within Figure 5.2, the results of this fitting procedure is shown for each CSV working
 1838 point. Results are presented for the $n_{jet} \geq 5$ category, using the $\mu +$ jets control sample
 1839 selection in the inclusive $H_T > 375$ GeV analysis bin. The grey bands represent the
 1840 statistical uncertainty on the template shapes. Additional fits are shown for other n_{jet}
 1841 category within Appendix D.1.

1842 Furthermore the extrapolated fit predictions within the high n_b^{reco} signal region, are
 1843 summarised for all H_T bins and working points in Table 5.1.

H_T	275-325	325-375	>375
Loose working point			
Simulation $n_b = 3$	344.0 ± 6.8	158.8 ± 4.5	324.9 ± 6.5
Template $n_b = 3$	347.5 ± 11.6	162.6 ± 4.7	322.9 ± 6.9
Simulation $n_b = 4$	29.8 ± 1.9	11.1 ± 1.1	40.2 ± 2.4
Template $n_b = 4$	32.6 ± 2.0	13.0 ± 1.0	37.0 ± 1.8
Medium working point			
Simulation $n_b = 3$	58.2 ± 2.87	33.3 ± 2.1	72.1 ± 3.1
Template $n_b = 3$	60.1 ± 1.9	32.1 ± 1.5	70.8 ± 2.3
Simulation $n_b = 4$	1.0 ± 0.4	0.3 ± 0.2	1.5 ± 0.4
Template $n_b = 4$	1.2 ± 0.1	0.4 ± 0.1	2.2 ± 0.2
Tight working point			
Simulation $n_b = 3$	58.2 ± 2.87	33.3 ± 2.1	72.1 ± 3.1
Template $n_b = 3$	60.1 ± 1.9	32.1 ± 1.5	70.8 ± 2.3
Simulation $n_b = 4$	1.0 ± 0.4	0.3 ± 0.2	1.5 ± 0.4
Template $n_b = 4$	1.2 ± 0.1	0.4 ± 0.1	2.2 ± 0.2

Table 5.1.: Summary of the fit predictions in the n_b^{reco} signal region for $n_{jet} = 3, = 4, \geq 5$. The fit region is $n_b^{reco} = 0, 1, 2$ and simulation yields are normalised to an integrated luminosity of 10 fb^{-1} . The uncertainties quoted on the template yields are purely statistical.

1844 The pull distributions for all the fits performed are compatible with a mean of zero
 1845 and standard distributions, see Appendix D.2.

1846 The good overall agreement summarised in the table validates both the formula method
 1847 used to generate the templates as well as the fitting method itself. The application of
 1848 this method to the same selection in data is used to demonstrate necessary control over
 1849 the efficiency and mis-tagging rates.

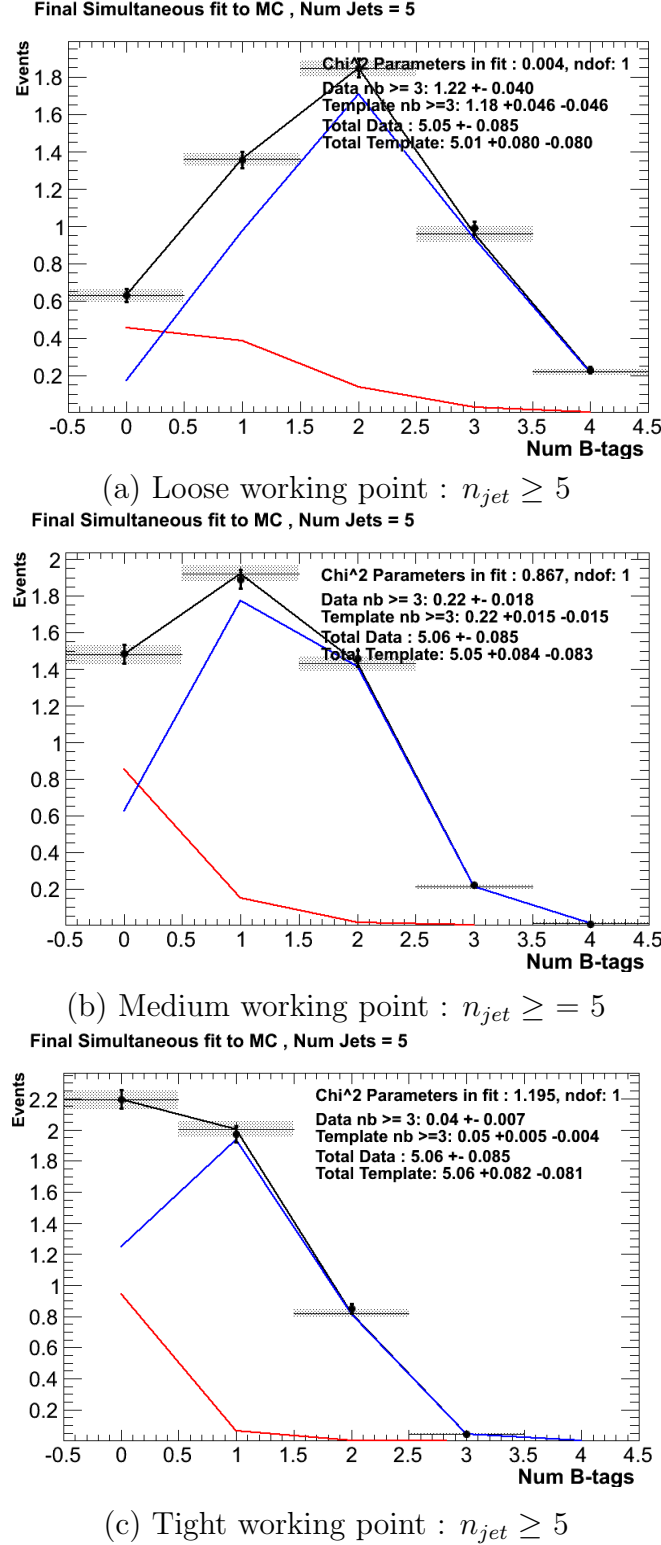


Figure 5.2.: The results of fitting the $Z = 0$ and $Z = 2$ templates to the $n_b^{reco} = 0, 1, 2$ bins taken directly from simulation in the region $H_T > 375$ GeV, for the $n_{jet} \geq 5$ category. The red template represents $Z = 0$, while the blue template represents $Z = 2$. Grey bands represent the statistical uncertainty of the fit. The χ^2 parameter displayed represents the goodness of fit to the low n_b^{reco} (0-2) control region.

1850 5.2.2. Results in a data control sample

1851 The method above is now applied to the 2012 8 TeV dataset in the $\mu +$ jets control
 1852 sample, to establish the validity of this method in data. The relevant data to simulation
 1853 scale factors are applied to get corrected values of the efficiency and mis-tagging rates
 1854 measured in data [64] [81].

1855 Figure 5.3 show the the results of the templates derived from simulation to each of
 1856 the three defined H_T bins, in the $n_{jet} \geq 5$ category for the medium working point CSV
 1857 tagger (the same working point used within the α_T analysis). Grey bands represent the
 1858 statistical uncertainty of the fit combined in quadrature with the systematic uncertainties
 1859 of varying the data to simulation scale factors up and down by their measured systematic
 1860 uncertainties. Additional fit results for the other working points are found in Appendix
 1861 D.3

1862 The numerical results and extrapolation to the $n_b^{reco} = 3, 4$ bins for all H_T and working
 1863 points is shown in Table 5.2.

H_T	275-325	325-375	>375
Loose working point			
Data $n_b = 3$	717	338	618
Template $n_b = 3$	782.6 ± 16.8	340.6 ± 10.2	601.9 ± 14.2
Data $n_b = 4$	68	39	68
Template $n_b = 4$	75.0 ± 2.7	27.6 ± 1.3	71.6 ± 2.6
Medium working point			
Data $n_b = 3$	124	73	137
Template $n_b = 3$	124.3 ± 2.3	62.0 ± 1.7	121.9 ± 2.5
Data $n_b = 4$	1	1	3
Template $n_b = 4$	2.6 ± 0.1	1.3 ± 0.1	4.0 ± 0.1
Tight working point			
Data $n_b = 3$	21	13	23
Template $n_b = 3$	26.7 ± 0.5	11.7 ± 0.3	21.9 ± 0.5
Data $n_b = 4$	0	0	0
Template $n_b = 4$	0.23 ± 0.07	0.09 ± 0.04	0.29 ± 0.09

Table 5.2.: Summary of the fit predictions in the n_b^{reco} signal region of the $\mu +$ jets control sample, for $n_{jet} = 3, = 4, \geq 5$. The fit region is $n_b^{reco} = 0, 1, 2$ using 11.5 fb^{-1} of data at $\sqrt{s} = 8\text{TeV}$. The uncertainties quoted on the template yields are purely statistical.

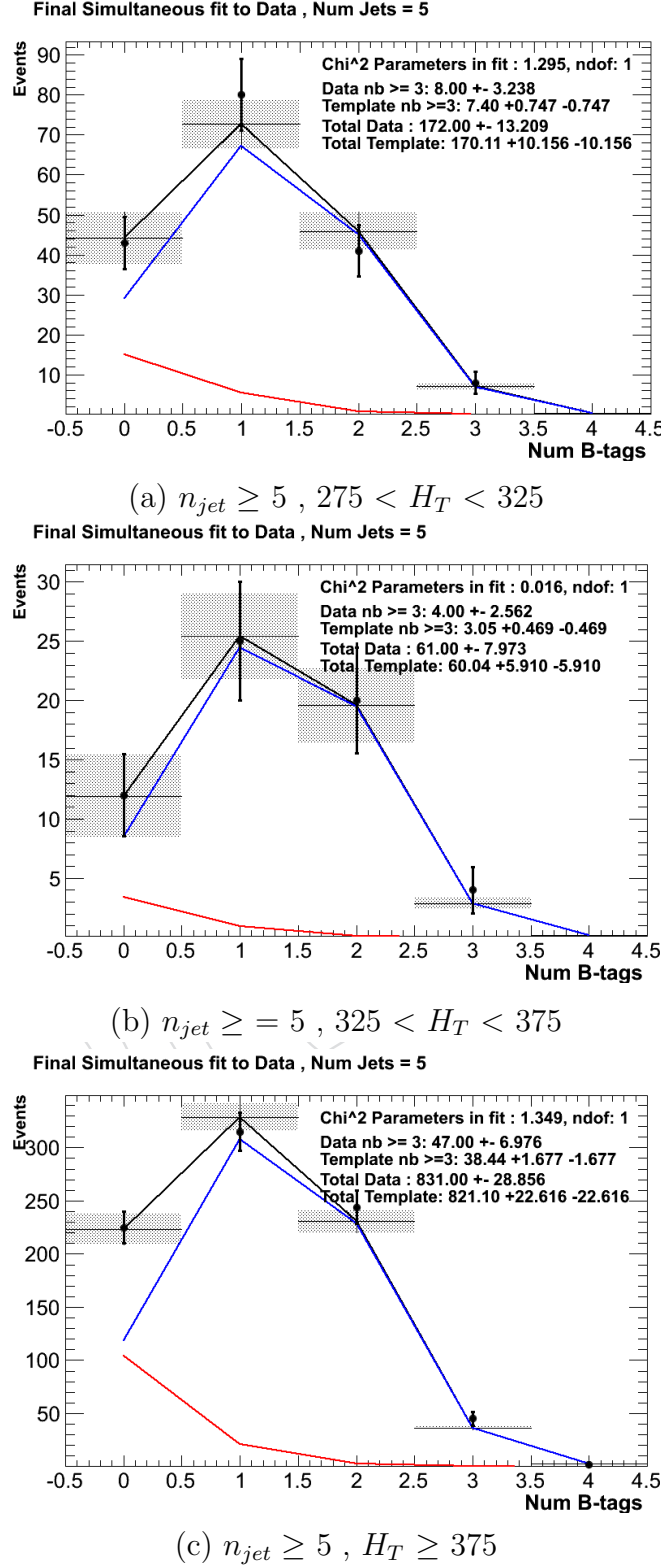


Figure 5.3.: The results of fitting the $Z = 0$ and $Z = 2$ templates to the $n_b^{reco} = 0, 1, 2$ bins taken directly from data, for the $n_{jet} \geq 5$ category and medium CSV working point. The red template represents $Z = 0$, while the blue template represents $Z = 2$. The χ^2 parameter displayed represents the goodness of fit to the low n_b^{reco} (0-2) control region.

1864 The agreement for all working points demonstrates a good control of the b-tagging
1865 efficiency and mis-tagging rates and gives confidence in the method outlined.

1866 **5.2.3. Application to the α_T hadronic search region**

1867 As an accompaniment to the background estimation methods outlined by the α_T search.
1868 The b-tag template method offers a complimentary way of estimated the background
1869 within the hadronic signal region of the search.

1870 **5.3. Conclusions**

1871 A **SUSY** signature such as one from gluino-induced third-generation squark production,
1872 would result in a final state with an underlying b-quark content greater than two. In
1873 order to be able to discriminate such signatures from the **SM** background, templates are
1874 generated based on a parameterisation of the number of the **SM** processes, where the
1875 underlying b-quarks per event is typically zero or two. These templates are then fit to
1876 data in a low n_b^{reco} (0-2) control region in order to extrapolate a prediction in a high
1877 n_b^{reco} (3-4) signal region.

1878 The method was demonstrated both in simulation and also in data, using the **SM**
1879 enriched $\mu +$ jets selection from the α_T search, to prove conceptually and experimentally
1880 that the method works and there is adequate control over the efficiency and mis-tagging
1881 rates in data for all working points of the **CSV** tagger. Additionally this method was
1882 also applied to the α_T analysis signal region where good agreement is observed between
1883 data and the background estimation method of the α_T analysis.

Chapter 6.

¹⁸⁸⁴ Results and Interpretation

¹⁸⁸⁵ Results at 12fb 8TeV

¹⁸⁸⁶ 6.1. Statistical Interpretation

¹⁸⁸⁷ Likelihood stuff

¹⁸⁸⁸ 6.2. Interpretation in Simplified Signal Models

¹⁸⁸⁹ Result interpretation

¹⁸⁹⁰

Appendix A.

¹⁸⁹¹ Miscellaneous

¹⁸⁹² A.1. Noise Filters

¹⁸⁹³ For Calo jets the following criteria were applied:

Loose CaloJet Id	
Variable	Definition
$f_{HPD} < 0.98$	Fraction of jet energy contributed from “hottest” HPD , which rejects HCAL noise.
$f_{EM} > 0.01$	Noise from the HCAL is further suppressed by requiring a minimal electromagnetic component to the jet f_{EM} .
$N_{hits}^{90} \geq 2$	Jets that have $> 90\%$ of its energy from a single channel are rejected, to serve as a safety net that catches jets arising from undiagnosed noisy channels.

Table A.1.: Criteria for a reconstructed jet to pass the loose calorimeter jet id.

¹⁸⁹⁴ For PF jets the following criteria were applied:

Loose PF jet Id	
Variable	Definition
$\text{nfhJet} < 0.99$	Fraction of jet composed of neutral hadrons. HCAL noise tends to populate high values of neutral hadron fraction.
$\text{nemfJet} < 0.99$	Fraction of jet composed of neutral electromagnetic energy. ECAL noise tends to populate high values of neutral EM fraction.
$\text{nmultiJet} > 1$	Number of constituents that jet is composed from.
$\text{chfJet} > 0$	Fraction of jet composed of charged hadrons.
$\text{cmultiJet} > 0$	Number of charged particles that compose jet.
$\text{cemfJet} < 0.99$	Fraction of jet composed of charged electromagnetic energy.

Table A.2.: Criteria for a reconstructed jet to pass the loose PF jet id.

1895 The following noise filters are applied, to remove events with spurious, non-physical
1896 jets or missing transverse energy.

Noise Filters	
Variable	Definition
CSC tight beam halo filter	As proton beams circle the LHC , proton interactions with the residual gas particles or the beam collimators can occur, producing showers of secondary particles which can interact with the CMS detector.
HBHE noise filter with isolated noise rejection	Anomalous noise in the HCAL not due to electronics noise, but rather due to instrumentation issues associated with the HPD 's and Readout Boxes (RBXs).
HCAL laser filter	The HCAL uses laser pulses for monitoring the detector response. Some laser pulses have accidentally been fired in the physics orbit, and ended up polluting events recorded for physics analysis.
ECAL dead cell trigger primitive (TP) filter	EB and EE have single noisy crystals which are masked in reconstruction. Use the Trigger Primitive (TP) information to assess how much energy was lost in masked cells.
Bad EE Supercrystal filter	Two supercrystals in EE are found to occasionally produce high amplitude anomalous pulses in several channels at once, causing a large E_T' spike.
ECAL Laser correction filter	A laser calibration multiplicative factor is applied to correct for transparency loss in each crystal during irradiation. A small number of crystals receive unphysically large values of this correction and become very energetic, resulting in E_T' .

Table A.3.: Noise filters that are applied to remove spurious and non-physical E_T' signatures within the **CMS** detector.

¹⁸⁹⁷ A.2. Primary Vertices

¹⁸⁹⁸ The pileup per event is defined by the number of 'good' reconstructed primary vertices
¹⁸⁹⁹ in the event, with each vertex satisfying the following requirements

Good primary vertex requirement	
Variable	Definition
$N_{dof} > 4$	The number of degree of freedom, from the vertex fit to compute the best estimate of the vertex parameters.
$ \Delta z_{vtx} < 24\text{cm}$	The distance, $ \Delta z_{vtx} $, to the position of the closest HLT primary vertex.
$\rho < 2\text{cm}$	The perpendicular distance of track position to the beam spot.

Table A.4.: Criteria for a vertex in an event to be classified as a 'good' reconstructed primary vertex.

Appendix B.

1900 L1 Jets

1901 B.1. Jet matching efficiencies

1902 The single jet turn-on curves are derived from events independent of whether the leading
1903 jet in an event is matched to a Level 1 jet using ΔR matching detailed in Section (3.4.3)
1904 or not. These turn-ons are produced from events which are not triggered on jet quantities
1905 and therefore it is not guaranteed that the lead jet of an event will be seeded by a Level
1906 1 jet. Figure B.1 shows the particular matching efficiency of a lead jet to a L1 jet.

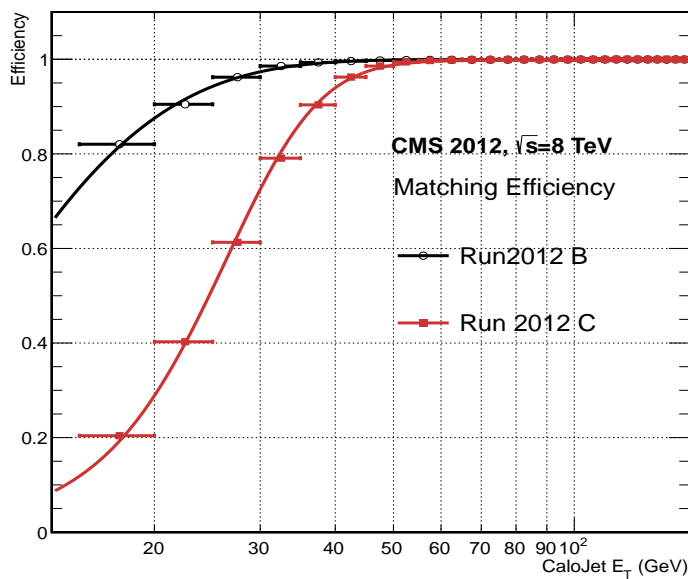


Figure B.1.: Leading jet matching efficiency as a function of the offline CaloJet E_T , measured in an isolated muon triggered dataset in the 2012B and 2012C run periods.

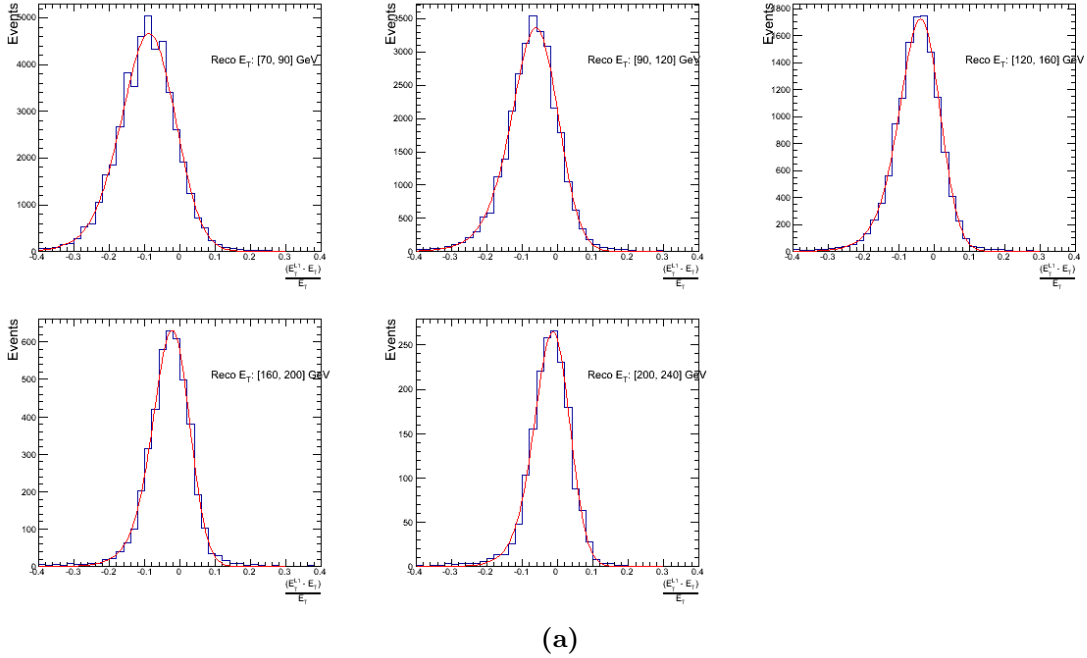
Run Period	μ	σ
2012B	6.62 ± 0.01	0.79 ± 0.03
2012C	19.51 ± 0.03	7.14 ± 0.02

Table B.1.: Results of a cumulative EMG function fit to the turn-on curves for the matching efficiency of the leading jet in an event to a Level-1 jet in run 2012C and 2012B data, measured in an isolated muon triggered sample. The turn-on point, μ , and resolution, σ , are measured with respect to offline Calo Jet E_T .

It can be seen that the turn on is sharper during the 2012B run period. The seed threshold requirement of a 5 GeV jet seed in run 2012C results in more events in which even the lead offline jet does not have an associated L1 jet. For larger jet E_T thresholds, typical of thresholds used in physics analyses, 100% efficiency is observed.

The matching efficiencies have a μ values of 6.62 GeV and 19.51 GeV for Run 2012B and 2012C respectively and is shown in Table B.1.

B.2. Leading Jet Energy Resolution



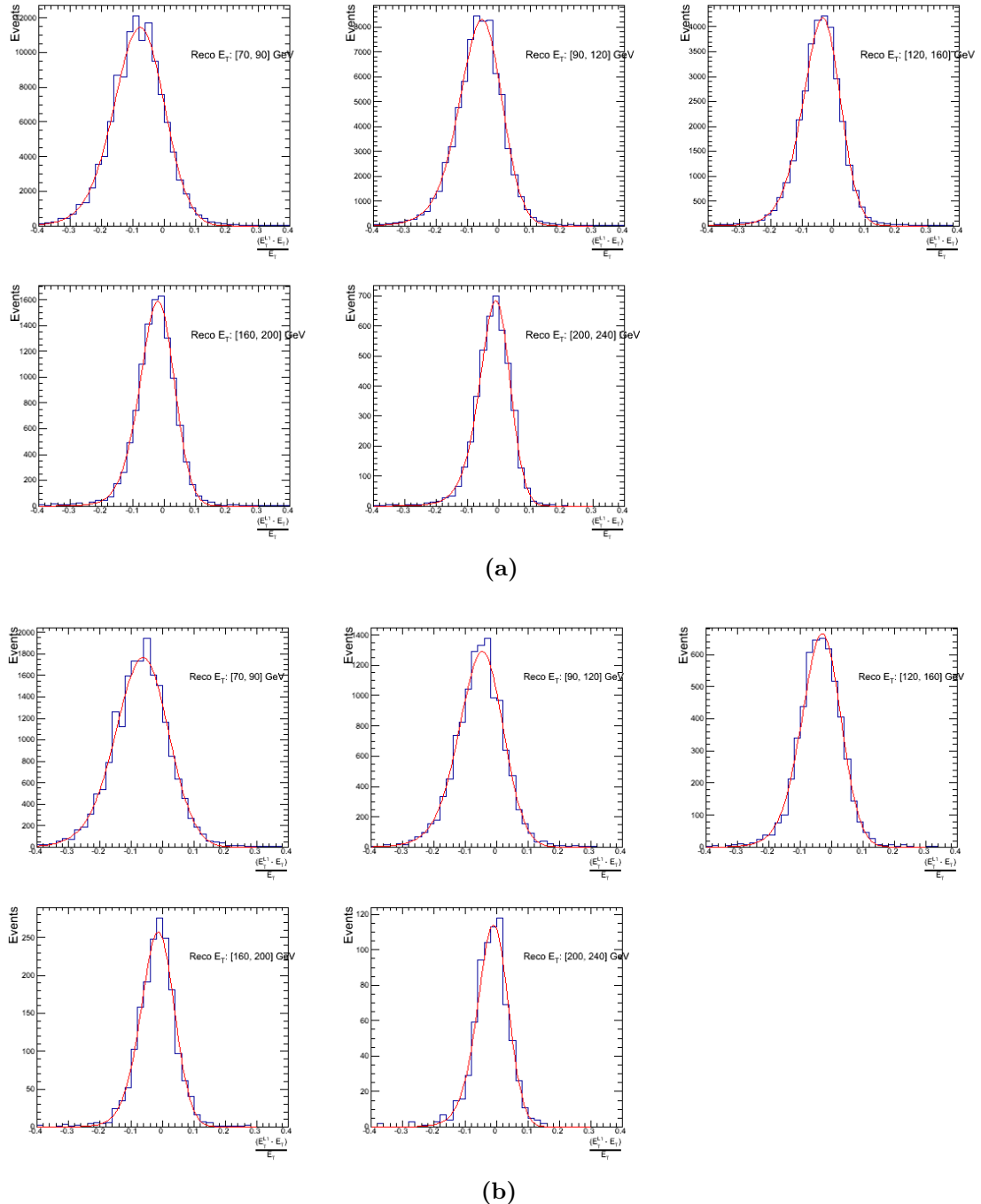
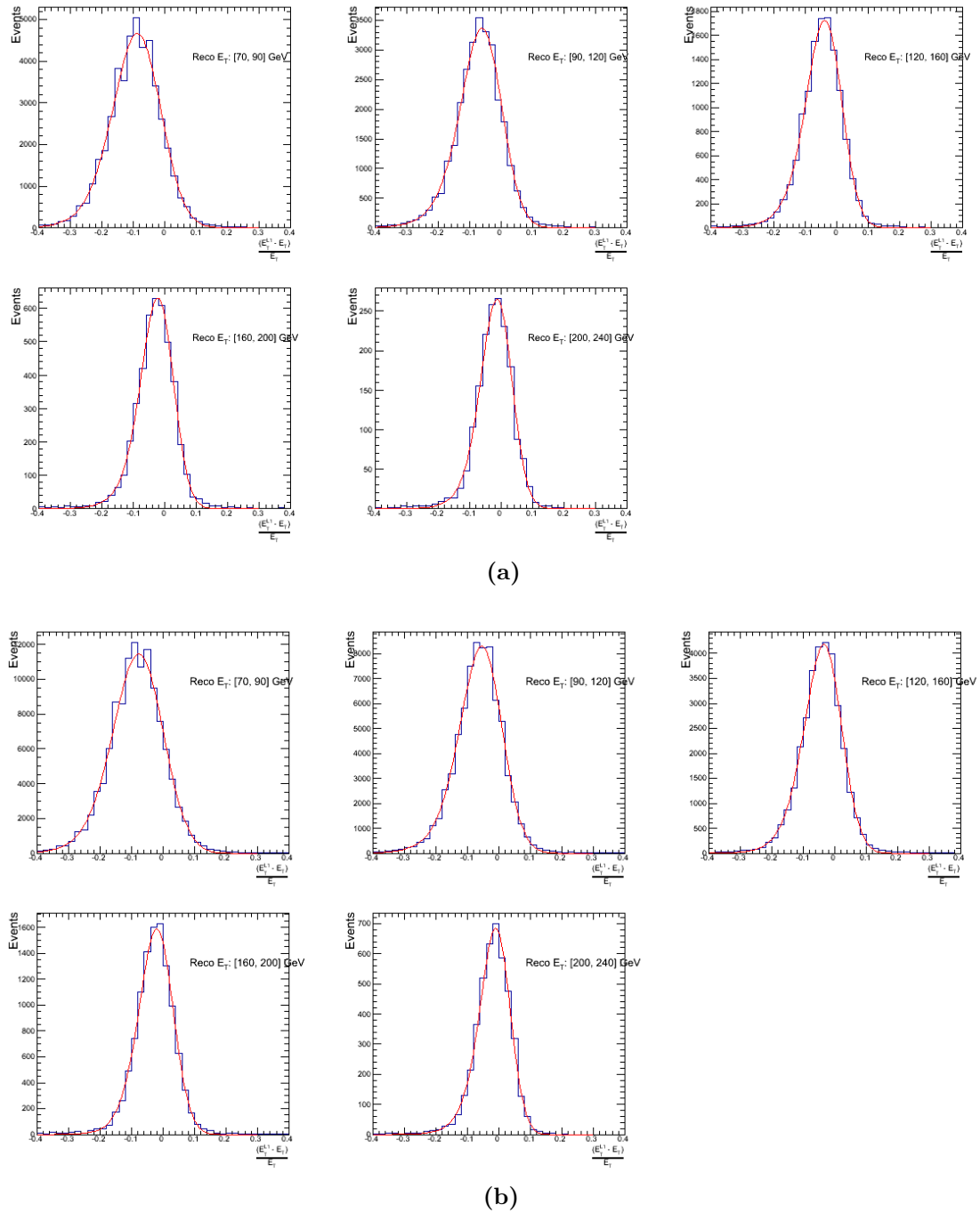
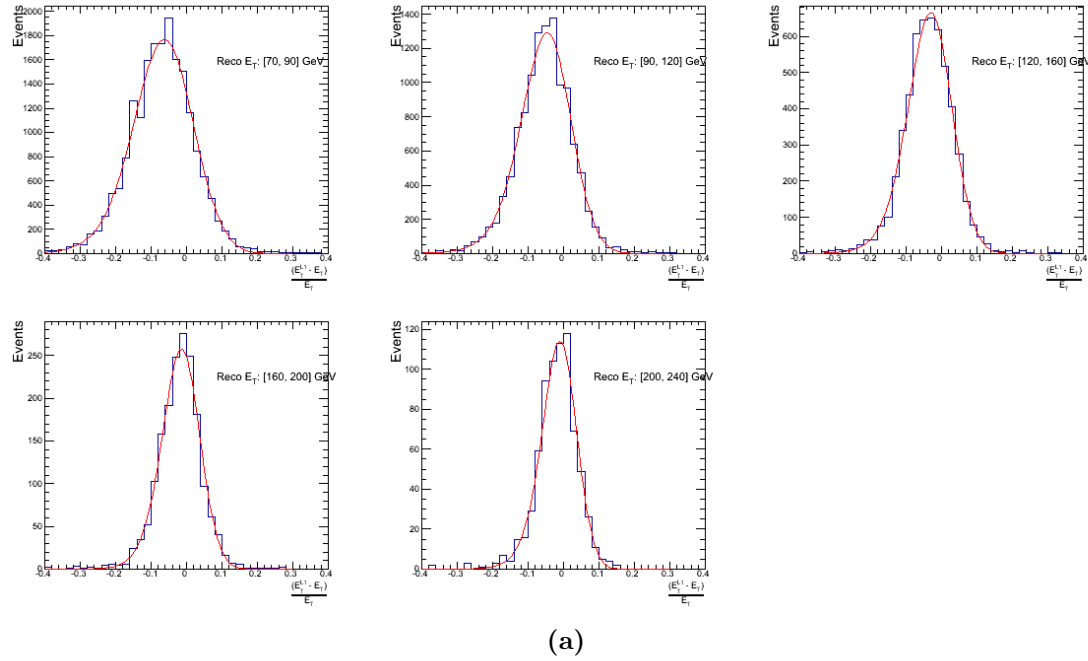


Figure B.2.: Resolution plots of the leading offline jet Calo E_T measured as a function of $\frac{(\text{L1 } E_T - \text{Offline } E_T)}{\text{Offline } E_T}$ for low (a), medium (b) and high (c) pile-up conditions.





(a)

Figure B.3.: Resolution plots of the leading offline jet PF E_T measured as a function of $\frac{(L1 E_T - Offline E_T)}{Offline E_T}$ for low (a), medium (b) and high (c) pile-up conditions.

1914 B.3. Resolution for Energy Sum Quantities

1915 The following plots show the resolution parameters for the four energy sum quantities as
 1916 a function of the quantity (q) itself. In this case, The mean and RMS of the individual
 1917 $\frac{(L1 q - Offline q)}{Offline q}$ distributions, in bins of the quantity q is displayed.

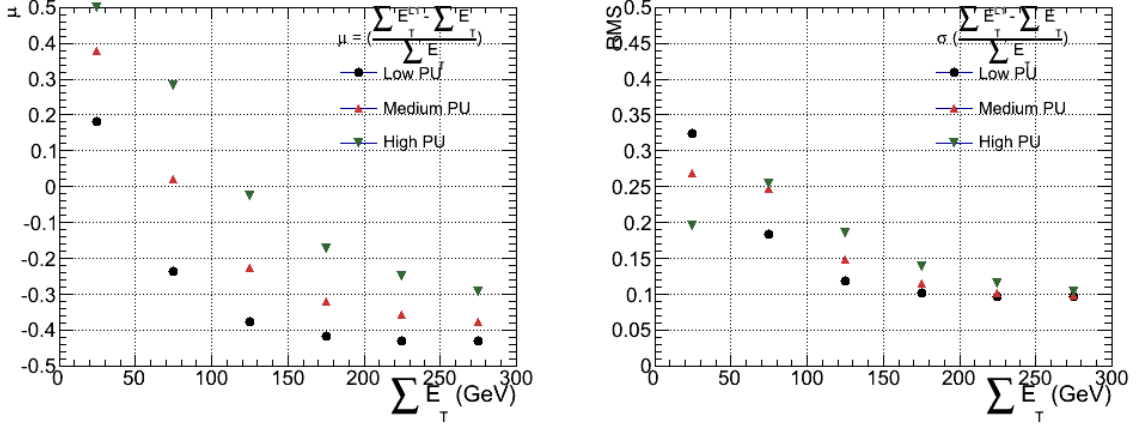


Figure B.4.: $\sum E_T$ resolution parameters in bins of Calo $\sum E_T$ measured for the defined low, medium and high pile up conditions. The plots show the mean μ (left), resolution σ (RMS) of the $\frac{\Delta q}{q}$ distributions.

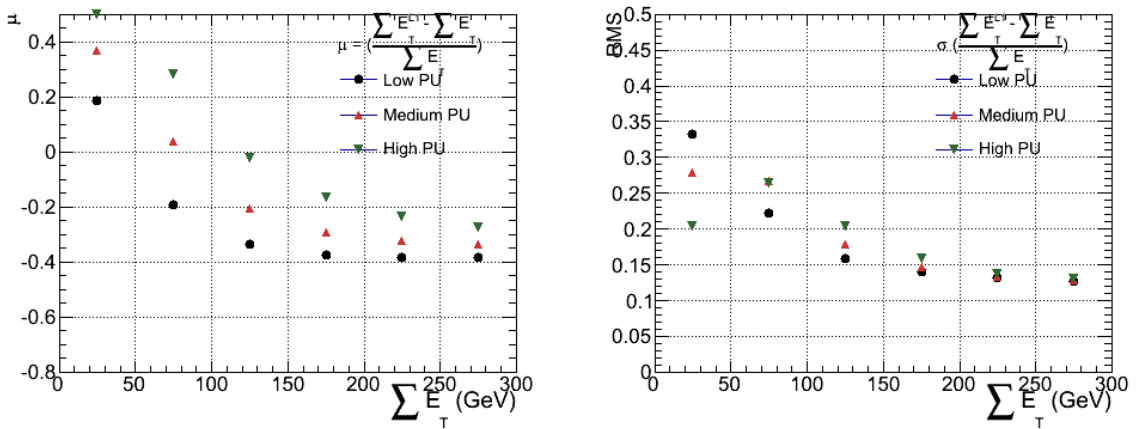


Figure B.5.: $\sum E_T$ resolution parameters in bins of PF $\sum E_T$ measured for the defined low, medium and high pile up conditions. The plots show the mean μ (left), resolution σ (RMS) of the $\frac{\Delta q}{q}$ distributions.

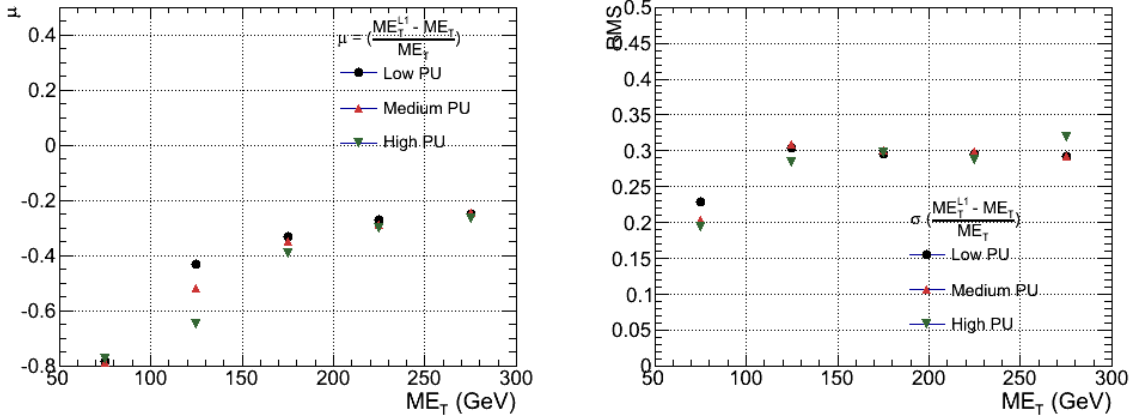


Figure B.6.: \mathcal{E}_T resolution parameters in bins of Calo \mathcal{E}_T measured for the defined low, medium and high pile up conditions. The plots show the mean μ (left), resolution σ (RMS) of the $\frac{\Delta q}{q}$ distributions.

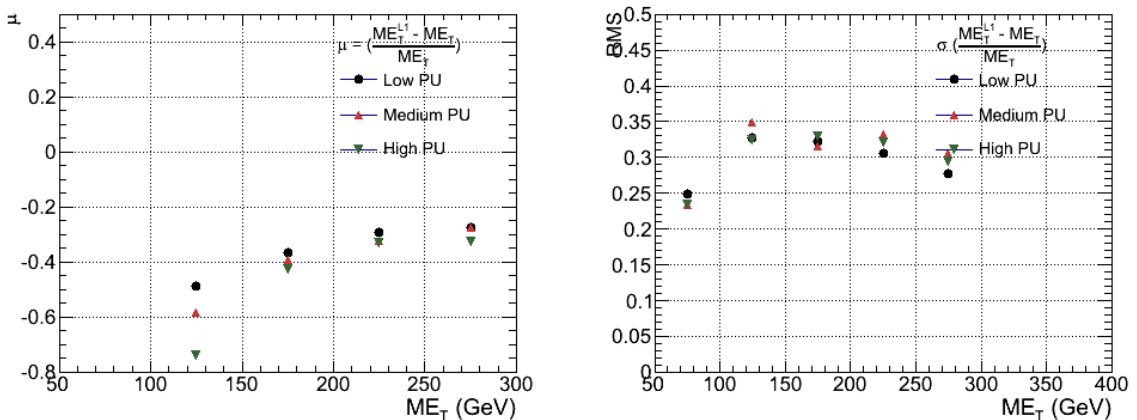


Figure B.7.: \mathcal{E}_T resolution parameters in bins of PF \mathcal{E}_T measured for the defined low, medium and high pile up conditions. The plots show the mean μ (left), resolution σ (RMS) of the $\frac{\Delta q}{q}$ distributions.

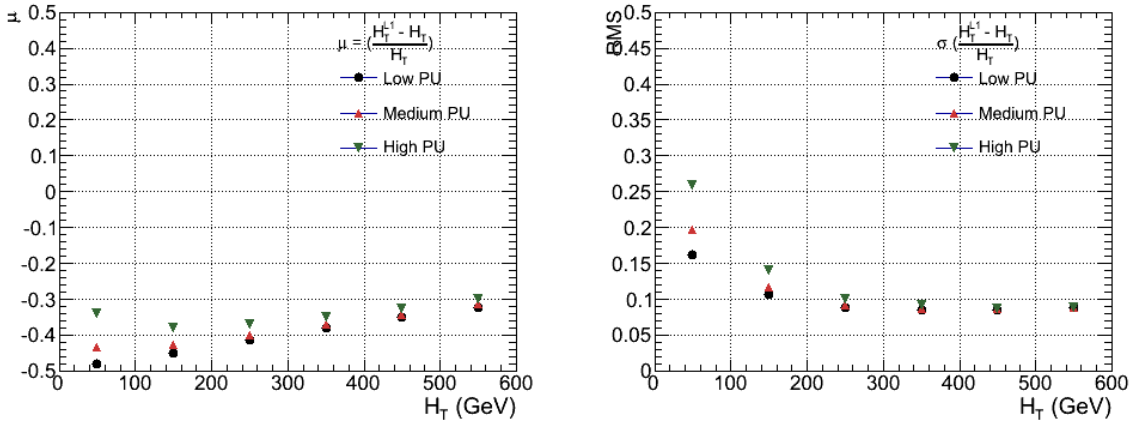


Figure B.8.: H_T resolution parameters in bins of Calo H_T measured for the defined low, medium and high pile up conditions. The plots show the mean μ (left), resolution σ (RMS) of the $\frac{\Delta q}{q}$ distributions.

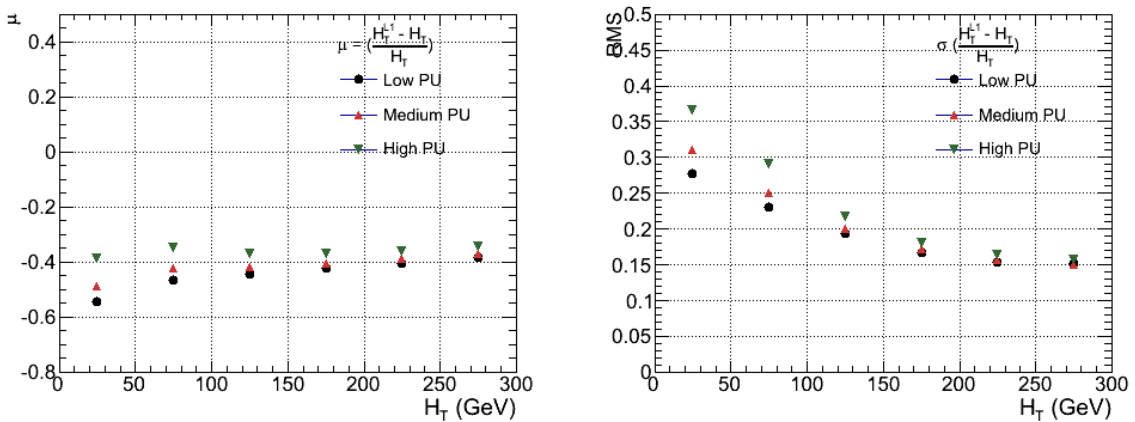


Figure B.9.: H_T resolution parameters in bins of PF H_T measured for the defined low, medium and high pile up conditions. The plots show the mean μ (left), resolution σ (RMS) of the $\frac{\Delta q}{q}$ distributions.

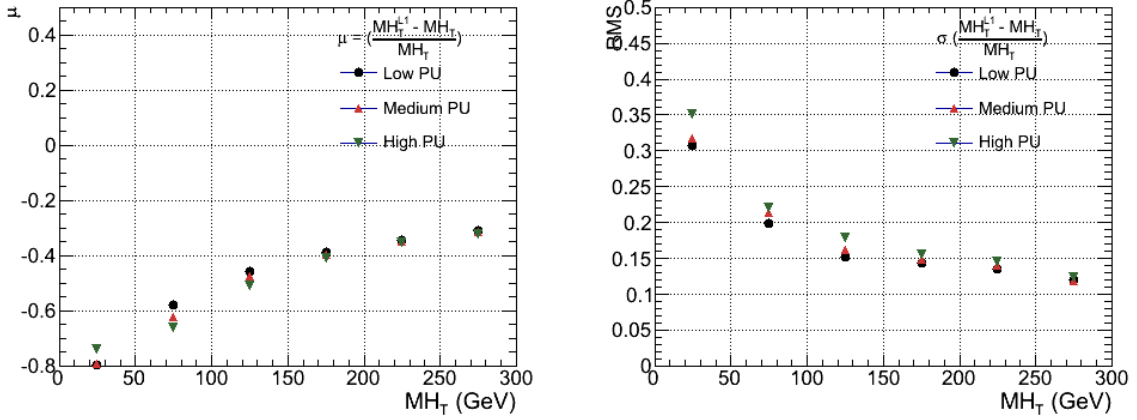


Figure B.10.: H_T resolution parameters in bins of H_T measured for the defined low, medium and high pile up conditions. The plots show the mean μ (left), resolution σ (RMS) of the $\frac{\Delta q}{q}$ distributions.

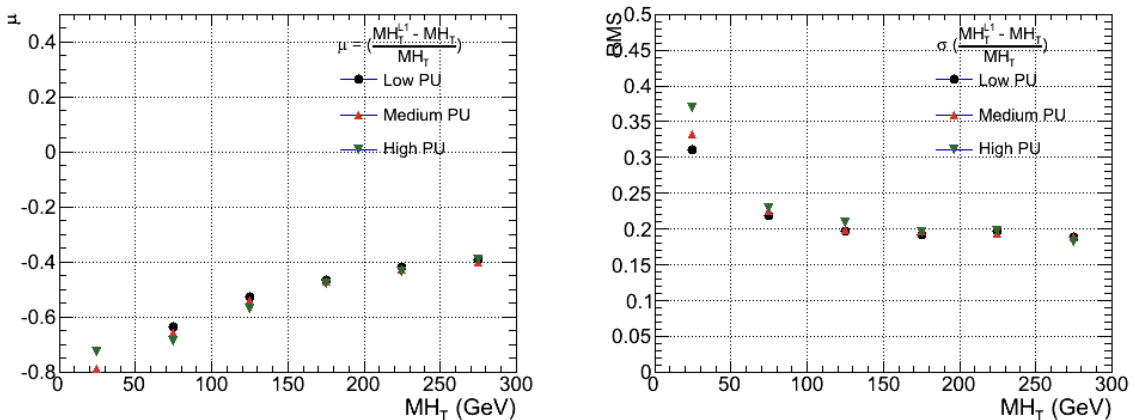


Figure B.11.: H_T resolution parameters in bins of PF H_T measured for the defined low, medium and high pile up conditions. The plots show the mean μ (left), resolution σ (RMS) of the $\frac{\Delta q}{q}$ distributions.

Appendix C.

¹⁹¹⁸ Additional material on background estimation methods

¹⁹²⁰ C.1. Determination of k_{QCD}

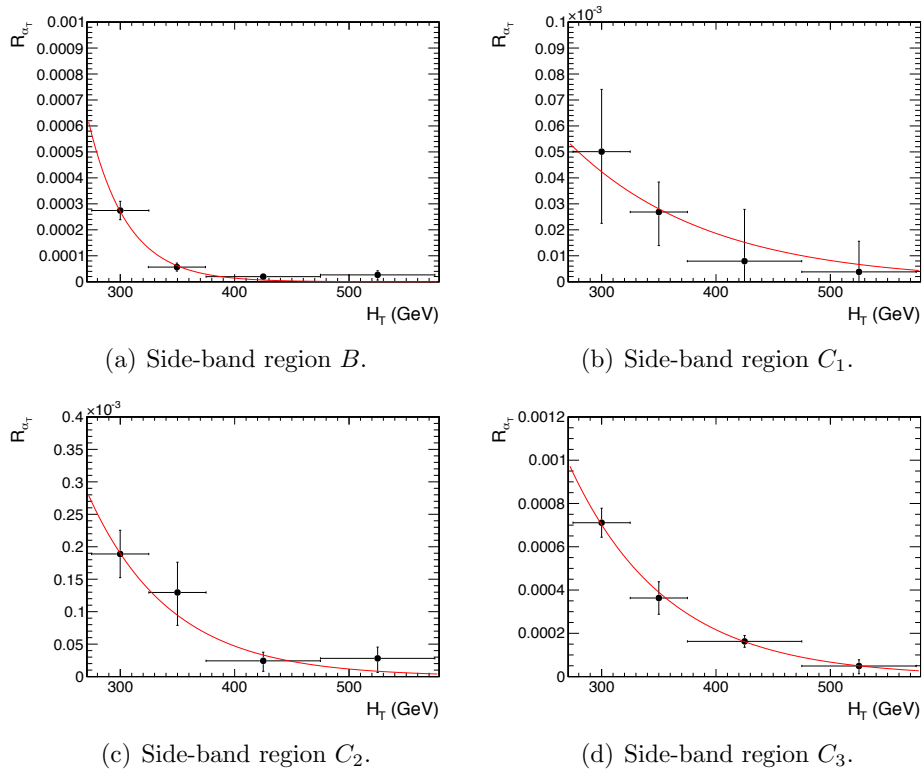


Figure C.1.: $R_{\alpha_T}(H_T)$ and exponential fits for each of the data sideband regions. Fit is conducted between the H_T region $275 < H_T < 575$.

C.2. Effect of varying background cross sections on closure tests

1922 Closure tests with cross section variations of +20% and -20% applied to $W + \text{jets}$ and $t\bar{t}$
1923 processes respectively.

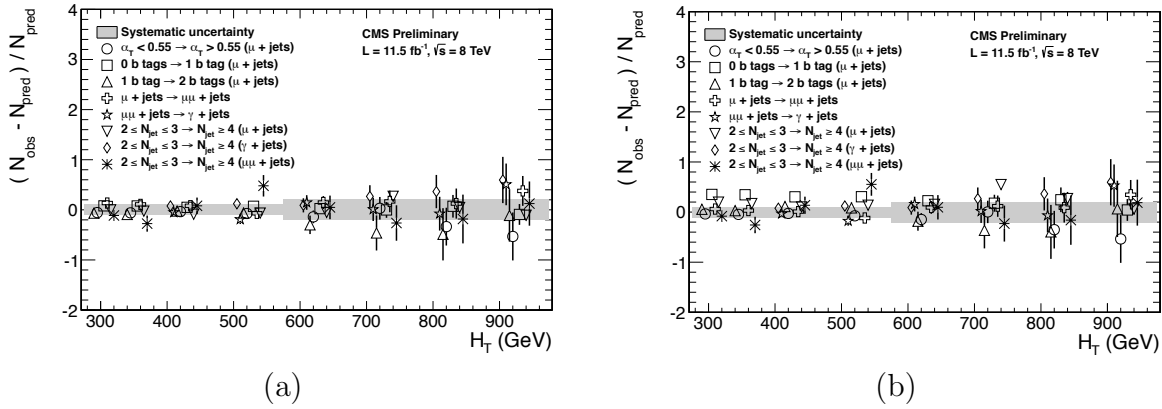


Figure C.2.: Sets of closure tests (open symbols) overlaid on top of the systematic uncertainty used for each of the five H_T regions (shaded bands) and for the two different jet multiplicity bins: (a) $2 \leq n_{jet} \leq 3$ and (b) $n_{jet} \geq 4$.

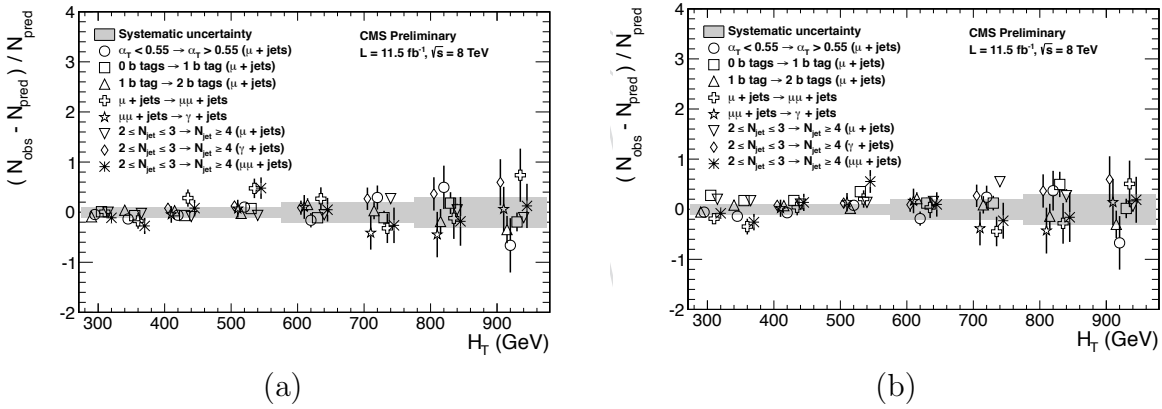


Figure C.3.: Sets of closure tests (open symbols) overlaid on top of the systematic uncertainty used for each of the five H_T regions (shaded bands) and for the two different jet multiplicity bins: (a) $2 \leq n_{jet} \leq 3$ and (b) $n_{jet} \geq 4$.

	H_T (GeV)
--	-------------

Table C.1.

Appendix D.

¹⁹²⁶ Additional Material For B-tag ¹⁹²⁷ Template Method

¹⁹²⁸ D.1. Templates Fits in Simulation

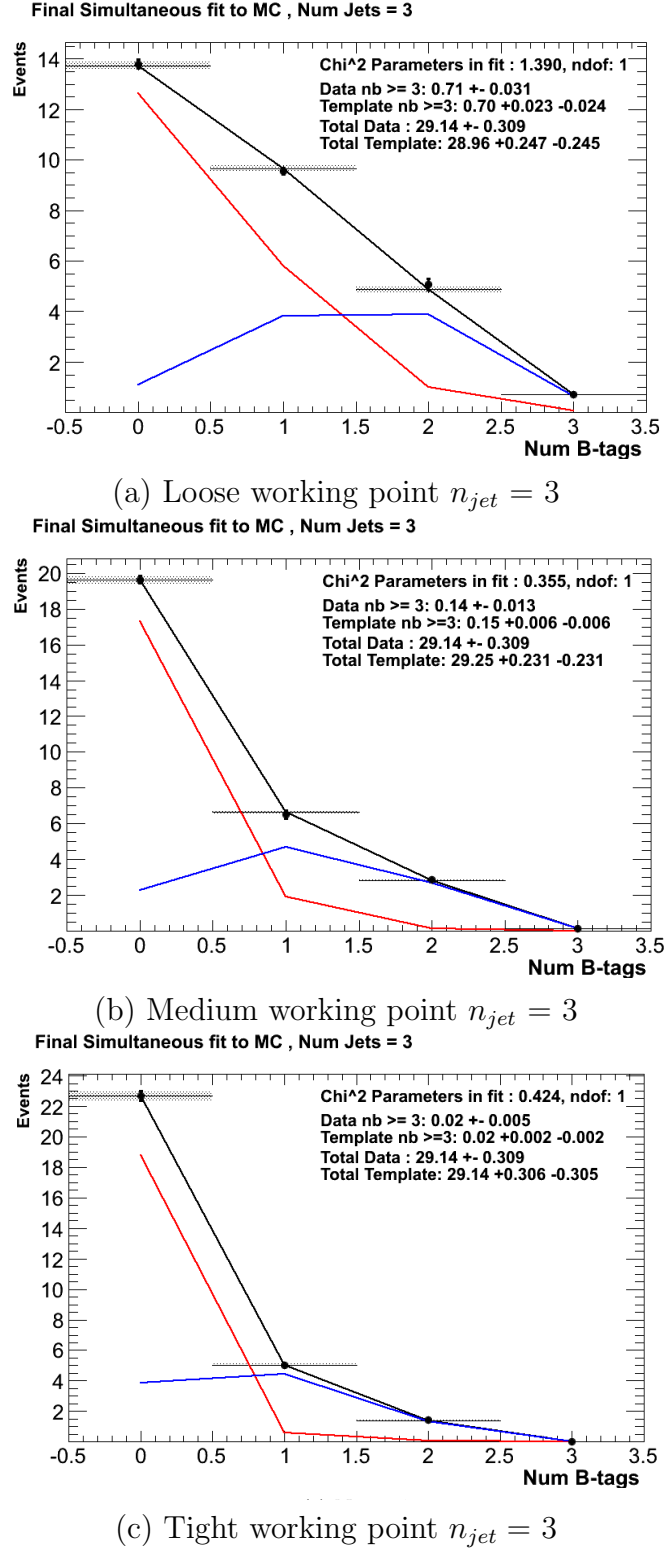


Figure D.1.: The results of fitting the $Z = 0$ and $Z = 2$ templates to the $n_b^{reco} = 0, 1, 2$ bins taken directly from simulation in the region $H_T > 375$ GeV, for the $n_{jet} = 3$ category. The red template represents $Z = 0$, while the blue template represents $Z = 2$. Grey bands represent the statistical uncertainty of the fit. The χ^2 parameter displayed represents the goodness of fit to the low n_b^{reco} (0-2) control region.

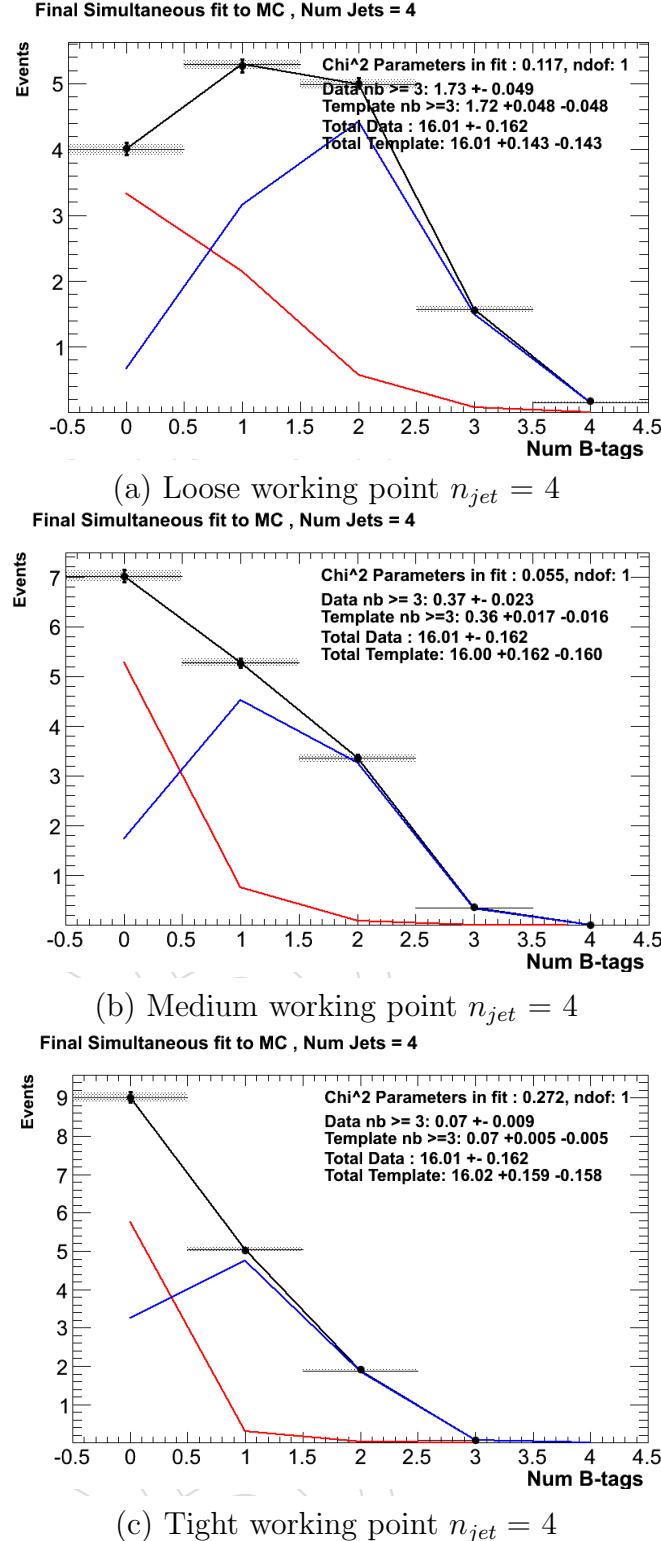


Figure D.2.: The results of fitting the $Z = 0$ and $Z = 2$ templates to the $n_b^{reco} = 0, 1, 2$ bins taken directly from simulation in the region $H_T > 375$ GeV, for the $n_{jet} = 4$ category. The red template represents $Z = 0$, while the blue template represents $Z = 2$. Grey bands represent the statistical uncertainty of the fit. The χ^2 parameter displayed represents the goodness of fit to the low n_b^{reco} (0-2) control region.

¹⁹²⁹ **D.2. Pull Distributions for Template Fits**

¹⁹³⁰ **D.3. Templates Fits in Data**

¹⁹³¹ Template fits for the loose **CSV** working point :

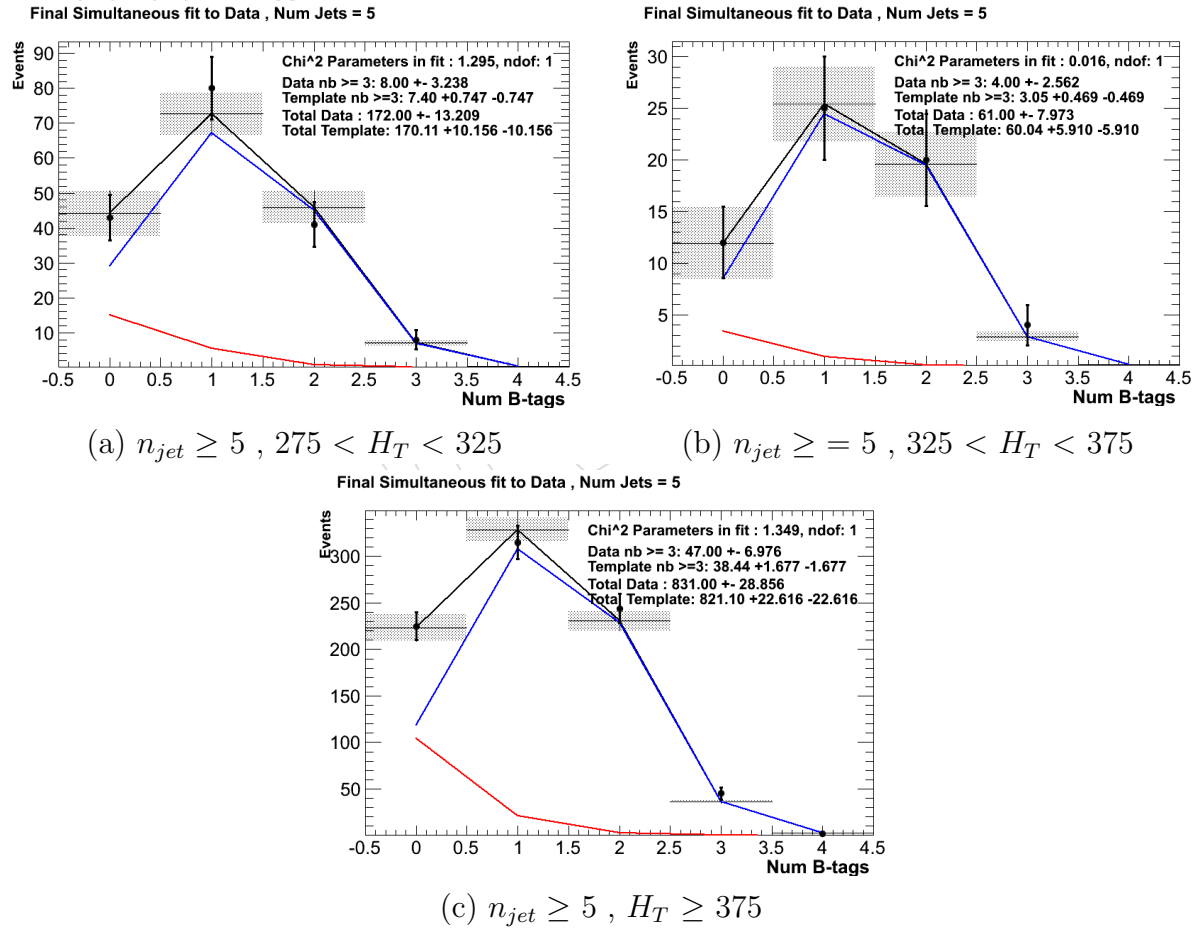


Figure D.3.: The results of fitting the $Z = 0$ and $Z = 2$ templates to the $n_b^{reco} = 0, 1, 2$ bins taken from data, for the $n_{jet} \geq 5$ category and loose **CSV** working point. The red template represents $Z = 0$, while the blue template represents $Z = 2$. The χ^2 parameter displayed represents the goodness of fit to the low n_b^{reco} (0-2) control region.

¹⁹³² Template fits for the tight **CSV** working point :

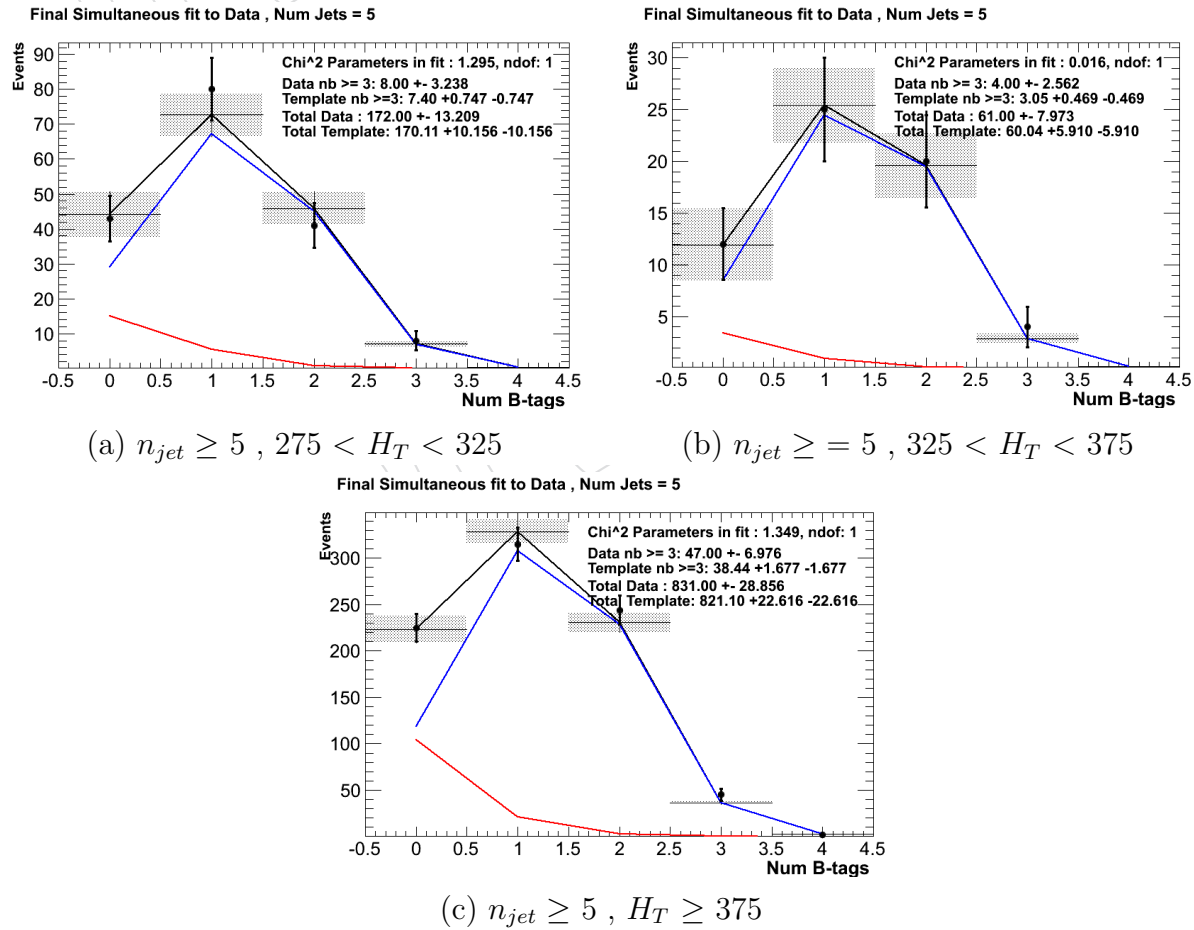


Figure D.4.: The results of fitting the $Z = 0$ and $Z = 2$ templates to the $n_b^{reco} = 0, 1, 2$ bins taken from data, for the $n_{jet} \geq 5$ category and tight CSV working point. The red template represents $Z = 0$, while the blue template represents $Z = 2$. The χ^2 parameter displayed represents the goodness of fit to the low n_b^{reco} (0-2) control region.

1933

¹⁹³⁴ Bibliography

- ¹⁹³⁵ [1] J. Beringer *et al.*, “Review of Particle Physics (RPP),” *Phys.Rev.*, vol. D86, p. 010001, 2012.
- ¹⁹³⁶
- ¹⁹³⁷ [2] G. H. et al., “Nine-year wilkinson microwave anisotropy probe (wmap) observations: Cosmological parameter results,” *The Astrophysical Journal Supplement Series*, vol. 208, no. 2, p. 19, 2013.
- ¹⁹³⁸
- ¹⁹³⁹
- ¹⁹⁴⁰ [3] G. Aad *et al.*, “Observation of a new particle in the search for the Standard Model Higgs boson with the ATLAS detector at the LHC,” *Phys.Lett.*, vol. B716, pp. 1–29, 2012.
- ¹⁹⁴¹
- ¹⁹⁴²
- ¹⁹⁴³ [4] S. Chatrchyan *et al.*, “Observation of a new boson at a mass of 125 GeV with the CMS experiment at the LHC,” *Phys.Lett.*, vol. B716, pp. 30–61, 2012.
- ¹⁹⁴⁴
- ¹⁹⁴⁵ [5] S. Chatrchyan *et al.*, “Search for supersymmetry in hadronic final states with missing transverse energy using the variables AlphaT and b-quark multiplicity in pp collisions at 8 TeV,” *Eur.Phys.J.*, vol. C73, p. 2568, 2013.
- ¹⁹⁴⁶
- ¹⁹⁴⁷
- ¹⁹⁴⁸ [6] S. Weinberg, “A model of leptons,” *Phys. Rev. Lett.*, vol. 19, pp. 1264–1266, Nov 1967.
- ¹⁹⁴⁹
- ¹⁹⁵⁰ [7] S. Glashow, “Partial Symmetries of Weak Interactions,” *Nucl.Phys.*, vol. 22, pp. 579–588, 1961.
- ¹⁹⁵¹
- ¹⁹⁵² [8] A. Salam, “Weak and Electromagnetic Interactions,” *Conf.Proc.*, vol. C680519, pp. 367–377, 1968.
- ¹⁹⁵³
- ¹⁹⁵⁴ [9] G. Hooft, “Renormalizable lagrangians for massive yang-mills fields,” *Nuclear Physics B*, vol. 35, no. 1, pp. 167 – 188, 1971.
- ¹⁹⁵⁵
- ¹⁹⁵⁶ [10] F. Hasert *et al.*, “Observation of Neutrino Like Interactions Without Muon Or Electron in the Gargamelle Neutrino Experiment,” *Phys.Lett.*, vol. B46, pp. 138–140, 1973.
- ¹⁹⁵⁷
- ¹⁹⁵⁸

- 1959 [11] G. Arnison *et al.*, “Experimental Observation of Lepton Pairs of Invariant Mass
1960 Around 95-GeV/c**2 at the CERN SPS Collider,” *Phys.Lett.*, vol. B126, pp. 398–410,
1961 1983.
- 1962 [12] M. Banner *et al.*, “Observation of Single Isolated Electrons of High Transverse
1963 Momentum in Events with Missing Transverse Energy at the CERN anti-p p
1964 Collider,” *Phys.Lett.*, vol. B122, pp. 476–485, 1983.
- 1965 [13] E. Noether, “Invariante variationsprobleme,” *Nachrichten von der Gesellschaft
1966 der Wissenschaften zu Gttingen, Mathematisch-Physikalische Klasse*, vol. 1918,
1967 pp. 235–257, 1918.
- 1968 [14] F. Halzen and A. D. Martin, “Quarks and leptons.” Wiley, 1985.
- 1969 [15] *Introduction to Elementary Particles*. Wiley-VCH, 2nd ed., Oct. 2008.
- 1970 [16] C. S. Wu, E. Ambler, R. W. Hayward, D. D. Hoppes, and R. P. Hudson, “Ex-
1971 perimental Test of Parity Conservation in Beta Decay,” *Physical Review*, vol. 105,
1972 pp. 1413–1415, Feb. 1957.
- 1973 [17] P. Higgs, “Broken symmetries, massless particles and gauge fields,” *Physics Letters*,
1974 vol. 12, no. 2, pp. 132 – 133, 1964.
- 1975 [18] F. Englert and R. Brout, “Broken symmetry and the mass of gauge vector mesons,”
1976 *Phys. Rev. Lett.*, vol. 13, pp. 321–323, Aug 1964.
- 1977 [19] P. W. Higgs, “Broken symmetries and the masses of gauge bosons,” *Phys. Rev. Lett.*,
1978 vol. 13, pp. 508–509, Oct 1964.
- 1979 [20] G. S. Guralnik, C. R. Hagen, and T. W. B. Kibble, “Global conservation laws and
1980 massless particles,” *Phys. Rev. Lett.*, vol. 13, pp. 585–587, Nov 1964.
- 1981 [21] S. Weinberg, “A model of leptons,” *Phys. Rev. Lett.*, vol. 19, pp. 1264–1266, Nov
1982 1967.
- 1983 [22] H. Yukawa, “On the interaction of elementary particles. i,” *Progress of Theoretical
1984 Physics Supplement*, vol. 1, pp. 1–10, 1955.
- 1985 [23] Y. e. a. Fukuda, “Evidence for oscillation of atmospheric neutrinos,” *Phys. Rev.
1986 Lett.*, vol. 81, pp. 1562–1567, Aug 1998.
- 1987 [24] R. Becker-Szendy, C. Bratton, D. Casper, S. Dye, W. Gajewski, *et al.*, “A Search
1988 for muon-neutrino oscillations with the IMB detector,” *Phys.Rev.Lett.*, vol. 69,

- 1989 pp. 1010–1013, 1992.
- 1990 [25] S. P. Martin, “A Supersymmetry primer,” 1997.
- 1991 [26] H. Nilles, *Supersymmetry, Supergravity and Particle Physics*. Physics reports, North-Holland Physics Publ., 1984.
- 1993 [27] H. E. Haber and G. L. Kane, “The Search for Supersymmetry: Probing Physics Beyond the Standard Model,” *Phys.Rept.*, vol. 117, pp. 75–263, 1985.
- 1995 [28] E. Witten, “Dynamical Breaking of Supersymmetry,” *Nucl.Phys.*, vol. B188, p. 513, 1981.
- 1997 [29] J. Wess and B. Zumino, “Supergauge transformations in four dimensions,” *Nuclear Physics B*, vol. 70, no. 1, pp. 39 – 50, 1974.
- 1999 [30] H. Muller-Kirsten and A. Wiedemann, *Introduction to Supersymmetry*. World Scientific lecture notes in physics, World Scientific, 2010.
- 2001 [31] I. Aitchison, *Supersymmetry in Particle Physics: An Elementary Introduction*. Cambridge University Press, 2007.
- 2003 [32] K. A. Intriligator and N. Seiberg, “Lectures on Supersymmetry Breaking,” *Class.Quant.Grav.*, vol. 24, pp. S741–S772, 2007.
- 2005 [33] Y. Shadmi, “Supersymmetry breaking,” pp. 147–180, 2006.
- 2006 [34] C. Burgess, P. G. Camara, S. de Alwis, S. Giddings, A. Maharana, *et al.*, “Warped Supersymmetry Breaking,” *JHEP*, vol. 0804, p. 053, 2008.
- 2008 [35] H. Murayama, “Supersymmetry breaking made easy, viable, and generic,” 2007.
- 2009 [36] H. Baer and X. Tata, *Weak Scale Supersymmetry: From Superfields to Scattering Events*. Cambridge University Press, 2006.
- 2011 [37] S. P. Martin, “Implications of supersymmetric models with natural r-parity conservation,” 1996.
- 2013 [38] G. L. Kane, C. F. Kolda, L. Roszkowski, and J. D. Wells, “Study of constrained minimal supersymmetry,” *Phys.Rev.*, vol. D49, pp. 6173–6210, 1994.
- 2015 [39] C. Stlege, G. Bertone, D. Cerdeno, M. Fornasa, R. Ruiz de Austri, *et al.*, “Updated global fits of the cmSSM including the latest LHC SUSY and Higgs searches and XENON100 data,” *JCAP*, vol. 1203, p. 030, 2012.

- 2018 [40] M. Citron, J. Ellis, F. Luo, J. Marrouche, K. Olive, *et al.*, “The End of the CMSSM
2019 Coannihilation Strip is Nigh,” *Phys.Rev.*, vol. D87, p. 036012, 2013.
- 2020 [41] D. Ghosh, M. Guchait, S. Raychaudhuri, and D. Sengupta, “How Constrained is
2021 the cMSSM?,” *Phys.Rev.*, vol. D86, p. 055007, 2012.
- 2022 [42] D. Alves *et al.*, “Simplified Models for LHC New Physics Searches,” *J.Phys.*, vol. G39,
2023 p. 105005, 2012.
- 2024 [43] J. Alwall, P. Schuster, and N. Toro, “Simplified Models for a First Characterization
2025 of New Physics at the LHC,” *Phys.Rev.*, vol. D79, p. 075020, 2009.
- 2026 [44] S. Chatrchyan *et al.*, “Interpretation of Searches for Supersymmetry with simplified
2027 Models,” *Phys.Rev.*, vol. D88, p. 052017, 2013.
- 2028 [45] J. Hisano, K. Kurosawa, and Y. Nomura, “Natural effective supersymmetry,”
2029 *Nucl.Phys.*, vol. B584, pp. 3–45, 2000.
- 2030 [46] M. Papucci, J. T. Ruderman, and A. Weiler, “Natural SUSY Endures,” *JHEP*,
2031 vol. 1209, p. 035, 2012.
- 2032 [47] B. Allanach and B. Gripaios, “Hide and Seek With Natural Supersymmetry at the
2033 LHC,” *JHEP*, vol. 1205, p. 062, 2012.
- 2034 [48] K. Aamodt *et al.*, “The ALICE experiment at the CERN LHC,” *JINST*, vol. 3,
2035 p. S08002, 2008.
- 2036 [49] G. Aad *et al.*, “The ATLAS Experiment at the CERN Large Hadron Collider,”
2037 *JINST*, vol. 3, 2008.
- 2038 [50] R. Adolphi *et al.*, “The cms experiment at the cern lhc,” *JINST*, vol. 0803, p. S08004,
2039 2008.
- 2040 [51] A. A. Alves *et al.*, “The LHCb Detector at the LHC,” *JINST*, vol. 3, p. S08005,
2041 2008.
- 2042 [52] J.-L. Caron, “Lhc layout.. schema general du lhc..” Sep 1997.
- 2043 [53] C. Collaboration, “Cms luminosity - public results.”
2044 twiki.cern.ch/twiki/bin/view/CMSPublic/LumiPublicResults., 2011.
- 2045 [54] CERN, “Cms compact muon solenoid..” <http://public.web.cern.ch/public/Objects/LHC/CMSnc.jpg>
2046 Feb 2010.

- 2047 [55] *The CMS electromagnetic calorimeter project: Technical Design Report*. Technical
2048 Design Report CMS, Geneva: CERN, 1997.
- 2049 [56] *The CMS muon project: Technical Design Report*. Technical Design Report CMS,
2050 Geneva: CERN, 1997.
- 2051 [57] CMS Collaboration, “The cms physics technical design report, volume 1,”
2052 *CERN/LHCC*, vol. 2006-001, 2006.
- 2053 [58] M. Cacciari, G. P. Salam, and G. Soyez, “The anti- k_t jet clustering algorithm,”
2054 *Journal of High Energy Physics*, vol. 2008, no. 04, p. 063, 2008.
- 2055 [59] “Jet performance in pp collisions at 7 tev,” Tech. Rep. CMS-PAS-JME-10-003,
2056 CERN, Geneva, 2010.
- 2057 [60] X. Janssen, “Underlying event and jet reconstruction in cms,” Tech. Rep. CMS-CR-
2058 2011-012, CERN, Geneva, Jan 2011.
- 2059 [61] T. C. collaboration, “Determination of jet energy calibration and transverse mo-
2060 mentum resolution in cms,” *Journal of Instrumentation*, vol. 6, no. 11, p. P11002,
2061 2011.
- 2062 [62] R. Eusebi and on behalf of the CMS collaboration), “Jet energy corrections and
2063 uncertainties in cms: reducing their impact on physics measurements,” *Journal of
2064 Physics: Conference Series*, vol. 404, no. 1, p. 012014, 2012.
- 2065 [63] “Algorithms for b Jet identification in CMS,” Tech. Rep. CMS-PAS-BTV-09-001,
2066 CERN, 2009. Geneva, Jul 2009.
- 2067 [64] “Performance of b tagging at $\sqrt{s}=8$ tev in multijet, ttbar and boosted topology
2068 events,” no. CMS-PAS-BTV-13-001, 2013.
- 2069 [65] T. C. collaboration, “Identification of b-quark jets with the cms experiment,” *Journal
2070 of Instrumentation*, vol. 8, no. 04, p. P04013, 2013.
- 2071 [66] S. Dasu *et al.*, “CMS. The TriDAS project. Technical design report, vol. 1: The
2072 trigger systems,” 2000.
- 2073 [67] P. Sphicas, “CMS: The TriDAS project. Technical design report, Vol. 2: Data
2074 acquisition and high-level trigger,” 2002.
- 2075 [68] J. B. et al., “Calibration and Performance of the Jets and Energy Sums in the
2076 Level-1 Trigger ,” no. CMS IN 2013/006 (2013), 2013.

- 2077 [69] B. et al., “Study of Level-1 Trigger Jet Performance in High Pile-up Running
2078 Conditions,” no. CMS IN 2013/007 (2013), 2013.
- 2079 [70] J. J. Brooke, “Performance of the cms level-1 trigger,” Tech. Rep. CMS-CR-2012-322.
2080 CERN-CMS-CR-2012-322, CERN, Geneva, Nov 2012.
- 2081 [71] L. Randall and D. Tucker-Smith, “Dijet searches for supersymmetry at the large
2082 hadron collider,” *Phys. Rev. Lett.*, vol. 101, p. 221803, Nov 2008.
- 2083 [72] “SUSY searches with dijet events,” 2008.
- 2084 [73] “Search strategy for exclusive multi-jet events from supersymmetry at CMS,” Tech.
2085 Rep. CMS-PAS-SUS-09-001, CERN, 2009. Geneva, Jul 2009.
- 2086 [74] “Calorimeter Jet Quality Criteria for the First CMS Collision Data,” Tech. Rep.
2087 CMS-PAS-JME-09-008, CERN, 2010. Geneva, Apr 2010.
- 2088 [75] T. C. collaboration, “Performance of cms muon reconstruction in pp collision events
2089 at $\sqrt{s} = 7$ tev,” *Journal of Instrumentation*, vol. 7, no. 10, p. P10002, 2012.
- 2090 [76] “Search for supersymmetry in events with photons and missing energy,” Tech. Rep.
2091 CMS-PAS-SUS-12-018, CERN, Geneva, 2012.
- 2092 [77] M. Cacciari and G. P. Salam, “Pileup subtraction using jet areas,” *Phys.Lett.*,
2093 vol. B659, pp. 119–126, 2008.
- 2094 [78] Z. Bern, G. Diana, L. J. Dixon, F. Febres Cordero, S. Hoche, H. Ita, D. A. Kosower,
2095 D. Maitre, and K. J. Ozeren, “Driving missing data at next-to-leading order,” *Phys.
2096 Rev. D*, vol. 84, p. 114002, Dec 2011.
- 2097 [79] “Data-Driven Estimation of the Invisible Z Background to the SUSY MET Plus
2098 Jets Search,” Tech. Rep. CMS-PAS-SUS-08-002, CERN, 2009. Geneva, Jan 2009.
- 2099 [80] Z. Bern, G. Diana, L. Dixon, F. Febres Cordero, S. Hoche, *et al.*, “Driving Missing
2100 Data at Next-to-Leading Order,” *Phys.Rev.*, vol. D84, p. 114002, 2011.
- 2101 [81] C. Collaboration, “Cms btag pog : Cms b-tagging performance database.”
2102 <https://twiki.cern.ch/twiki/bin/viewauth/CMS/BtagPOG>, 2013.